Novel Waveform Design Algorithms for Pulse Compression Radars

by

Kubilay Savcı

A Dissertation Submitted to the
Graduate School of Sciences and Engineering
in Partial Fulfillment of the Requirements for
the Degree of

Doctor of Philosophy

in

Electrical and Electronics Engineering

KOÇ ÜNİVERSİTESİ

September 06, 2022

Novel Waveform Design Algorithms for Pulse Compression Radars

Koç University

Graduate School of Sciences and Engineering

This is to certify that I have examined this copy of a doctoral dissertation by

Kubilay Savcı

and have found that it is complete and satisfactory in all respects,

and that any and all revisions required by the final

examining committee have been made.

Committee Members:

Prof. Alper T. Erdoğan (Advisor)

Prof. Engin Erzin

Prof. Lütfiye Durak Ata

Prof. Selçuk Paker

Assoc. Prof. Kaan Güven

Date:

ABSTRACT

Novel Waveform Design Algorithms for Pulse Compression Radars
Kubilay Savcı
Doctor of Philosophy in Electrical and Electronics Engineering
September 06, 2022

Radar systems have been used widely for the detection of remote targets since World War II, and since then, they have become ubiquitous in remote sensing applications. At its core, the radar probing waveform has received considerable attention in the past decades with the advances in digital hardware and signal processing techniques. Indeed, waveforms and their synthesis methods can find diverse applications in areas, not only in active remote sensing but also in communications and medical imaging. In recent years, computational methods have been devised to synthesize arbitrary waveforms under various practical constraints, including the Low Peak-to-Average-Power-Ratio (PAPR), unimodularity, correlation constraints and spectrum allocation restrictions with the aim of improving the underlying system performance. With the new trends in radar techniques, such as noise radar and cognitive radar, the transmit waveforms and pertinent terms such as waveform diversity and waveform adaptivity have attracted more attention due to their practical benefits.

In this thesis, we give an introduction to the new trends and techniques, i.e. noise radar technology and cognitive radar, and further propose two novel waveform design algorithms, particularly for noise radar technology and spectrum-aware sensing systems such as cognitive radar. The first algorithm named 'Combined Spectral Shaping and Peak-to-Average Power Reduction (COSPAR)' which embodies a parametric window function as a spectral weighting to control the autocorrelation sidelobes and a Peak-to-Average-Power-Ratio (PAPR) reduction technique inspired by a phase retrieval algorithm is proposed to synthesize tailored noise waveforms for enhanced Low Probability of Intercept (LPI) radar operation. The proposed COSPAR algorithm is recommended for the generation of infinitely many orthogonal low PAPR noise-like signals suitable to feed up noise radar waveform libraries. Furthermore, a visual analysis tool based on Spectral Kurtosis in the Time-Frequency

domain is proposed to assess the noise-like behaviour and pertinent LPI characteristics of the signal. In the second algorithm, we pose the waveform design task as a nonlinear large-scale optimization problem and propose a novel computational approach utilizing a nonlinear optimization technique i.e. Limited Memory Broyden-Fletcher-Goldfarb-Shanno (L-BFGS) recursion to synthesize unimodular sequences with good correlation and spectral stopband properties. The proposed algorithm, named 'L-BFGS based Sequence Design (LBSD)', includes a modified search direction and step length rule to facilitate faster convergence and aims to accelerate the overall waveform generation process. As a result, the proposed method is viable for the agile generation of spectrally compatible waveforms that are essential for cognitive radars.

Finally, the benefits and good features of the proposed COSPAR signals are shown in field trials using an experimental noise radar demonstrator system, and some results from these experiments are reported in the thesis. Additionally, the performance of the proposed LBSD algorithm is shown via numerical examples in comparison to existing state-of-art waveform design algorithms.

ÖZETÇE

Darbe Sıkıştırma Radarları için Yenilikçi Dalgaformu Tasarım Algoritmaları
Kubilay Savcı
Elektrik ve Elektronik Mühendisliği, Doktora
06 Eylül 2022

Radar sistemleri, II. Dünya Savaşı'ndan beri uzak hedeflerin tespiti için yaygın olarak kullanılmış ve o zamandan bu yana uzaktan algılama uygulamalarının her alanında kullanılır hale gelmişlerdir. Radar sistemlerinin temelinde bulunan radar gönderim dalga formu, sayısal donanım ve sinyal işleme tekniklerindeki gelişmelerle birlikte son yıllarda büyük ilgi görmüştür. Doğrusu, dalga formları ve sentez yöntemleri yalnızca aktif uzaktan algılamada değil, aynı zamanda iletişim ve tıbbi görüntüleme alanlarında da çeşitli uygulamalar bulabilmektedir. Son yıllarda, altta yatan sistemin performansını iyileştirmek amacıyla Düşük Tepe-Ortalama-Güç Oranı (PAPR), birim genlik, korelasyon kısıtları ve spektrum tahsis sınırlamaları dahil olmak üzere çeşitli pratik kısıtlar altında istenen dalga formlarını sentezlemek için hesaplama yöntemleri geliştirilmiştir. Gürültü radarı ve bilişsel radar gibi radar tekniklerindeki yeni eğilimlerle birlikte, yayın dalga formları ve dalga formu çeşitliliği ile dalga formu uyarlanabilirliği gibi ilgili terimler, pratik faydaları nedeniyle daha fazla dikkat çekmiştir.

Bu tezde, gürültü radar teknolojisi ve bilişsel radar gibi yeni eğilimler ve teknikler hakkında genel bir bakış sunulmakta ve ek olarak özellikle gürültü radar teknolojisi ve bilişsel radar gibi spektruma duyarlı algılama sistemleri için iki yeni dalga formu tasarım algoritması önerilmektedir. Öz ilinti yan kulakçıklarını kontrol etmek için izgesel ağırlık olarak parametrik bir pencere fonksiyonunu ve faz geri kazanım algoritmasından esinlenen bir Tepe-Ortalama Güç Oranı (PAPR) azaltma tekniğini içeren 'Birleşik İzgesel Şekillendirme ve Tepe-Ortalama Güç Azaltma (COSPAR)' olarak adlandırılan önerilen birinci algoritma, radarın gelişmiş Düşük Kestirim Olasılığı (LPI) etkinliği altında çalışması amacıyla uyarlanmış gürültü dalga formlarını sentezlemek için önerilmiştir. Önerilen COSPAR algoritması, gürültü radarı için dalga

formu kütüphaneleri oluşturmaya uygun sonsuz sayıda dikgen düşük PAPR'a sahip gürültü benzeri sinyallerin üretilmesi için önerilmektedir. Ayrıca, sinyalin gürültüye benzerliğini ve LPI özelliğini değerlendirmek için Zaman-Frekans uzayında İzgesel Basıklık'a dayalı bir görsel analiz aracı önerilmiştir. İkinci algoritmada, dalga formu tasarım görevi doğrusal olmayan büyük ölçekli bir optimizasyon problemi olarak ortaya konulmakta ve iyi öz ilinti ve izgesel durdurma bandı özelliklerine sahip birim genlikli dizileri sentezlemek için Sınırlı Bellek Broyden-Fletcher-Goldfarb-Shanno (L-BFGS) özyinelemesi gibi doğrusal olmayan bir optimizasyon tekniğini kullanan yeni bir hesaplama yaklaşımı önerilmektedir. 'L-BFGS tabanlı Dizi Tasarımı (LBSD)' olarak adlandırılan bu algoritma, daha hızlı yakınsamayı kolaylaştırmak için özgün bir arama yönü ve adım uzunluğu kuralı içermektedir ve genel hatlarıyla dalga formu sentezleme sürecini hızlandırmayı amaçlamaktadır. Sonuç olarak, önerilen yöntem, bilişsel radarlar için gerekli olan izgesel uyumlu dalga formlarının çevik şekilde üretimi için uygundur.

Son olarak, önerilen COSPAR sinyallerinin faydaları ve iyi özellikleri, deneysel bir gürültü radarı gösterim sistemi kullanılarak yapılan saha denemelerinde gösterilmiş ve bu deneylerden elde edilen bazı sonuçlar tezde sunulmuştur. Ek olarak, önerilen LBSD algoritmasının performansı, literatürde mevcut yeni dalga formu tasarım algoritmalarına kıyasla sayısal örneklerle gösterilmektedir.

ACKNOWLEDGMENTS

I would like to express my sincere gratitude and profound respect to my supervisor, Prof. Dr. Alper Tunga Erdoğan for the patient guidance, inspiration, encouragement, and valuable support throughout the development of this thesis. I will always feel proud to be one of his students and never forget his support throughout my doctoral studies.

I would like to thank the members of my dissertation committee Prof. Dr. Engin Erzin, Doç. Dr. Kaan Güven, Prof. Dr. Lütfiye Durak Ata and Prof. Dr. Selçuk Paker for their valuable comments, time, interest, and serving on my defense committee.

I deeply appreciate the collaboration from my colleagues and co-authors at Turkish Navy Research Center Command for their invaluable support in numerous research efforts.

Last but foremost, I wish to express my love and deepest gratitude to my family for their constant support, encouragement, inspiration, and never-ending patience. This work would never have been possible without their unconditional trust in me.

TABLE OF CONTENTS

LIST OF TABLES

LIST OF FIGURES

ABBREVIATIONS

ACF	Auto Correlation Function
ADC	Analog-to-Digital Converter
AF	Ambiguity Function
BT	Bandwidth Time Product
CA	Cyclic Algorithm
CDMA	Code Division Multiple Access
CE	Continuous Emission
COSPAR	Combined Spectral Shape and Peak-to-Average-Power Ratio Reduction Algorithm
CR	Cognitive Radar
CW	Continuous Wave
CWD	Choi–Williams Distribution
DAC	Digital-to-Analog Converter
DSP	Digital Signal Processor
DRT	Deterministic Radar Technology
DFT/IDFT	Discrete Fourier Transform/Inverse DFT
EA	Electronic Attack
ECM	Electronic Counter Measure
ECCM	Electronic Counter Counter Measure
ELINT	Electronic Intelligence
EP	Electronic Protection
ESM	Electronic Support Measures
EW	Electronic Warfare
FFT/IFFT	Fast Fourier Transform/Inverse FFT
FMCW	Frequency Modulated Continuous Wave

FPGA	Field Processing Gate Array
ISL	Integrated Sidelobe Level
IF	Intermediate Frequency
L-BFGS	Limited Memory Broyden–Fletcher–Goldfarb–Shanno Algorithm
LBSD	L-BFGS Based Sequence Design Algorithm
LFM	Linear Frequency Modulation
LPE	Low Probability of Exploitation
LPI	Low Probability of Intercept
LPID	Low Probability of Identification
MF	Matched Filter
MM	Majorization-Minimization
MMF	Modified Merit Factor
MSPS	Mega Samples Per Second
NLFM	Nonlinear Frequency Modulation
NRT	Noise Radar Technology
PAPR	Peak-to-Average Power Ratio
PSD	Power Spectral Density
PSL	Peak Sidelobe Level
PSLR	Peak-to-(Mean)Sidelobes-Ratio
PRNG	Pseudo Random Noise Generator
PR	Phase Retrieval
RCS	Radar Cross Section
RF	Radio Frequency
SNR	Signal-to-Noise Ratio
SK	Spectral Kurtosis
STFT	Short Time Fourier Transform
WVD	Wigner–Ville Distribution

Chapter 1

INTRODUCTION

1.1 Radar Waveform Design

The waveform is a key component of a radar system, and it is a primary factor in determining many of the radar's performances. A proper waveform choice will allow the radar to: (I) achieve greater resolution in Doppler (velocity) and delay (range) space; (II) deliver maximum signal energy albeit using low peak power; (III) use the spectrum efficiently; and (IV) utilize a diversity of signals belonging to the same class, which may allow a plurality of radars to operate in the vicinity of each other and can aid in countering electronic counter measures (ECM).

Typically, radar employs a narrow-band signal, the bandwidth of which is significantly narrower than the carrier frequency. In order to utilize small-sized antennas, a high carrier frequency, often in the microwave spectrum, is necessary. The signal bandwidth is a trade between the need for higher (narrow) range resolution, which necessitates a wide bandwidth, and the radar transceiver's preference for a narrow bandwidth due to the linearity issues.

One can obtain a wide pulse bandwidth by modulating the waveform. Any of the three waveform properties - amplitude, frequency, and phase - might be modulated. The only way to modulate a power oscillator such as a magnetron back in the early days of radar was to use on-off keying. Wide bandwidth resulted from a very narrow sinusoidal signal, and this narrow signal had to have a very high peak power in order to produce the high pulse energy needed for detecting distant targets.

The drawback of magnetron was unsteady frequency and phase. The frequency and phase of waveforms generated by modern radar technology can be precisely controlled. This allows for frequency modulation as well as phase modulation, and it also makes the radar 'coherent'. By modulating the phase, frequency, or amplitude of a coherent radar signal, one can increase the bandwidth of a long pulse, causing it to behave like a narrow pulse. This is referred to as 'pulse compression', and it is the primary topic of waveform design and processing.

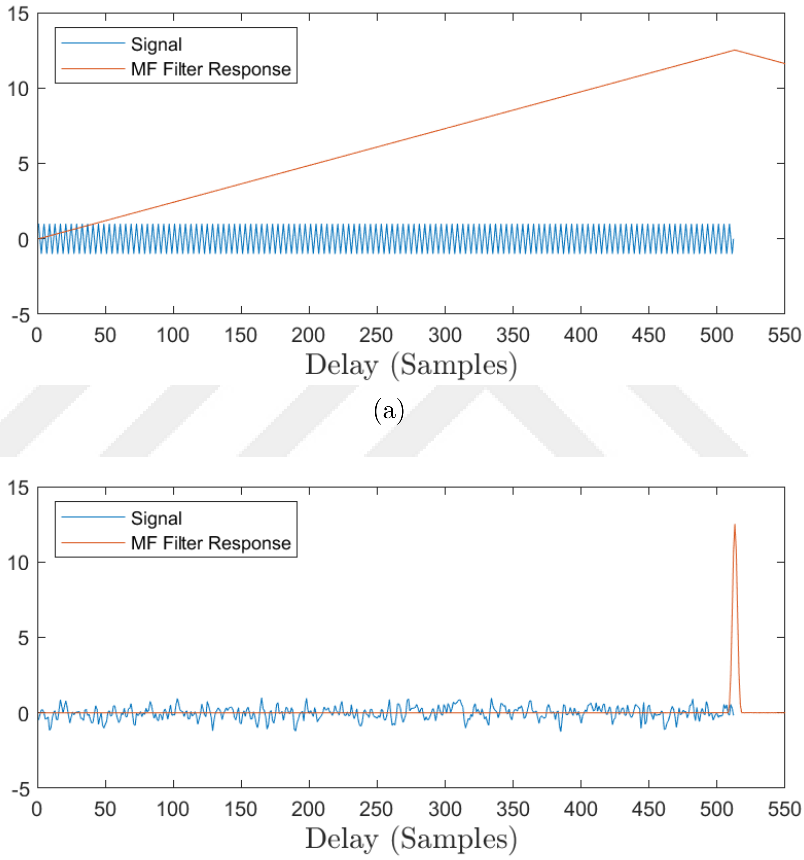

(a)

(b)

Figure 1.1: Signals and their matched filter response: (a) Unmodulated Signal, (b) Modulated Signal.

An illustration of pulse compression is presented in Figure 1.1. As a point of reference, Figure 1.1a depicts a sinusoidal signal with a rectangular real envelope. In addition, the envelope of a delay response at the receiver once the pulse is processed by its matching filter (MF) is overlaid on it. At this stage, it is sufficient to state that the MF output represents the waveform's auto-correlation function (ACF). As expected from the ACF of a rectangle, the response is a wide triangle with a rise time equal to the pulse duration. Figure 1.1b depicts a signal with amplitude and phase modulation of the same duration. The delay response was significantly narrowed as a result of the modulation. All of the energy from the long pulse was squeezed into a short pulse, which is why the process is called "pulse compression." Another desirable property of the delay response is the low sidelobes surrounding the narrow mainlobe.

Figure 1.2 demonstrates the frequency spectrum of two exemplary modulated and unmodulated signals. The modulated signal's spectral mainlobe is actually broader. Proper design, on the other hand, resulted in extremely low spectral sidelobes outside of the band. As a result of this feature, more radars can coexist in close vicinity, improving spectrum utilization.

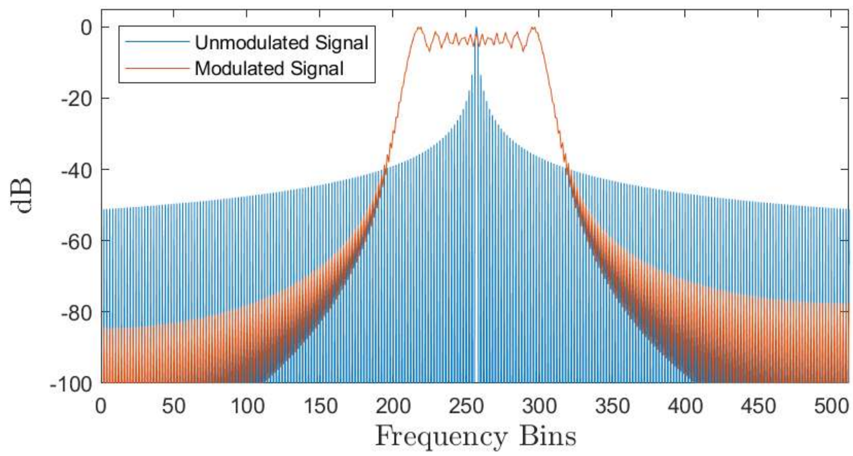

Figure 1.2: Spectrum of the unmodulated and modulated signals.

Figure 1.3 illustrates the importance of decreasing delay sidelobes. Two nearby targets' reflection intensities (i.e., radar cross section (RCS)) can differ significantly from one another. Figure 1.3a demonstrates how a strong target can conceal a neighbouring weak target with its large sidelobes. The weak target can be seen more clearly when the sidelobes are lowered as shown in Figure 1.3b.

The other challenge with resolution is target velocity, in other words the Doppler

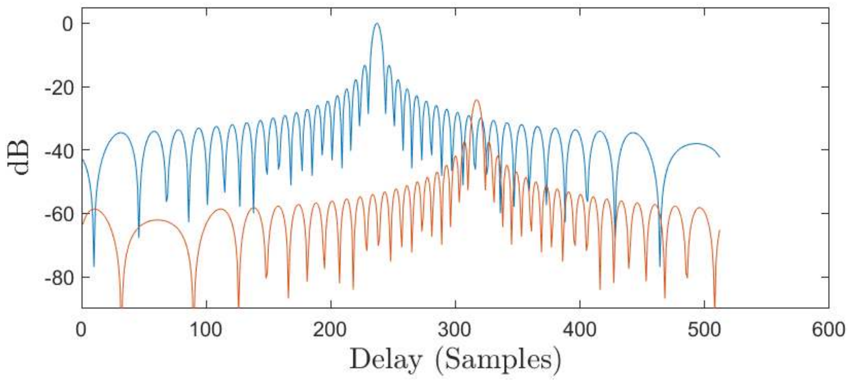

(a)

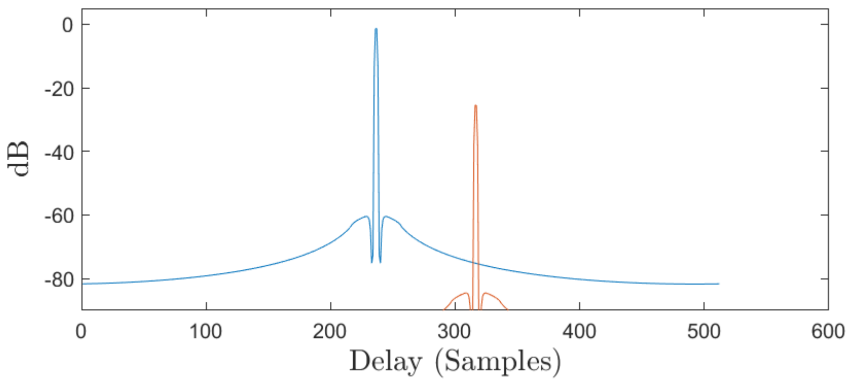

(b)

Figure 1.3: MF responses of a compressed pulse: (a) without and (b) with sidelobe reduction.

shift. Coherent signal time must be long enough to achieve a narrow Doppler resolution. Long signal duration does not necessarily indicate continuous transmission, but it does entail long coherent processing. A common waveform related to long coherent processing is a coherent train of numerous widely spaced, narrow pulses. Antenna dwell time on the target, or the amount of time that the received reflection from the target may remain coherent, determines the length of this coherent processing interval (CPI) duration.

Radar waveform design has indeed become a hot subject in the scientific and industrial arena as a result of the advent of new computer architectures, high-speed and off-the-shelf processors, arbitrary digital waveform generators, Multiple-Input-Multiple-Output with multiple transmit and receive elements, solid-state technology, etc. Actually, in extreme interference circumstances with clutter, jammers, and concurrent radiators, radar waveform synthesis and diversification may give unique characteristics to increase radar performance in terms of detection, classification, identification, and localization. Adaptability in transmission is also important to the current cognitive radar concept citing [1, 2] which uses external stimulation to motivate the perception-action loop. Radar waveform synthesis is often produced as the solution to a constrained optimization problem with constraints based on internal and external data, the latter of which may be acquired during the perception cycle or pre-stored in the transceiver.

Radar waveform design methods are also essential for constructing waveform libraries from which the best suitable waveforms can be chosen "on the fly." Again, optimization theory is useful in addressing the optimization of certain performance metrics, such as the Integrated Sidelobe Level (ISL) or Peak Sidelobe Level (PSL) and so on. In fact, during the past 15 years there has been an explosion of creative strategies for radar signal design that primarily use mathematical approaches derived from optimization theory and operations research [3, 4].

1.2 Literature Review and Motivation

Pulse compression radar, sonar, and communication systems all benefit greatly from transmit waveforms or finite sequences with low periodic or aperiodic autocorrelation sidelobes [5–7]. A pulse compression radar's matched filter output is the waveform's autocorrelation function (ACF) convolved with the of scatterer points (similar to Channel Impulse Response coefficients). Thus, weak scatterers are not easily discernible due to the strong correlation sidelobes around the correlation peak response of a powerful scatterer. Using an autocorrelation function that is similar to an impulse is preferable when trying to identify weak targets. Code Division Multiple Access (CDMA) and other communication systems benefit from low autocorrelation sidelobes because they improve synchronization and lessen the impact of multipath effects and user interference. In order to improve power efficiency and assure linear functioning of the power amplifiers in transceivers, it is sometimes necessary to have a constant modulus property for sequences in addition to having minimal autocorrelation sidelobes [3].

The electromagnetic spectrum, on the other hand, is limited, and because numerous systems share the same frequency range, they interfere with one another. Waveforms with spectral stopband properties are frequently needed in such a congested electromagnetic environment to reduce interference and jamming [8–10]. Waveforms having the spectral stopband feature, commonly known as Sparse Frequency Waveforms (SFW) in the literature, have a spectrum that contains a number of notched restricted frequency bands. Applications for SFW include high frequency radars [11], ultra-wide band systems [12], and cognitive radars [1, 2]. Continuous RF spectrum monitoring and rapid synthesis of a spectrally compatible waveform against dynamic radio environment are essential in such spectrum aware systems to counter jammers and interference [13].

Due to the wide range of uses and significant practical advantages of waveforms with low autocorrelation sidelobes and stopband property, researchers have become increasingly interested in the production techniques of such sequences. Several references provide in-depth analyses on this issue [4, 5, 14]. In the following, we present a brief literature about the radar waveform topic and explain what motivates us to conduct research on waveform design techniques.

The majority of the early efforts on waveform design focus on the creation of binary sequences, followed by the synthesis of polyphase signals. Closed form algebraic formulas were developed early on to construct such sequences with good correlation features (Barker code (Binary) [15], Frank code (Polyphase) [16], Chu code (Polyphase) [17], P1-P4 codes (Polyphase) [18, 19], and Golomb code (Polyphase) [20]). However, these analytical construction approaches only permitted sequences of a finite length to exist. The following investigations used computational techniques such the stochastic search method [21], exhaustive search method [22], and evolutionary algorithm [23] in an effort to get around the restrictions on sequence length. Although they pioneered the way for the synthesis of sequences of arbitrary length, their heuristic nature does not ensure convergence in terms of correlation sidelobe minimization, and they are not suitable for the development of lengthy sequences (i.e., $N > 10^3$) due to their rising computational cost with sequence length. More effective algorithms have been devised employing advanced strategies to address these issues, such as the Cyclic Algorithm New (CAN) [24] and the Monotonic Minimizer for Integrated Sidelobe Level (MISL) [25]. These algorithms allowed for the synthesis of lengthy sequences, i.e., $N \sim 10^6$ or even longer. The CAN algorithm was designed to construct long unimodular aperiodic sequences using the alternating minimization technique. It seeks to minimize a quadratic cost function that is almost equivalent to the original quartic cost function associated with the integrated sidelobe level (ISL) metric. Despite being computationally efficient, the solution to the approximate problem does not necessarily converge to the global minimum of the original problem. The MISL algorithm [25], in contrast to the CAN algorithm, minimizes a surrogate function of the original ISL minimization problem using the Majorization-Minimization (MM) framework [26]. It guarantees that the algorithm will eventually reach the global minima of the original problem. However, the original cost function's twofold majorization leads to slow convergence. Therefore, an acceleration approach (Accelerated-MISL) that significantly reduced the number of iterations has been presented in order to increase the convergence speed [25]. Later on, these methods have been modified to include zero correlation zone (also known as weighted integrated sidelobe level, or WISL) design, such as MWISL [27], and periodic sequence design, such as the PECAN algorithm [28].

A lot of study has been recently devoted to the construction of signals with low correlation sidelobes. Interior point approaches are used in [29] to generate low-sidelobe phase-coded waveforms, such as Barker sequences of any length. Other MM-based algorithms have been devised in [30,31] using a variety of objective functions. An algorithm using the Block MM framework to build an arbitrary length sequence with the goal of minimizing the ISL metric is proposed in [30]. In [31], a novel MM technique known as FISL is described, which employs a majorization function to achieve a tighter global upper bound than the original ISL based cost function.

In addition to the design of aperiodic and periodic sequences with low autocorrelation sidelobes, new approaches that investigate the design of sequences with desired stopbands, such as Stopband CAN (SCAN) and Weighted SCAN (WeSCAN) [13], have appeared in the literature. In fact, they are both derived from the CAN algorithm [24] mentioned previously. Their convergence is slow due to their computational cost (e.g., WeSCAN requires Eigen decomposition at each iteration). Steepest Descent based Cyclic Algorithm (SDCA) [32], despite it only offered a slight speed boost, has been presented as an enhancement to these cyclic algorithms. Recently, effective algorithms for producing unimodular sequences with appropriate spectral stopbands have been developed, including the Lagrange Programming Neural Network (LPNN) [33], Alternating Direction Method of Multipliers (ADMM) [34], gradient-based algorithms [35, 36], Spectral-MISL [25], Fast Fourier Transform based Conjugate Gradient Algorithm (FCGA) [37], and Stopband MISL-new (SMISLN) [38], where LPNN only applies to the construction of periodic sequences. Also, there are several research on constructing sequences based on binary constraint [39], Ambiguity Function [40], similarity [41], Peak to Average Power Ratio constraint [42], and Peak Sidelobe Level (PSL) [27, 43, 44] in the context of sequence design . A review of the important methods will be provided in Chapter 4.

The majority of the existing algorithms concentrate on achieving suppression levels for either frequency stopbands or correlation sidelobes that are better than what is possible with older techniques. As a result, the convergence speed has typically been of less importance. The natural waveform adaptivity feature of cognitive and spectrum aware systems, however, mandates the creation of waveforms in quick succession [45, 46]. In [37], Tang et. al. took this issue into account and developed the "FCGA," an effective conjugate gradient-based ISL and spectral stopband optimization algorithm, to speed up the synthesis of periodic and aperiodic unimodular sequences. The Polak-Ribiere-Polyak Conjugate Gradient method is utilized in the FCGA algorithm, which provides monotonic minimization of the objective function. In [37], Tang et. al. have also added a Taylor series expansion-based technique to efficiently determine a step length with a high degree of accuracy at each iteration.

Due to the fact that the phase gradient calculation and step length calculation are based on Fast Fourier Transform operations, the technique converges rather rapidly. Among the numerous contemporary techniques discussed above, FCGA is one of the state of art algorithms in terms of convergence speed. More recently, the Stopband MISL-New (SMISLN) algorithm has been suggested, which overcomes the optimization problem by employing an alternative MM approach for a deeper suppression of the correlation sidelobes and spectral stopbands [38]. Despite the authors' implementation of an accelerated version of SMISLN in [38], the algorithm becomes slower as the length of the sequence increases due to the sequence length dependent dimensionality of the matrix operations involved (high space complexity). Finally, it is noteworthy that an autocorrelation function that behaves like an impulse imposes a flat power spectrum. Therefore, it is difficult to satisfy both time and frequency domain restrictions (suppression of the spectral stopbands and the autocorrelation sidelobes) simultaneously.

In the context of waveform design applications, the new trends in radar domain, such as noise radar technology and cognitive radar necessitate waveform diversity. For example in noise radar technology, the waveforms with certain properties (noise-like characteristics, orthogonality, low autocorrelation sidelobes, Low Probability of Intercept/Exploitation, Peak-to-Average-Power Ratio (PAPR), etc.) shall either be generated in advance to form up a waveform library prior to radar mission or in (near) real-time by pseudo-noise generators/algorithms during active mission. From the military aspect, the waveforms of noise radar should be unpredictable and random from pulse to pulse and must allow for Low Probability of Intercept (LPI) radar operation. On the other hand, cognitive radars need to generate such (task-)optimized waveforms in adapting the active radar dynamically to the changing environment (clutter, spectrum congestion, target response, jamming etc.). Therefore, spectrum awareness is a primary feature of the cognitive radar, and the generation of a spectrally compatible waveform in cognitive radar applications can help the radar to tackle spectrum congestion and jamming issues while efficiently utilizing the spectrum. In this respect, the need for effective methods to control correlation sidelobes of noise waveforms and the Low Probability of Intercept/Exploitation requirement for military noise radar systems have motivated us to seek for an efficient method to generate noise-like signals with low integrated sidelobe level (ISL). Secondly, the demand for agile waveform generation for spectrum aware cognitive radars has motivated us to seek efficient optimization methods for the fast synthesis of spectrally compatible waveforms.

We note that throughout the thesis we use 'waveform' and 'sequence' interchangeably as the former is widely used in the context of radar whereas the latter is a more general term in the scope of signal processing.

1.3 Scientific Contributions and Research Publications

The major contributions of this thesis are summarized as follows:

(i) A novel algorithm named 'Combined Spectral Shaping and Peak-to-Average Power Reduction (COSPAR)' which embodies a parametric window function as a spectral weighting to control the autocorrelation sidelobes and a Peak-to-Average-Power-Ratio (PAPR) reduction technique inspired by a phase retrieval algorithm, is proposed to synthesize tailored low PAPR noise radar waveforms for enhanced Low Probability of Intercept (LPI) radar operation.

(ii) The sidelobe performance of COSPAR signals have been shown by field trials using the noise radar demonstrator system.

(iii) A visual analysis tool based on Spectral Kurtosis in the Time-Frequency domain is developed to assess the noise-like behaviour and pertinent LPI characteristics of the signal.

(iv) For the construction of spectrally compatible unimodular aperiodic/periodic sequences with minimal autocorrelation sidelobes, a new approach named "L-BFGS based Sequence Design (LBSD)" is developed, which is based on nonlinear optimization theory. The goal of this research is to find a more efficient approach to waveform synthesis that can be used in spectrum-aware cognitive radars. The algorithmic contribution is a nonlinear optimization method applied to the sequence design problem, together with a criterion for choosing the step size that improves the convergence rate of the iterative operation.

(v) Numerical simulations show that our proposed LBSD algorithm is better than existing methods in terms of how quickly it converges and how well it suppresses correlation sidelobes and spectral stopbands simultaneously.

In the course of our research, a number of publications were produced. The list of these publications is given as follows:

- A. G. Stove, G. Galati, F. De Palo, C. Wasserzier, A. Y. Erdogan, K. Savci, K. Lukin, "Design of a Noise Radar Demonstrator," *17th International Radar Symposium (IRS)*, 2016, pp. 1-6. doi: 10.1109/IRS.2016.7497328 [47]

- K. Savci, A. Y. Erdogan and T. O. Gulum, "Software defined L-band noise radar demonstrator," *17th International Radar Symposium (IRS)*, 2016, pp. 1-4. doi: 10.1109/IRS.2016.7497330 [48]

- K. Savci, A. G. Stove, A. Y. Erdogan, G. Galati, K. Lukin, G. Pavan, C. Wasserzier, "Trials of a Noise-Modulated Radar Demonstrator – First Results in a Marine Environment," *20th International Radar Symposium (IRS)*, 2019, pp. 1-9. doi: 10.23919/IRS.2019.8768194 [49]

- K. Savci, A.Y. Erdogan, "Digital Correlator: A Scalable and Efficient FPGA Implementation for Radar Receivers," *Signal Processing Symposium (SPSYMPO)*, 2019, pp. 207-211, doi: 10.1109/SPS.2019.8882091 (Awarded, 3rd Place in the "Young Scientist Contest") [50]

- N. Cotuk, A. H. Kayran, A. Aytun, K. Savci, "Detection of Marine Noise Radars with Spectal Kurtosis Method," *in IEEE Aerospace and Electronic Systems Magazine*, vol. 35, no. 9, pp. 22-31, 1 Sept. 2020, doi: 10.1109/MAES.2020.2990590 [51]

- K. Savci, A. G. Stove, F. De Palo, A. Y. Erdogan, G. Galati, K. A. Lukin, S. Lukin, P. Marques, G. Pavan, C. Wasserzier, "Noise radar – Overview and Recent Developments," *IEEE Aerospace and Electronic Systems Magazine*, vol. 35, no. 9, pp. 8-20, 1 Sept. 2020, doi: 10.1109/MAES.2020.2990591. [52]

- F. De Palo, G. Galati, G. Pavan, C. Wasserzier, K. Savci,"Introduction to Noise Radar and Its Waveforms," *MDPI Sensors*, 2020, 20(18), 5187, doi: 10.3390/s20185187 [53]

- G. Galati, G. Pavan, K. Savci, C. Wasserzier, "Noise Radar Technology: Waveforms Design and Field Trials," *MDPI Sensors*, 2021, 21(9), 3216, doi: 10.3390/s21093216 [54]

- K. Savci, G. Galati, G. Pavan, "Low-PAPR Waveforms with Shaped Spectrum for Enhanced Low Probability of Intercept Noise Radars," *MDPI Remote Sensing*, 2021; 13(12), 2372, doi: 10.3390/rs13122372 [55]

- G. Galati, G. Pavan, K. Savci, C. Wasserzier, "Counter-Interception and Counter-Exploitation Features of Noise Radar Technology," *MDPI Remote Sensing*, 2021; 13(22), 4509,doi: 10.3390/rs13224509 [56]

- K. Savci, "A Limited Memory BFGS Based Unimodular Sequence Design Algorithm for Spectrum-Aware Sensing Systems," *IEEE Access*, 2022, doi: 10.1109/ACCESS.2022.3192848 [57]

1.4 Thesis Outline

This thesis mainly addresses the waveform design methods including the generation of noise-like signals for noise radar technology and the generation of spectrally compatible waveforms for spectrum aware radar systems i.e., cognitive radar. We refer to the concepts of noise radar technology and cognitive radar and in particular, we treat them from the waveform point of view. Further in our work, we attempt to balance a practical point of view with a rigorous mathematical approach supported by a wealth of rich numerical examples and some real experiments. The remaining chapters of the thesis are organized as follows:

In chapter 2, we provide an introduction to the recent trends in radar techniques and applications i.e., noise radar, cognitive radar over the past decade to give insight on concepts being developed for wide range of radar applications. We highlight the significance of transmit waveform and their potentional performance benefits within the concepts of noise radar technology and cognitive radar.

In Chapter 3, we introduce the preliminaries in the context of waveform design. The matched filter and its optimality is discussed. The performance of matched filter in comparison with inverse and Wiener filtering is shown for radar applications. Then, the waveform performance metrics are defined which typically form up the constraints of the related objective functions in most waveform optimization problems. The ambiguity function of a signal is presented with regards to resolution and ambiguities in range and Doppler space.

Chapter 4 serves as an introduction to the background of waveforms and their design methods. We present a review of waveform design techniques and methods available in literature. First, we go through the classical waveforms which are derived from algebraic formulations, and then we present the seminal computational waveform synthesis methods. The chapter addresses the strengths and weaknesses of existing algorithms in literature.

In Chapter 5, we propose an innovative waveform design algorithm named "Combined Spectral Shaping and Peak-to-Average Power Reduction (COSPAR)" for noise radars which allows us to control the autocorrelation sidelobes while boosting the LPI property of noise radars. In this chapter, we develop the steps of the COSPAR synthesis method, including a novel PAPR reduction method inspired from a Phase-Retrieval Algorithm. Additionally, we propose a visual tool based on Spectral Kurtosis to assess the LPI property of radar waveforms. This chapter mainly involves the research presented in [55].

In Chapter 6, we concentrate on designing unimodular periodic and aperiodic sequences with desirable spectral stopband properties and good correlation sidelobes, and we propose an effective algorithm based on a quasi-Newton optimization technique called the Limited Memory Broyden-Fletcher-Goldfarb-Shanno (L-BFGS) method. The suggested approach is known as the "L-BFGS based Sequence Design (LBSD) Algorithm" in this regard. The bi-objective (ACF sidelobe and spectral stopband restrictions) optimization problem is first scalarized into an unconstrained single objective optimization problem, and then it is considered as a nonlinear large-scale problem in order to construct the LBSD method. The L-BFGS approach is then used to effectively solve this nonconvex and nonlinear cost function, with the search direction determined by the two-loop L-BFGS recursion. The research presented in this chapter was originally published in [57].

Finally, Chapter 7 concludes the thesis by summarizing the main outcomes and contributions from this research. Furthermore, future research directions are highlighted.

Chapter 2

NEW TRENDS IN RADAR SYSTEMS

Active radar systems are widely used for detection of objects and estimation of object properties such as velocity, Radar Cross Section (RCS) in Civilian and Military applications. Active radars propagate electromagnetic waves into the scene (sky, land, sea) where objects reflect the signal back to the radar. When the reflected waves or echoes are intercepted by radar receivers, the distance between the object and radar can be estimated by measuring the round-trip time delay and moreover the velocity information of the object can be obtained if the Doppler frequency shift on the received signal can be measured. Today, radar systems are widely used for surveillance, air security, navigation, metrology, as well as remote sensing applications. A typical radar system operation is illustrated in Figure 2.1.

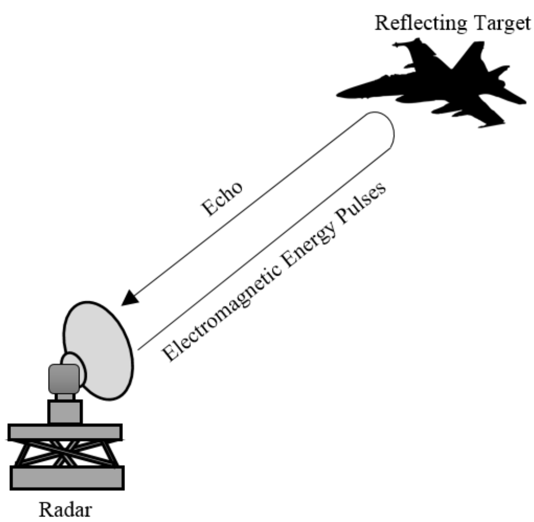

Figure 2.1: A typical radar operation.

The invention and initial development of radars date back to early 20th century. In 1904, Christian Hülsmeyer, a German engineer conducted first radar trials to detect ships on the river with his device called "Telemobiloscope" [58, 59]. Hülsmeyer demonstrated his invention to the German Navy for its potential for military use but failed to arouse any interest. Although there was simply no civilian or military need for radar until the early 1930s, with the advent of long-range military bomber aircrafts, major countries started to look for a means to detect hostile aircrafts. There has been significant progress in radar technology during the World War II. After the war, progress in radar technology slowed considerably. In the last couple of decades, innovations in solid-state radio frequency and telecommunication technologies and rapid growth in digital hardware paved the way for new approaches in radar domain.

Conventional radar systems have generally employed short pulses of high-energy waveforms or linear frequency modulated (LFM) chirp waveforms to perform target detection and obtain target range information. In the legacy conventional high power radar systems which have resonant cavity magnetrons/klystrons, spectrally inefficient, low duty-cycle sinusoidal wave pulses are widely used. Despite their low chance of interference, these short pulsed radars needed high voltage circuits, caused unintentional harmful x-ray transmission and had high failure rates. As an alternative to these radars, low power radars with solid-state power amplifiers that can transmit medium/high duty-cycle waveforms have been produced. In terms of military use; the disadvantage of high power radar systems' detection and identification by electronic support (ES) systems caused the invention of low power, solid-state low probability of intercept (LPI) radars. Low power, solid-state LPI radars use matched-filter and pulse compression techniques to reach the range resolution capabilities of short-pulse, high power radars. It is difficult for conventional ES systems to detect and identify these radars that use Frequency Modulated (FM)/ Phase Modulated (PM) waveforms which are suitable for pulse compression and which offer high processing gains with matched filters. However, there is an increasing number of research for detection and parameter extraction of LPI radars with digital ES systems with successful results [60].

Aside from military aspects, the increase in civilian radar applications such as navigation, autonomous systems, automotive radars, remote sensing, air and marine traffic control radars has brought out many issues such as mutual interference, spectral compatibility and spectrum sharing. With the new generation of low power solid-state transmitters, modern radar systems transmit medium or long pulses which makes them prone to interference. In spectrally crowded areas such as in maritime domain, the spectrum sharing and mitigation of interference is very important for the safety of ships at sea. In Figure 2.2, the maritime traffic over the Sea of Marmara is shown as an exemplary case for a spectrally crowded maritime domain.

Figure 2.2: Marine traffic in the Sea of Marmara - 28.08.2019 15:00 (GMT+3) (www.marinetraffic.com).

By transmitting either very short pulses in the case of a pulsed radar or a wide bandwidth signal in case of an LFM radar, good range resolutions can be achieved to separate small targets in range or to identify range extended targets. For pulse compression radars, the range resolution is defined as

$$\Delta R = c/2B \tag{2.1}$$

where c is the speed of light and B is the signal bandwidth. However even in high resolution radar systems, if there is a strong target near a weak target then the detection of weak target is hindered by the strong one. This means that the high correlation sidelobes of matched filter output might mask the correlation peak of the weak target. This is known as the masking effect in the radar literature [61].

To overcome these problems, the use noise radar technology is recommended by [62]. Noise radar refers to the techniques and applications that use random noise (narrowband or broadband) as the sounding signal and then perform correlation of radar returns for target detection and imaging. From the historical perspective, the concept of noise radar starts in 1950s. Bourret published the first paper on a range measuring noise radar system using an analog correlator [63]. Horton is generally regarded as the first to describe a complete design of a continuous wave (CW) noise radar [64]. Further papers on this topic were published in the 1960s and 1970s, which could be regarded as the initial of noise radar studies. The main advantages of noise radar are unambiguous in range and Doppler domain, spectral compatibility allows spectrum share, mitigation of mutual interference, low probability of intercept (LPI), low probability of identification(LPID) and low probability of exploitation (LPE) properties.

On the other hand , the RF spectrum congestion necessitates novel and innovative approaches that provide an intelligent and effective spectrum utilization taking into consideration the time-varying emitter activities in the operational arena. In this regard, the cognitive radar concept seems like a highly promising approach, especially in metropolitan areas and maritime domain where spectrum is severely crowded [65], and is essential to predict and counter new threats in today's dynamic and ever-changing environment. It is possible to dynamically and cognitively [1,66,67] select the probing waveforms in response to the changing conditions in order to enhance radar performance while controlling its impact on the other surrounding radio systems by relying on real-time situational awareness capability as well as new computing architectures, processors, arbitrary digital waveform generators, solid-state transmitters, active phased array antennas, etc. In the following sections, we will address the noise radar and cognitive radar techniques to introduce the reader with notions and mechanisms of these trending concepts.

2.1 Noise Radar Technology

The term "noise radar" refers to a radar system that broadcasts a signal that is unpredictable. Although the concept of noise radar has been around for sixty years [64], but practical interest in it expanded dramatically in the 2000s due to progress in radar technology that have made its benefits easier to exploit.

Returning to the fundamentals of radar is the best way to gain an understanding of Noise Radar Technology (NRT). Radar's primary purpose is to broadcast a radio signal and use the echoes of that signal to detect the existence of any target. In their most basic form, radars burst out a series of pulses with specific durations and repetition rates. Limits to the ranging mechanism are established by the nature of the radiated waveform. The pulse repetition rate specifies the unambiguous range. The radar range resolution in (2.1), which determines a radar's ability to discern two neighbouring targets, is governed by the signal's bandwidth B. For modulated signals, this means that the range resolution doesn't depend on the pulse duration. Even in the simplest situation of an unmodulated pulse, where the bandwidth is roughly equal to the reciprocal of the pulse width, the same equation holds.

An optimal signal-to-noise ratio can be achieved by employing a matching filter on a radar signal. The received signal and the signal that was transmitted are correlated by this filter [68]. An important metric for noise radars is the time-bandwidth product, BT, which is calculated by multiplying the bandwidth B by the integration time T of the correlator. Utilizing modulated signals has several advantages, including the detachment of the pulse duration from the range resolution and the ability to reduce the peak power of the radar pulse by an amount equal to BT without sacrificing range resolution. In many instances , this lower transmit power makes it possible to use solid-state transmitters. The ratio of the compressed signal's peak response to its range sidelobes' mean level is also equal to BT for simple noise-like signals. This ratio, known as the "Peak to Side Lobe Ratio" (PSLR), is crucial for continuous wave noise radars where large return sidelobes extend across the entire range swath.

Ideal NRT emissions are uniformly distributed in frequency and have an infinite duration. However, the ideal continuous white noise is of theoretical importance only because B and T are finite in practice. The primary constraints on available bandwidth are imposed by frequency regulations. For instance, S-band air traffic control radars must remain within the range of 2700 - 2900 MHz, whereas X-band marine radars are restricted to operating in the spectrum from 9300 to 9500 MHz. Other practical factors, such as hardware constraints, must also be taken into account when determining how much bandwidth to utilize when the requirements are less stringent.

There are essentially three constraints on the pulse integration time. The radar scene, which changes over time, is the primary source of constraint. For instance, a target's position may vary due to its motion. The rate at which the radar must provide information to the operator is the second limitation. When the radar has a rotator antenna, the integration time is also restricted by the amount of time it may dwell in a certain direction while scanning. The third restriction is that the antenna dwell time may be constrained to less than 100 ms due to the necessity to search over a wide angular sector and the usual coherence length of echoes from moving objects being on the order of 100 ms. Taking into account a typical bandwidth of 50 MHz and a hypothetical integration time of 20 ms, the processing gain BT is on the order of a million. Band-limited finite-duration noise is a favorable radar waveform in light of the aforementioned. It can be regarded as a non-repetitive signal code known only to the radar, but unpredictable to any adversary.

In the following subsections, we provide an overview of NRT's technical concepts, and outline the fundamentals of NRT and its distinct advantages over deterministic radars. Then properties of noise waveforms are discussed, including a discussion on tailored noise waveforms.

2.1.1 Noise Radars versus Conventional Radars with Deterministic Waveforms

A small selection of waveforms are utilized in "classical" radar transmissions [5, 68], sometimes known as "Deterministic Radar Technology" (DRT). NRT, on the other hand, uses a matched filter that is set up in real-time and can utilize a practically infinite number of waveforms in transmission that are realizations of a random process.

Resilience Against Electronic Warfare

The randomness of NRT signals improves the Low Probability of Intercept (LPI) property of radar signals against military ESM (Electronic Support Measures) and ELINT (Electronic Intelligence) systems [69]. Exploiting the radar signal, ESM and ELINT systems attempt to identify the specific emitter source by analyzing the signal and building "signal libraries." Low Probability of Exploitation (LPE) features are the strategies used to counteract these adversary interception, classification, identification and jamming activities. In these measures, NRT clearly outperforms DRT. In reality, there is little benefit to capturing the signals. Because the jamming signal cannot be easily produced as a replica of the radar signal, up-range false target jamming, in which the jammer creates deceptive false targets that are closer to the radar than the jammer, lacks the processing gain offered by DRT.

Mitigation of Mutual Interference

Interference between numerous radars coexisting in a confined environment and congested spectrum is minimized by the victim radar viewing the interference as noise, similar to CDMA (Code Division Multiple Access) modulation [70]. Reducing the likelihood of mutual radar interference may become increasingly significant in the future, particularly in marine and automotive radar. In the marine environment, the necessity to be able to operate in the presence of other signals will be driven by the usage of solid-state transmitters, which have significantly higher duty cycles than magnetron-based transmitters, causing interference due to signal overlap in time. It is expected that as the number of vehicles equipped with radar systems grows, as well as the number of radars installed in each vehicle, the probability of interference will increase. It is also crucial for Multiple-Input-Multiple-Output (MIMO) radars, which transmit orthogonal waveforms concurrently from several antennas of the same radar, to be able to generate a multitude of quasi-orthogonal waveforms sharing the same time/frequency domains [71].

Thumbtack Shape of the Ambiguity Function

A waveform's resolution in range (delay) and radial velocity (Doppler frequency) is characterized by its ambiguity function [72]. When both the period T and the bandwidth B are infinite, the shape of the ambiguity function for the perfect noise waveform is that of the Dirac delta function, which means that there are absolutely no ambiguities. However, as B and T are finite in practice, the peak is typically accompanied by sidelobes that have a mean level about $1/BT$ below the peak. As previously mentioned, these sidelobes are undesirable but unavoidable and can cause problems for noise radars. Therefore measures must be taken to manage these sidelobes.

In practical applications of noise radar, BT values can scale into the millions. A more reasonable BT of 64, which is a low value but chosen to make the features of the ambiguity diagram easy to perceive, is used to illustrate a typical ambiguity function for NRT in Figure 2.3.

The ambiguity function of a typical synthetic noise waveform is depicted in Figure 2.3. The delay axis is proportional to the signal length, and the Doppler is measured in radians per sample, hence the full-scale range is $+/-\pi$. The picture depicts the central peak (red) with an unstructured floor that is uniformly distributed across the range and Doppler with a mean level roughly 18dB below the peak.

Table 2.1 contrasts a deterministic Frequency-Modulated Continuous Wave (FMCW) waveform [73] with NRT. It is presumed that the FMCW radar uses a

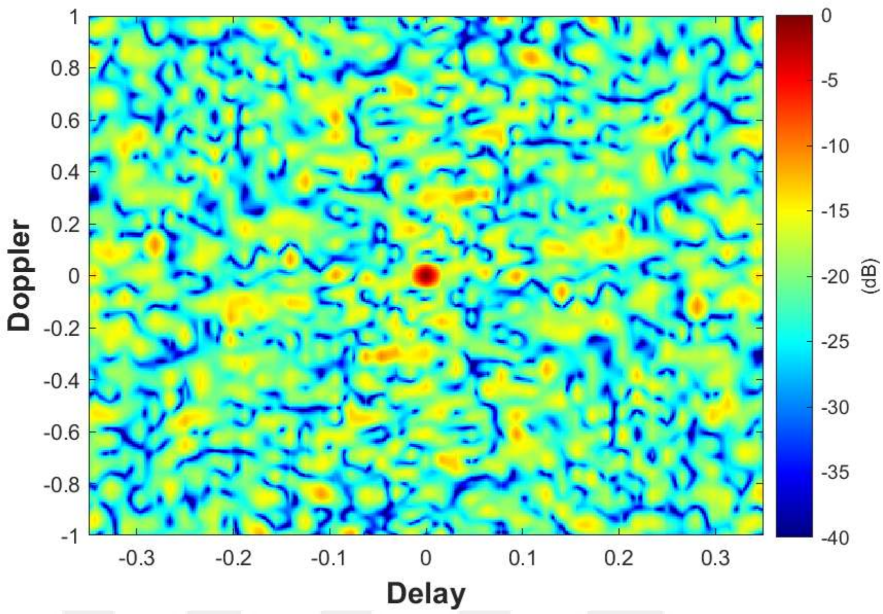

Figure 2.3: A typical ambiguity function of a noise signal.

linear sweep (Linear FM or LFM), which is the most common type of waveform in such radars. FMCW is chosen as a comparison since, like CW noise, it is a continuous signal that is generally used for its LPE capabilities or in situations where a simple radar using a continuous wave emitter is sought. These are the same kinds of applications that noise radar may be applied to, but FMCW is distinct from noise radar in that it utilizes a deterministic waveform.

2.1.2 Noise Radar Architecture

As previously noted, effective noise radar operation necessitates a large BT in order for: (I) the signals look like 'noise' i.e., random; (II) high range resolution to be attained; and (III) a small target to be visible in the presence of the pulse compression sidelobes of stronger signals. In addition to having a larger radar cross section (RCS), stronger targets may also have shorter ranges, resulting in lower path loss and potentially significant interfering returns due to the targets' sidelobes. As previously mentioned, the PSLR of the ambiguity function is restricted by BT, which may be on the scale of a million, resulting in a PSLR of 60 dB. This ratio is suffi-

Table 2.1: FMCW versus Noise Radar.

	FMCW Radar	**Noise Radar**
Range Accuracy	Affected by the target velocity and sweep linearity of the transmit signal.	Affected only by the transmit signal's bandwidth
Ambiguity Function	Range estimates for moving targets are influenced by the speed of the target.	Using a bank of correlators matched to different Doppler shifts, the distance to and speed of a target can be determined simultaneously.
Sensitivity	Affecting factors include antenna coupling, phase noise, and the side lobes of the FFT.	Affecting factors include antenna coupling and correlation sidelobes.
Electronic Protection (EP)	Inherent LPI, however the waveform that is being sent is continuously repeated, making it vulnerable to electronic attacks.	Inherent LPI, unpredictable signal transmission, and greater electromagnetic compatibility.
Signal Processing	Target range and velocity parameters are computed using coherent pulse trains and typical FFT processing.	Target range and velocity parameters are computed using 2D Correlation Filtering and a Range Filter Bank, as described in [9].
Spectral Efficiency	An up-chirp or a down-chirp are the only two waveforms that can theoretically occupy the same time and frequency range.	Two noise radars using the same transmission spectral band will have minimal mutual interference with one another.

cient for the majority of deterministic waveforms, because small targets only need to compete with the sidelobes of large targets at comparable range, but for a CW noise radar, where the sidelobes are spread over the whole range swath, the fluctuation in target echo with the "fourth power of range" must also be taken into account in the dynamic range requirements. Therefore, it is important to maximize both the bandwidth and the integration time, which leads to a preference for Continuous Emission (CE) waveforms with a 100% duty cycle, that is analogous to Continuous Wave (CW) in DRT. It should be noted that CE is also required to fully leverage the LPE feature, as the absence of trailing and leading edges makes extracting features from the signal extremely challenging for the opponent.

In this respect, the CE scheme leads to the following radar architectures shown in Figure 2.4. Figure 2.4a depicts the preferred radar architecture. The architecture in Figure 2.4a compromises the imperfections in transmitting channel, but it does come

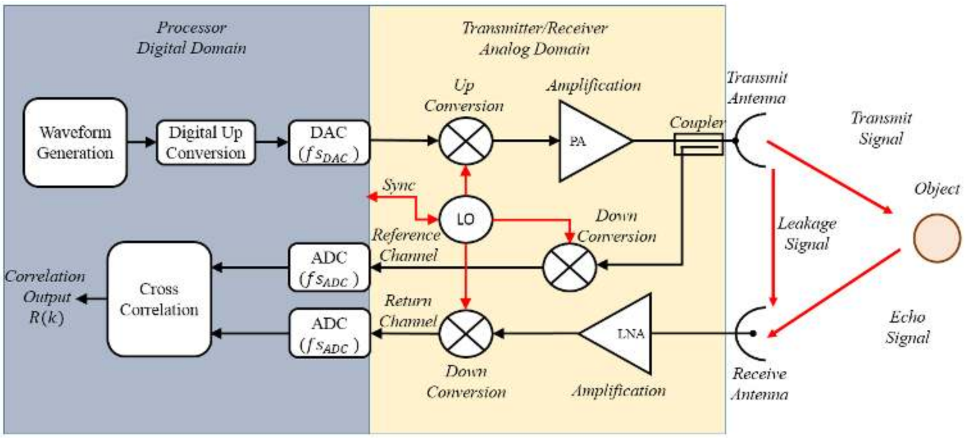

(a)

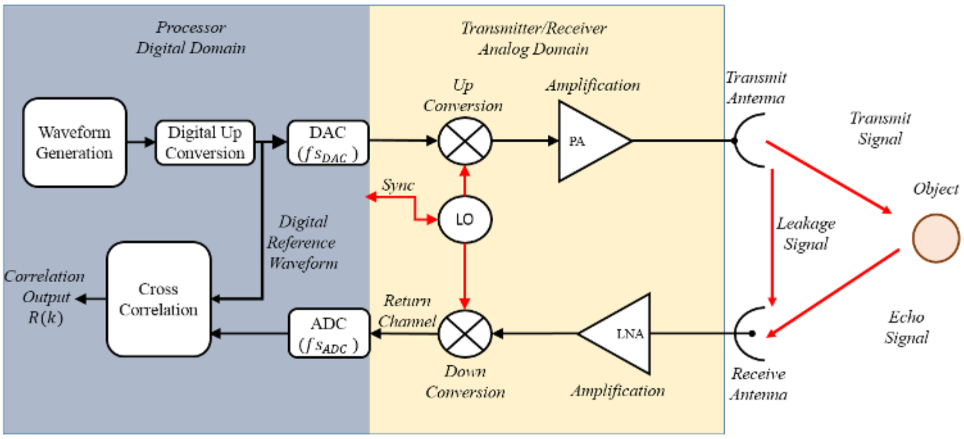

(b)

Figure 2.4: Noise radar block diagram : (a) with analog reference channel, (b) with digital reference channel.

at a cost, as it requires a wideband reference channel and an additional fast analog to digital converter (ADC). In Figure 2.4a, the correlator reference is a copy of the broadcast signal itself, accounting for all distortions in the analog circuitry up to the antenna port. These distortions, of course, compel us to prefer this more complex implementation alternative, despite the cost of a wideband reference channel with an extra analog-to-digital converter (ADC). As an alternate option, by employing a copy of the transmit code as the reference signal in the digital domain, this might be made simpler as shown in Figure 2.4b.

As expected, a major issue with continuous emission is the ”leakage” caused by antenna coupling from the transmitting to the receiving circuit (Figure 2.4). This effect, which is dependent on the antenna system and RF interconnections, is somewhat comparable to a strong target that is quite close to the radar (zero range). Due to the sidelobes of the radiated waveform's autocorrelation function, coupling has an impact on the operation of radar at near or medium ranges. Transmitting waveforms with low Range sidelobes is an efficient technique to mitigate this detrimental phenomena, in addition to appropriate antenna design.

2.1.3 Noise Radar Waveforms

The generation of the waveforms, which are realizations of an appropriate random process, is an important aspect in all NRT applications. The most 'obvious' way to obtain this signal is to begin with a physical noise source. This analog signal needs to be band-limited, modulated onto the radar's carrier frequency, and amplified before transmission. Direct usage of chaotic microwave oscillators as random signal sources for noise radars has also been reported [74]. Due to restrictions on accuracy, resolution, and dynamic range, analog generation methods is frequently impractical. As is the case with the majority of cryptography applications, digital implementation is recommended.

Digital Noise Waveforms and Pseudo-Random Noise Generators

Digital noise waveform implementation, or the usage of a pseudo-random number generator (PRNG), has long been the preferred method of implementing noise [75]. If pseudo-noise sequences are utilized in place of pure noise, one might assume that the desirable LPI/LPE capabilities of NRT, which depend on the randomness of the signals, would be impaired. Nevertheless, it is now quite simple to produce pseudo-random signals with enough complexity to render signal analysis useless. For instance, the Mersenne Twister PRNG [76] may produce signals for up to 2^{19937} samples, or repeat itself after 1.36×10^{5994} years with a sample rate of 100 MHz (or mega samples per second). The additional criticism that some PRNG algorithms are not "cryptographically secure" is irrelevant in NRT because the adversary can access the only the signal rather than the modulating code, which is subject to distortion from interference in the monitored band, multipath, etc. Additionally, if we take into account a typical military radar mission where the adversary ESM system may analyze signals for up to 1000 seconds, the radar, operating at the aforementioned rate of 100 MSPS, generates roughly 10^{11} samples during this time. In this regard as well, breaking the code seems not possible.

Pure Gaussian sequences, or digital representations of complex envelopes with Gaussian statistics, aren't necessarily the best option for NRT systems. They suffer from two practical issues: (I) The majority of radar transmitters run in saturation, that is, with a constant envelope throughout the emission. The penalty for a hypothetical linear operation could be as big as $10-12$ dB in transmission power efficiency. (II) The correlation processing produces sidelobes with mean amplitudes of the order $1/BT$ below the peak response of the compressed signal, as was mentioned in the previous sections.

Due to these two considerations, it is crucial to be able to produce optimized (tailored) pseudo random waveforms that have the following characteristics: (I) a peak to average power ratio (PAPR) that is equal to or almost equal to unity (for optimal utilization of the transmitter power), (II) minimal sidelobes in range and Doppler space. These waveforms obviously differ greatly from band pass, Gaussian noise realizations. Consequently, the issue of their level of unpredictability arises. The important query, which relates to their LPE characteristics, might be rephrased as follows: "How much knowledge of the signal's type and parameters can be derived from the analysis of increasing numbers of samples from the radar transmission?" In terms of information theory, where a measure of the information contained in a signal is related to the concept of entropy, a generic answer for an ideal ELINT/ESM system may be found. The Mutual Information Rate (MIR), or the additional information that is observed when one more sample is examined, must be assessed in order to guarantee that proposed waveforms have excellent LPI/LPE features.

Optimized (Tailored) Noise Waveforms

the PRNG based noise radar signals lack certain features such as inability to control correlation sidelobes and PAPR of the signal. For instance, by default, their mean sidelobe levels are of the order $1/BT$ with respect to the mainlobe of the compressed signal. Therefore, optimization based computational approaches are proposed to shape (tailor) the autocorrelation function in order to attain some desired qualities [53, 77].

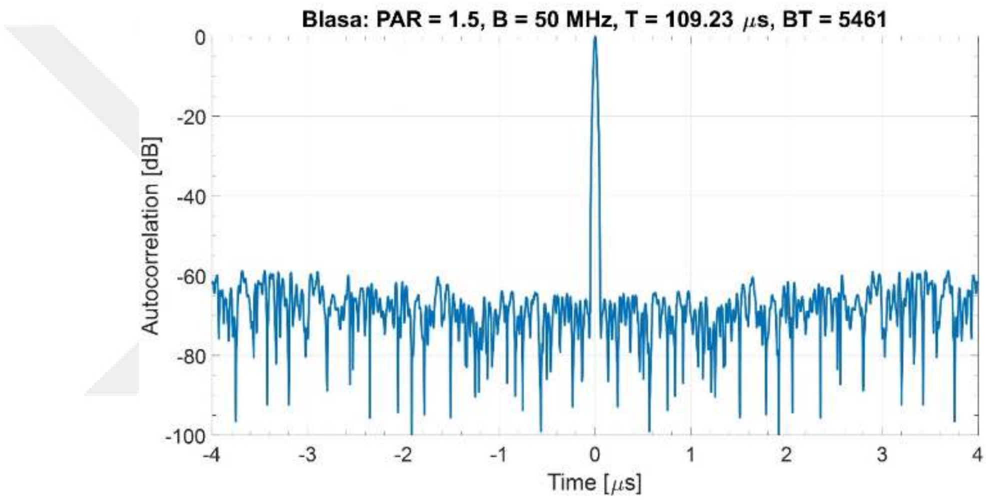

Figure 2.5: BLASA waveform. $PAPR = 1.5$, Compression loss in SNR $= -1.76dB$

For the purpose of generating tailored noise signals, the Cyclic Algorithm New (CAN) family of algorithms can be utilized [3]. These group of algorithms are based on alternating minimization, and approximation to a unit modulus, the region of suppressed sidelobes, and the mainlobe width can all be the considered constraints to be satisfied within this minimization. The CAN algorithms' primary weakness is that they tend to generate signals with flat PSD i.e., the bandwidth of the signal grows as the alternation proceeds.The spectrum constraint is considered in another cyclic algorithm, Stopband CAN (SCAN). The SCAN method has the disadvantage that the sidelobes near to the mainlobe are still large due to the sharp stop band edges.

To overcome this issue, De Palo et.al. [77] proposed the BLASA (Band-Limited

Technique for Sidelobes Attenuation) algorithm to generate band-limited noise signals. An exemplary BLASA signal with a PAPR of 1.5 is given in Figure 2.5. Note that $-10\log(BT) = -37.3$dB, however, owing to the optimization step, the mean of sidelobes is on the order of -70dB as seen in Figure 2.5.

In fact, many contemporary waveform design algorithms mentioned in Section (1.2) can be employed to generate signals for noise radars depending on the desired properties. These computational approaches and their construction methods will be addressed later in Section (4.2).

2.2 Cognitive Radar

The concept of Cognitive Radar is introduced by Haykin for the first time, along with some of its possible application domains [1]. As defined by the dictionary, Cognition is "acts of knowing, perceiving, or conceiving". The human visual system, in fact can perform the tasks of target recognition and tracking at speeds much above those of any conventional radar device [1]. Three key characteristics of a cognitive radar are listed below, as was done in [78]:

(i) acquiring knowledge via the radar's interactions with its surroundings and intelligent signal processing.

(ii) Receiver-to-transmitter feedback for intelligence

(iii) Analyzing the information contained in radar signals using the Bayesian approaches in target detection and tracking

Radar propagates a signal into the surroundings, and then, using the radar returns, creates a picture of the environment. Radar is accountable for both detecting radar returns and initiating the event resulting from radar returns [1]. Upon first sensing the environment via radar returns, a radar system begins data collection to establish a baseline understanding of its surroundings. The radar system makes a decision on which unknown targets to focus on during each scan interval. Targets are recorded once the receiver has spotted and identified them. However, it is unnecessary to store every single radar recording ever made.

Adaptability is a step toward fully eliminating radar record storage from the past. In contemporary radar system designs, the circuitry of the receiver is often adapted to the radar environment. Adaptability must be expanded to the radar's transmitter for it to function intellectually. Radar could also draw on its store of historical information to better deal with targets of varying types, such as airplanes, helicopters, ships, etc. at different ranges.

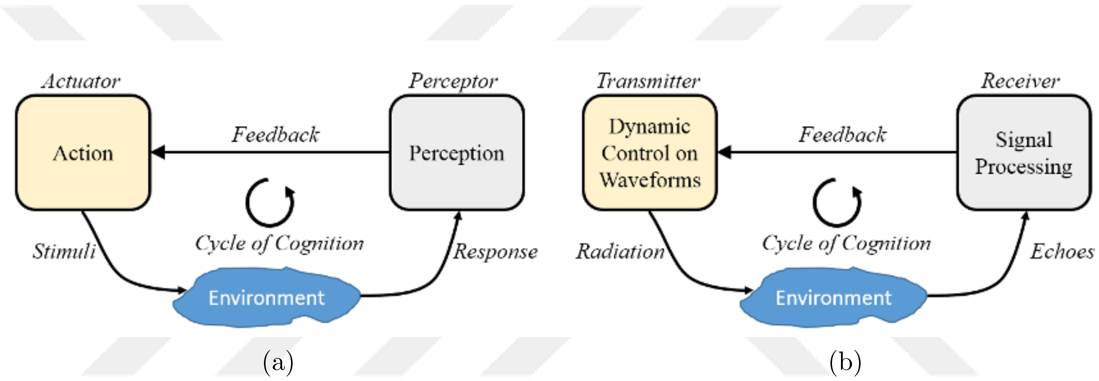

Figure 2.6: Cycle of Cognition: (a) for humans, (b) for radars.

Haykin poses the question, "What can we learn from the visual brain to dramatically improve the information-processing capability of conventional radar?" The cognitive radar (CR) is a novel hypothesis that uses the bat's echo-locating mechanism and, later, the visual brain to provide an answer to this fundamental question [[78]. The vast amount of research on the visual system that has been published in the field of neuroscience is the real reason for the focus on the visual brain.

Perception-Action Cyle

CR structure, functionality, and dynamics are shown in Figure 2.6 However, attention and intelligence are algorithmic procedures that are dispersed across the CR structure, rather than occupying a single location as memory and perception-action do.

A appropriate transmit waveform is picked from the library of transmit waveforms based on the weights of the multi-scale memory components. This waveform is then broadcast into the surrounding space. The signal is then received by the receiver after being purposefully broadcast into space. The receiver then uses a Bayesian filter to initiate a state-space model based on these observations. At that time, the transmitter feedback is necessary for the perception-action loop to continue. This feedback data, which may be thought of as an error vector in the state estimate, is created in the radar receiver and sent back to the transmitter so that appropriate action can be taken in response to the radar environment. Once the cycle is complete, the transmitter will use an illuminating signal to exert indirect control over the receiver. Haykin selects Bellman's dynamic programming with the goal of optimum control in mind for this work. Since the perception-action cycle in Haykin's cognitive model consists of four functional blocks,

(i) Approximate Bayesian filter for environmental perception,

(ii) Feedback link through receiver to transmitter,

(iii) Approximate dynamic programming for received control,

(iv) State-space model of the radar environment.

Memory

Memory also plays a crucial role in the CR. The need for CR to learn from its interactions with the radar environment inspired this idea. Both the transmitter and the receiver may use multi-scale memory to do this. Both the receiver and the transmitter, as shown in Figure 2.7 , include a memory element that is in turn related to another memory element. Executive memory refers to the sender's memory, whereas perceptual memory describes the receiver's.

As can be seen in Figure 2.7 , the system model library, which is made up of a grid of points with each point representing a state transition and system-noise covariance in the system equation, is in turn related to the perceptual memory. It is possible to choose the perceptual memory as a kind of heterogeneous associative memory. This memory's primary goal is to correlate the points in the measurement space with those in the system model space.

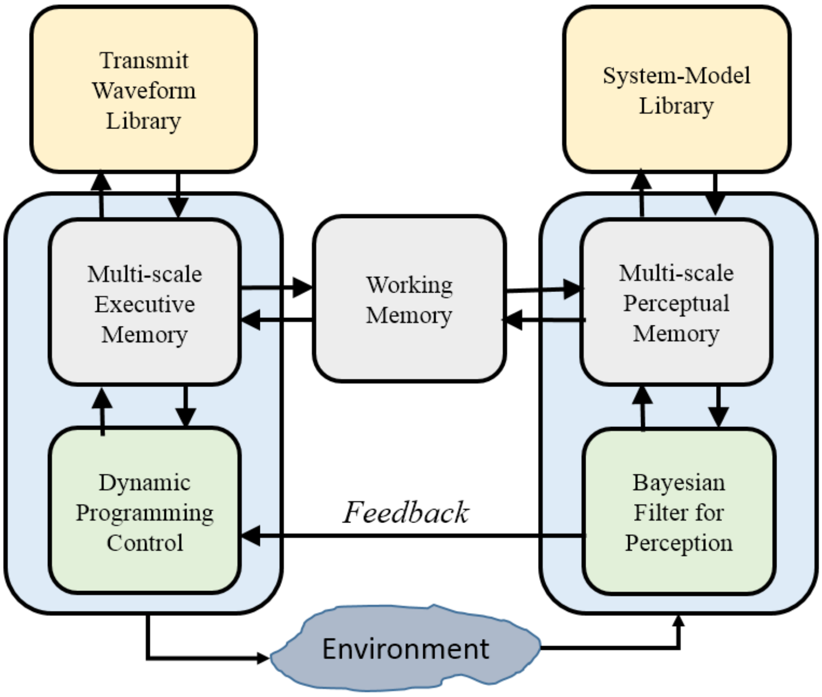

Figure 2.7: Haykin's Cognitive Radar with memory in [1]

The executive memory is another kind of memory that is found in the transmitter. The transmit-waveform library is another library that is related to this one in a similar fashion. Each dot on the grid represents a unique set of characteristics that together characterize the vector that represents the transmitted signal in one of these libraries. The executive memory is also an associative memory, but in this case the measurements and system-model library have been swapped out for feedback information and a send waveform vector.

As seen in Figure 2.7 , the working memory acts as a bridge between the perceptual memory and the executive memory, allowing the individual to make full use of both. Through linking our perceptual and executive memories, working memory serves as a restricted, devoted memory with limited storage capacity. In order to choose the working memory, a heterogeneous associative neural network is available. In the perception-action cycle, if a grid point in the system-model library is mismatched to the measurement vector, the working memory should fix the mistake on the following iteration. The same thing happens if a grid point in the transmitter's transmit waveform library is accidentally chosen.

Attention

As may be seen in Figure 2.7 , the PAC and memory occupy distinct locations inside the cognitive radar. However, algorithmic methods reveal perceptual and executive attentions at the CR receiver and CR transmitter, respectively.

As an example, the well-known explore-exploit strategy displays an important role in formulating an algorithm for the executive attention in a tracking problem. In order to show that, let's say, there is a grid point in the waveform library which was selected for transmission in the previous perception-action cycle. After that, this grid point is taken as a center point inside a cluster in the current cycle and neighbourhood of the center point presents the set of grid points. Over that set of points, the exploration phase is continued. The cluster of grid points is sent to the cognitive controller for illumination operation through the environment.

Intelligence

Compared to CR's attention process, intelligence does not have a fixed location. Therefore, intelligence manifests as an algorithmic system compelled by the attentional, memorization, and perceptual-attentional continuum (PAC). Since the other four pillars of cognition pale in comparison to intelligence, it is fair to claim that intelligence is the most valuable. To be more precise, the controller selects the effective transmit waveform by minimizing the cost function at the grid cluster level. In the course of the expedition, these grid points will be established. The receiver then determines the feedback vector.

In conclusion, cognitive radar offers a fresh perspective on the radars' ability to adapt. Target detection, target identification, and target classification are critical tasks that are carried out by the receiver side of conventional systems using intelligent signal processing methods and strategies. These adaptive systems use various adaptive approaches, including as receiver side beamforming and filtering, to reduce clutter and remove non-target replies. On the other hand, intelligence is sent to the transmitter section of cognitive radars through a feedback mechanism from the receiver, and this method enables the development of cognitive schemes to extract target information from the environment. Recent studies have shown that employing neural network architecture to learn about the radar environment improves target detection in real time using cognitive radar [2].

2.3 Summary

In this section, we have gone through the noise radar concept and briefly addressed the cognitive radar. From the waveform point of view, in [79] the cognitive active radars are described by

(i) cognitive active radars that work in a spectrally dense environment and change the transmitted waveform on the fly to avoid interference with the primary user of the channel, such as a broadcast or communication system,

(ii) cognitive active radars that adjust the transmitted waveform parameters to achieve a specified level of target tracking performance,

In either case NRT or cognitive radar, the waveforms are at the core of the radar system and modern radar systems demand for agile waveform generation capabilities.

Chapter 3

RADAR WAVEFORM DESIGN PRELIMINARIES

In radars, there are two factors that are critical to the system performance, i.e, the receive filter and the transmit waveform. This chapter describes the transmit waveform model, its processing via optimal receive filter i.e., the matched filter, the autocorrelation function, the ambiguity function and provides the background knowledge base required to understand the waveform design principles employed in the remainder of this thesis. The important applications of autocorrelation and the ambiguity function in terms of the understanding of specific waveform characteristics are demonstrated. The quality metrics, which are often involved in waveform optimization problem formulations, are introduced to evaluate radar waveforms.

3.1 Radar Signal Model

In this work, we concentrate our focus to baseband waveforms with the following modulations:

$$s(t) = \sum_{n=0}^{N-1} x(n)u_n(t), \quad 0 \leq t \leq T \tag{3.1}$$

where $\{x(n)\}_{n=0}^{N-1}$ is the modulating code sequence that is to be designed (which is assumed to be zero $\forall n \notin [0, N-1]$) and $u_n(t)$ is an ideal rectangular shaping pulse of time length t_u (thus $T = Nt_u$) described by

$$u_n(t) = \frac{1}{\sqrt{t_u}}\text{rect}\left(\frac{t - nt_u}{t_u}\right), \quad n = 0, ..., N-1, \tag{3.2}$$

where

$$\text{rect}(t) = \begin{cases} 1, \; 0 \leq t \leq 1, \\ 0, \; \text{otherwise,} \end{cases} \tag{3.3}$$

In fact, the original transmit signal is complex and has in-phase and quadrature components of $s(t)e^{2\pi f_c t}$ where f_c is the carrier frequency. It is assumed that the signal is demodulated at the receiver, and thus we can safely ignore the carrier term $e^{2\pi f_c t}$ in our analysis.

In practice, system components such as power amplifiers in the transmitter and analog-to-digital converters (ADCs) in the backend processor result in amplitude clipping when signal level is above some threshold level (1dB saturation point or maximum dynamic range). Thus, in order to maximize the power in the transmitted and received signal, unimodularity or low peak-to-average power ratio (PAPR) is desirable. Such unimodular sequences can be denoted by

$$x(n) = e^{j\theta(n)}, \quad n = 0, ..., N-1 \tag{3.4}$$

where$\{\theta(n)\}_{n=0}^{N-1}$ are phase samples distributed in $[-\pi, \pi]$. On the other hand, the signals with low peak-to-average power ratio have $PAPR \approx 1$ where PAPR is defined by

$$PAPR = \frac{max|x(n)|^2}{\frac{1}{N}\sum_{n=0}^{N-1}|x(n)|^2} \tag{3.5}$$

The probing waveform $s(t)$ is propagated through antenna into the scene and reflected by objects at different locations. Then, the return signal $y(t)$ that is received by the antenna, is a linear combination of a delayed and weighted version of transmit signal $s(t)$. The received (echo) signal is given by

$$y(t) = \sum_k z_k s(t - \tau_k) + n(t) \tag{3.6}$$

where τ_k is the lag (round-trip time) for the kth target, z_k is the complex valued coefficient related to the target properties, e.g., Radar Cross Section (RCS) and $n(t)$ is noise.

3.2 Optimal Matched Filtering and Correlation

Our goal is to estimate the property $z_{k'}$ of a k'th target in 3.6 at unknown distance corresponding to some round-trip time by applying the filter $w(t)$. Then, the estimation can be written as

$$\hat{z}_{k'} = \int_{-\infty}^{\infty} w(t - \tau_{k'}) y(t) dt \tag{3.7}$$

According to traditional convolution definition, (3.7) is the estimated output at time delay $\tau_{k'}$ when $w(t)$ is the filter and $y(t)$ is the input. Under the settings, where there is no clutter (unwanted echoes from ground, sea, etc.) and zero-mean white noise is assumed, replacing $w(t - \tau_{k'})$ with $s^*(t - \tau_{k'})$ will result in the the highest signal-to-noise (SNR) ratio at the output. In this case, this process is called "*Matched Filtering*" i.e. the rationale comes from that the filter weights are matched to the original transmit signal. Besides noise suppression, matched filter can also eliminate clutter if

$$R(\tau) = \int_{-\infty}^{\infty} s(t) s^*(t - \tau) dt, \quad -\infty < \tau < \infty \tag{3.8}$$

is zero $\forall \tau \neq 0$. $R(\tau)$ is called the *auto-correlation function* (ACF) of $s(t)$. For the discrete waveform sequence $\{x(n)\}_{n=0}^{N-1}$, the discrete ACF is defined as

$$r(k) = \sum_{n=k}^{N-1} x(n) x^*(n-k) = r^*(-k), \quad k = 0, ..., N-1. \tag{3.9}$$

where k denotes the lag index. For this auto-correlation sequence, $r(0)$ is termed as *in-phase correlation* and it is equal to the signal energy. Note that $r(0)$ or the signal energy is equal to N for unimodular sequences of length N. All the other auto-correlations at different lags for $\{k \neq 0, k = -N+1, ..., N-1\}$ are called *correlation sidelobes*.

Indeed, $\{r(k)\}_{k=0}^{N-1}$ defined in 3.9 constitutes the *aperiodic* auto-correlation function of $\{x(n)\}_{n=0}^{N-1}$. The *periodic* auto-correlation of the sequence $\{x(n)\}_{n=0}^{N-1}$ is defined as

$$\tilde{r}(k) = \sum_{n=0}^{N-1} x(n)x^*((n-k) \bmod N) = \tilde{r}^*(-k) = \tilde{r}^*(N-k), \quad k = 0, ..., N-1. \tag{3.10}$$

where "mod" denotes the modulo operator given as follows:

$$l \bmod N = \begin{cases} l - \lfloor l \,/\, N \rfloor N, & \text{l is not an integer multiple of } N \\ N, & \text{otherwise} \end{cases}, \tag{3.11}$$

Periodic ACF is often used in radars when continuous wave operation is employed whereas aperiodic ACF is often utilized in the case of pulsed operation. In periodic case, radar processing interval is equal to the CW transmission duration. In aperiodic case, radar processes a longer interval than the duration of the waveform as it is the typical case for long range radars.

In the remainder of the thesis, when we use the expression 'autocorrelation function' (or for the sake of brevity, the 'correlation function') we refer to signals' aperiodic correlation function unless we explicitly state the word 'periodic'.

Additionally, the matched filtering may also be computed in frequency domain. Given the discrete sequence $\mathbf{x} = \{x(n)\}_{n=0}^{N-1}$, the frequency domain computation of correlation $\mathbf{r} = \{r(k)\}_{n=0}^{\tilde{N}-1}$ is given as follows:

$$\mathbf{r} = \mathcal{F}_{\tilde{N}}^{-1}\{\mathcal{F}_{\tilde{N}}(\mathbf{x}) \circ \mathcal{F}_{\tilde{N}}^*(\mathbf{x})\} \tag{3.12}$$

where $\mathcal{F}_{\tilde{N}}(\cdot)$, $\mathcal{F}_{\tilde{N}}^{-1}(\cdot)$, $\circ$ and $(\cdot)^*$ represent, respectively, the $\tilde{N}$-point Fast Fourier Transform (FFT), the $\tilde{N}$-point Inverse Fast Fourier Transform (IFFT), the Hadamard product, and the complex conjugate operator. (3.12) denotes the aperiodic correlation when $\tilde{N} = 2N$ and the periodic correlation when $\tilde{N} = N$.

3.3 Comparison of Inverse Filter, Wiener Filter and Matched Filter Results in Radar Applications

In this section, we investigate whether the inverse Filter [80] and Wiener Filter [81] can be used instead of the well known matched Filter [82] in radar receivers. The disadvantages of inverse Filter and Wiener Filter are shown along with simulation results and finally a mathematical proof is given which demonstrates why matched filter is optimal and why it is adopted widely in radar receivers.

A pulsed radar transmits a signal the length of which is an order of a micro/millisecond and the transmit signal reflects back from the objects thereby the return signal is captured by the radar receiver. Let $s(t)$ denote the transmit signal. Then, the return signal can be modelled as the following

$$y(t) = \sum_k z_k s(t - \tau_k) + n(t) \tag{3.13}$$

where τ_k is the round-trip delay for the k^{th} target, z_k is the coefficient related to the target reflection (Radar Cross Section) and $n(t)$ is the noise.

Equation (3.13) can be regarded as the following system

$$y(t) = (h * s)(t) + n(t) \tag{3.14}$$

where $h(t)$ is the unknown impulse response of the scene we wish to observe with the radar. In frequency domain, this can be written as

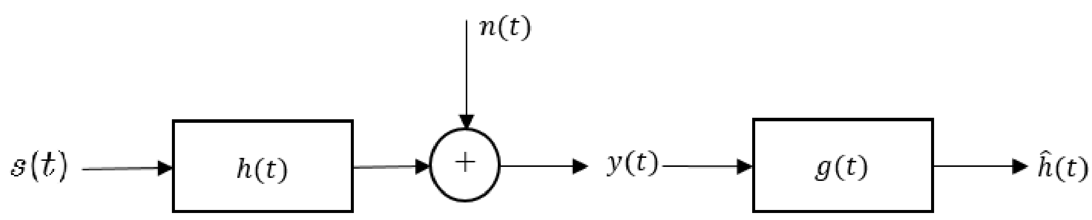

Figure 3.1: Radar signal and filter model

$$Y(f) = H(f)S(f) + N(f) \tag{3.15}$$

In general, the signal model and the filtering problem can be illustrated as in Figure 3.1.

In the ensuing subsections, we explain the aforementioned filtering methods and simulate the filtering results for low and high SNR cases in two scenarios depicted in Figure 3.3 and Figure 3.4 using the chirp signal shown in Figure 3.2. Note that in scenario-II, the reflected signal from the farther target is not captured to full extent as a part of this signal falls outside the instrumented range of the radar.

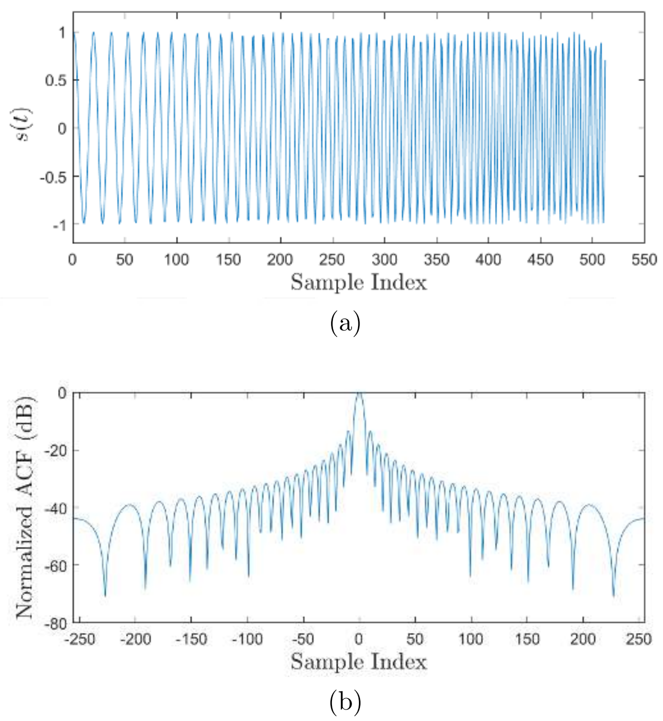

Figure 3.2: Chirp signal and its ACF: (a) Signal, (b) ACF.

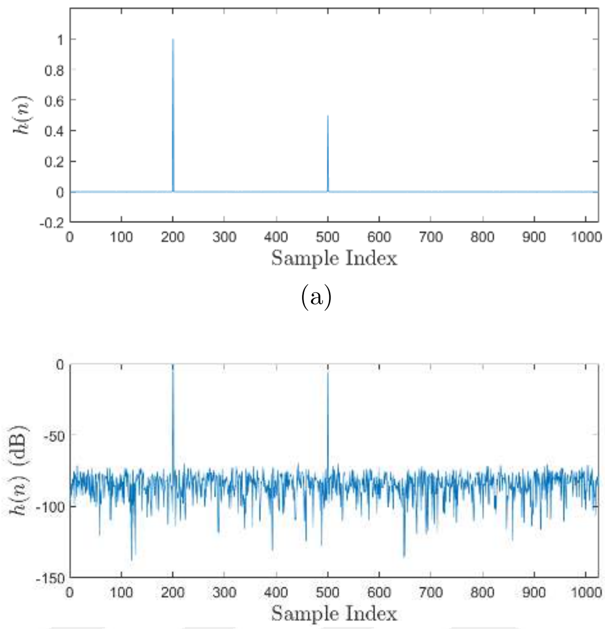

(a)

(b)

Figure 3.3: Scenario-I: Impulse response of the scene. Two targets are located at sample index 200 and 500, respectively. (a) Linear Scale, (b) Log Scale.

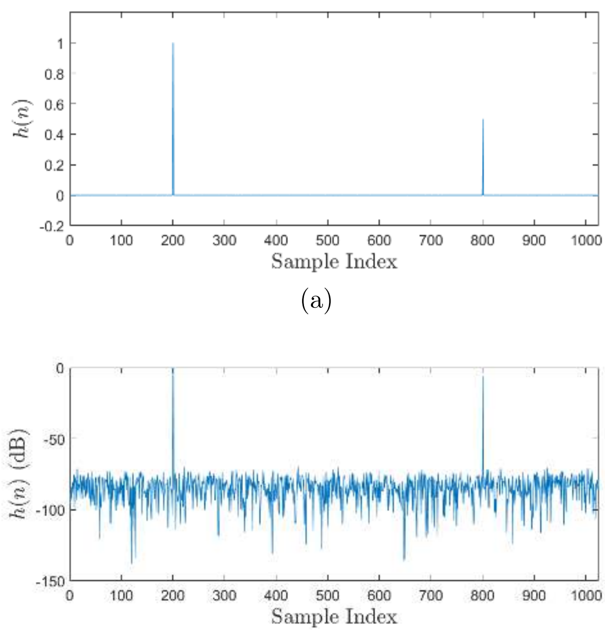

(a)

(b)

Figure 3.4: Scenario-II: Impulse response of the scene. Two targets are located at sample index 200 and 800, respectively. (a) Linear Scale, (b) Log Scale.

Inverse Filter

Neglecting the noise part, one can think that $h(t)$ can be estimated with an inverse filter $g(t)$ the description of which is given in the frequency domain as the following

$$G(f) = \frac{1}{S(f)} \tag{3.16}$$

Then the frequency domain estimation of $h(t)$ can be calculated as

$$\hat{H}(f) = Y(f)G(f) = \frac{Y(f)}{S(f)} \tag{3.17}$$

where $h(t)$ can be obtained by inverse Fourier transform of $\hat{H}(f)$. The method's fundamental flaw is that when $S(f)$ exhibits low-pass characteristics, $1/S(f)$ is a high-pass filter that grows in value with increasing frequency. As a result, (3.17) exhibits numerical instability for small $S(f)$ values and significantly boosts the contribution from high frequency noise. Due to this issue, even very small quantities of high frequency noise present in the measured signal $y(t)$ might cause significant distortion when using inverse filtering.

Limiting the frequency response $1/X(f)$ to some threshold γ is one way to cope with the noise sensitivity of an inverse filter.

$$G(f) = \begin{cases} \frac{1}{S(f)}, \text{ if } \frac{1}{S(f)} < \gamma \\ \gamma\frac{|S(f)|}{S(f)}, \text{ otherwise} \end{cases}, \tag{3.18}$$

Inverse filtering simulation results are shown in Figure 3.5-3.8b for high and low SNR cases per each scenario. The received signals in Figure 3.5-3.8a are obtained by convolving the chirp signal in Figure 3.2 with the impulse response of the scenes (See Figure 3.3 and 3.4), and then adding Gaussian noise. In high SNR case (SNR= 37 dB), the inverse filtering gives us acceptable solutions (see Figure 3.6b) although Signal-to-Clutter ratio is not retained at the output of the filter. In case of low SNR (SNR= 17 dB), the estimation of impulse response is highly distorted (see Figure 3.5b and 3.7b). When a part of the signal is not captured, even in the high

SNR case, it may easily lead to false target detection as shown in Figure 3.8b.

Wiener Filter

The Wiener filter is popularly used as a deconvolution method in signal processing. As opposed to inverse filtering, this technique aims to minimize noise while attempting to recover the original signal. In terms of mean square error, it achieves the ideal compromise between noise smoothing and inverse filtering. Presuming white Gaussian noise, the Wiener filter may be described in the Fourier domain using the following formula:

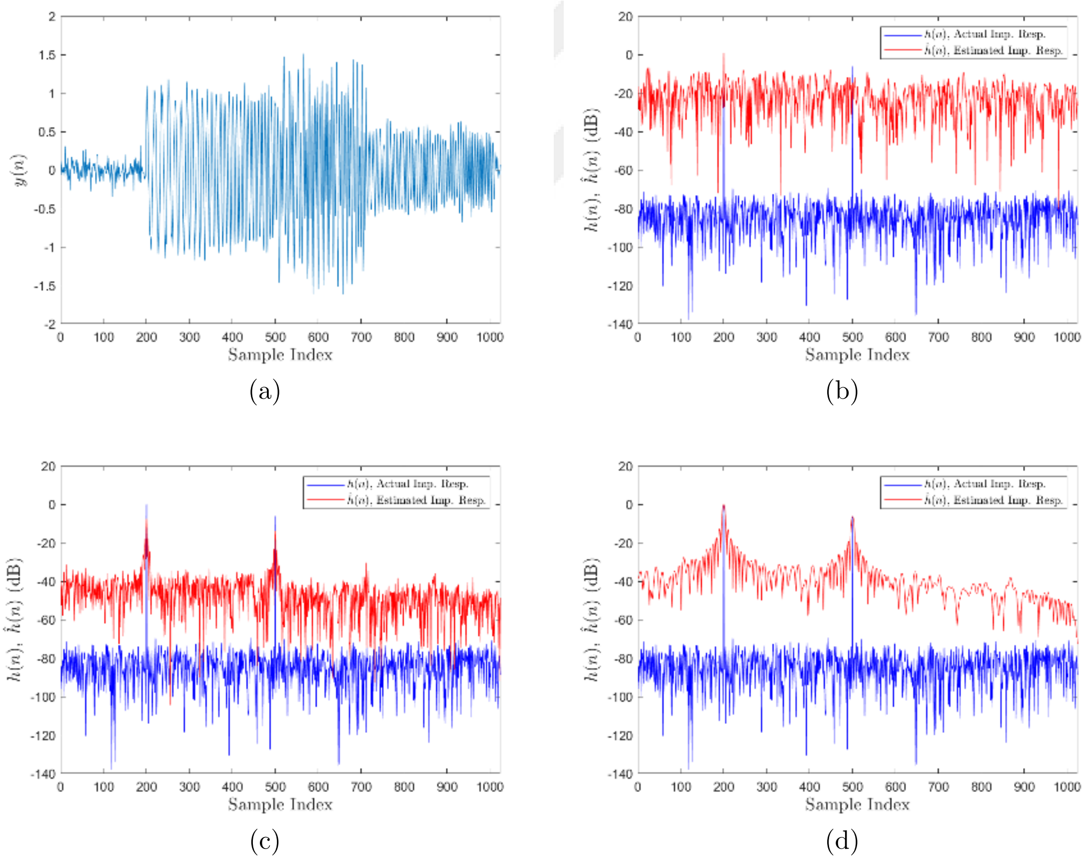

Figure 3.5: Simulation results for low SNR (SNR=17dB) case in Scenario-I : (a) Received Signal, (b) Inverse Filtering Output, (c) Wiener Filter Output, (d) Matched Filter Output.

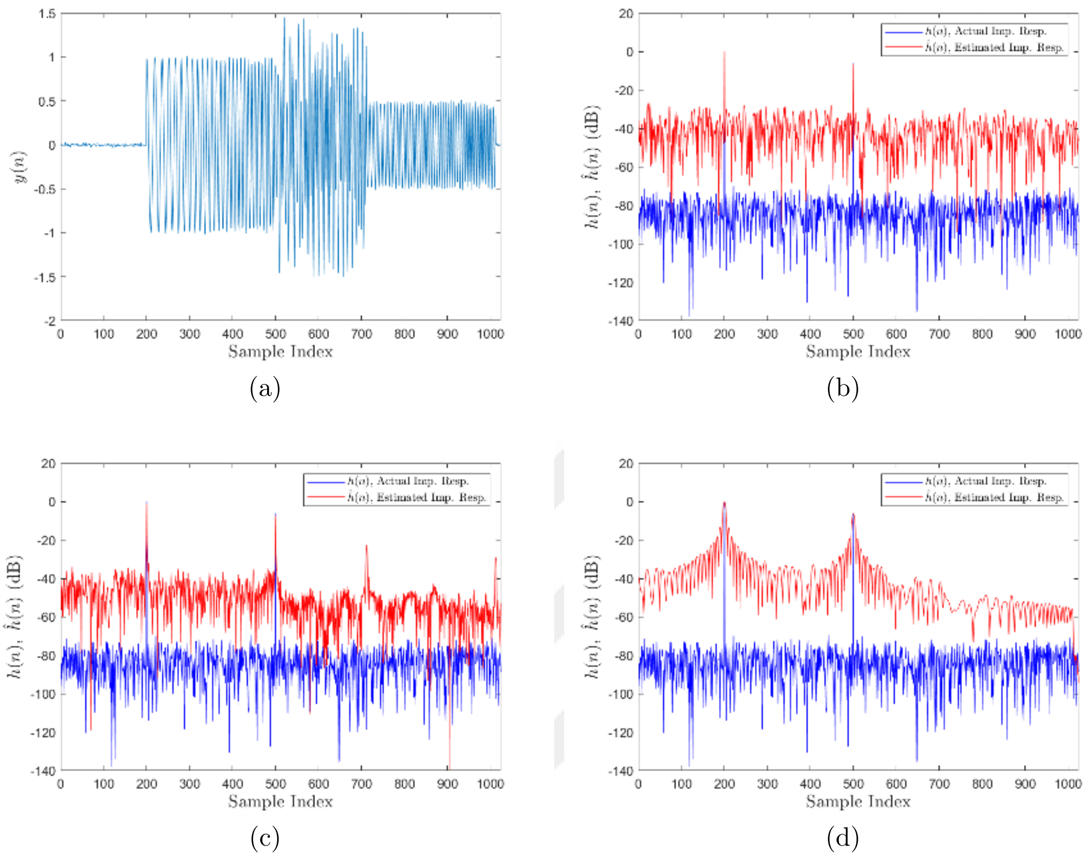

Figure 3.6: Simulation results for High SNR (SNR=37dB) case in Scenario-I : (a) Received Signal, (b) Inverse Filtering Output, (c) Wiener Filter Output, (d) Matched Filter Output.

$$W(f) = \frac{S^*(f)}{|S(f)|^2 + P_n(f)} \tag{3.19}$$

where $P_n(f)$ is PSD of noise. Then the frequency domain estimation of $h(t)$ can be calculated as

$$\hat{H}(f) = W(f)Y(f) \tag{3.20}$$

where $h\hat{(t)}$ can be obtained by the inverse Fourier transform of $\hat{H}(f)$. Wiener filtering simulation results are shown in Figure 3.5-3.8c for two scenarios under different SNR cases. It is observed that the impulse response estimation includes false targets at the output due to that Wiener filter is sensitive to noise estimation. When some part of the signal is missing (not captured completely) then the estimation of impulse response is highly distorted which may easily lead to false target detection as seen in Figure 3.6c and 3.8c.

Matched Filter

We can rewrite (3.13) as the following

$$y(t) = \underbrace{z_{k'}s(t-\tau_{k'})}_{target\ echo} + \underbrace{\sum_{k\neq k'} z_k s(t-\tau_k)}_{clutter} + \underbrace{n(t)}_{noise} \tag{3.21}$$

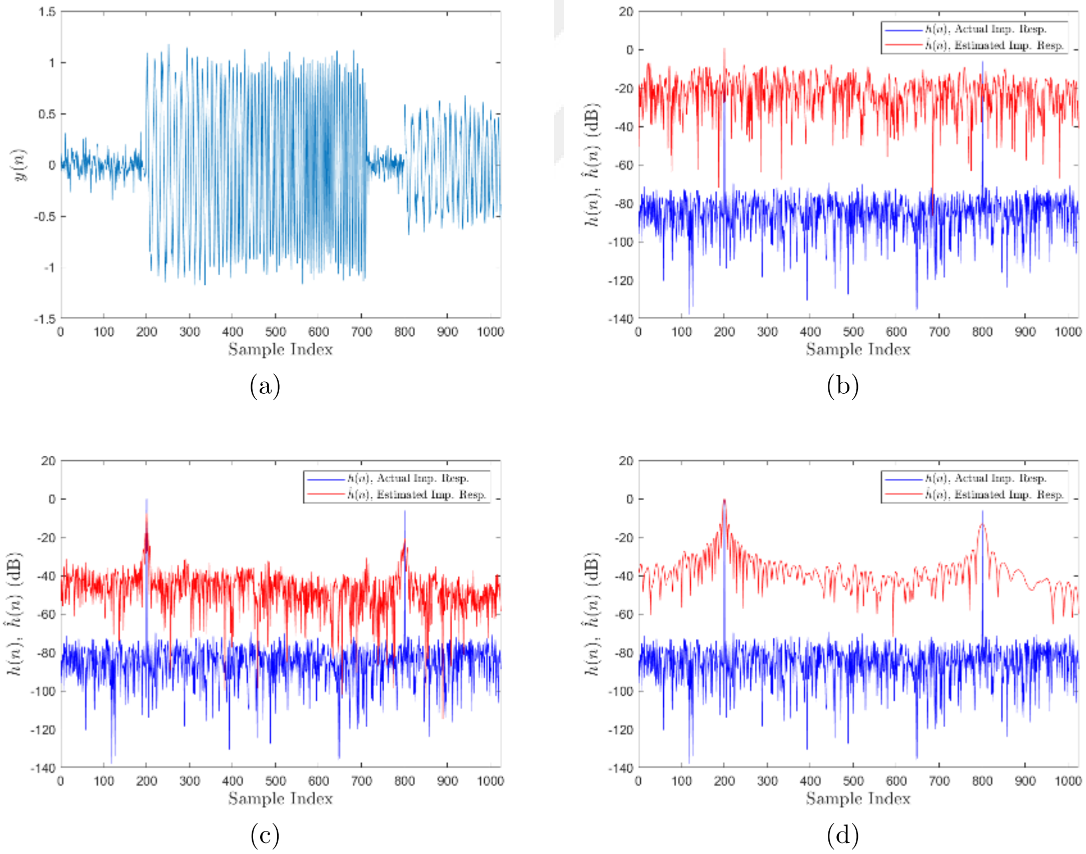

Figure 3.7: Simulation results for low SNR (SNR=17dB) case in Scenario-II : (a) Received Signal, (b) Inverse Filtering Output, (c) Wiener Filter Output, (d) Matched Filter Output.

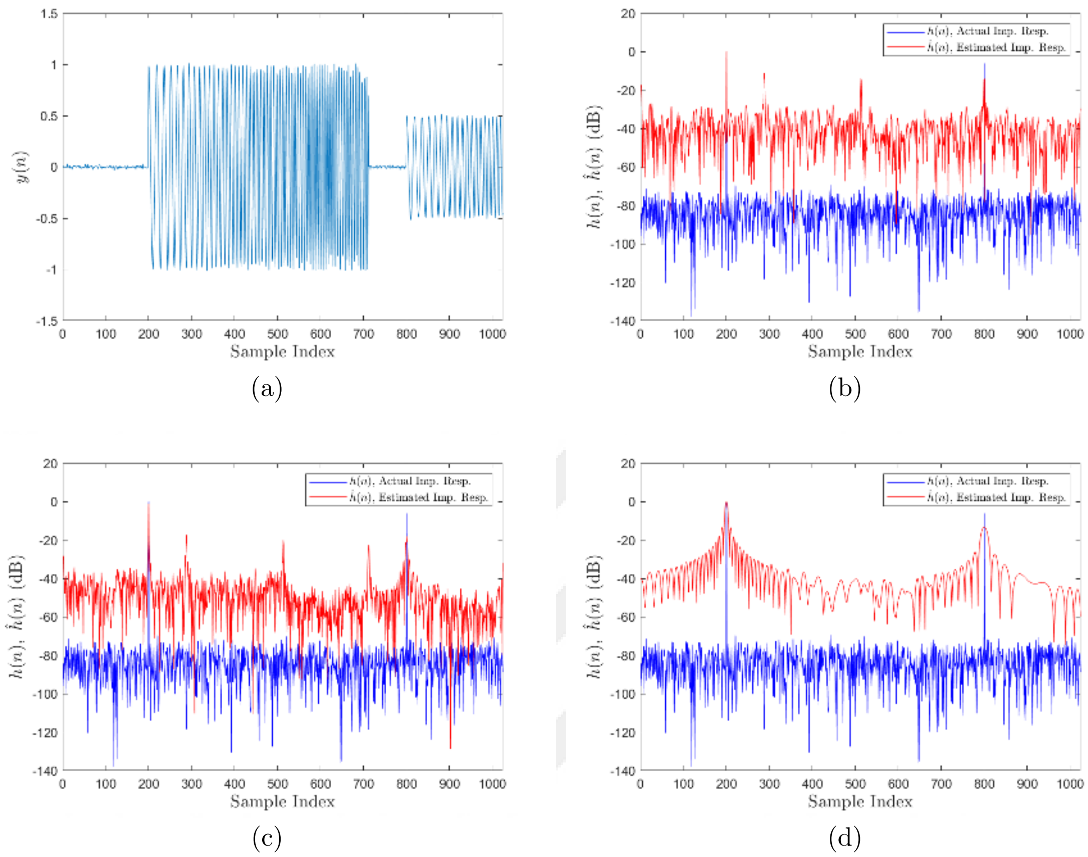

Figure 3.8: Simulation results for high SNR (SNR=37dB) case in Scenario-II : (a) Received Signal, (b) Inverse Filtering Output, (c) Wiener Filter Output, (d) Matched Filter Output.

In (3.21), when there is no clutter and $n(t)$ is the zero-mean white noise then the filter in (3.7) with $w(t-\tau_{k'}) = s^*(t-\tau_{k'})$ will give the highest signal-to-noise ratio (SNR). A proof is given below.

$$\begin{aligned} SNR &\cong \frac{\left|\int_{-\infty}^{\infty} w(t-\tau_{k'}) z_{k'} s(t-\tau_{k'}) \mathrm{dt}\right|^2}{E\left[\left|\int_{-\infty}^{\infty} w(t-\tau_{k'}) n(t) \mathrm{dt}\right|^2\right]} \\ &= \frac{|z_{k'}|^2 \left|\int_{-\infty}^{\infty} w(t-\tau_{k'}) s(t-\tau'_k) \mathrm{dt}\right|^2}{\sigma_n^2 \int_{-\infty}^{\infty} |w(t-\tau_{k'})|^2 \, \mathrm{dt}} \\ &\leq \frac{|z_{k'}|^2 \int_{-\infty}^{\infty} |s(t-\tau'_k)|^2 \, \mathrm{dt}}{\sigma_n^2} = \frac{|z_{k'}|^2 \sigma_s^2}{\sigma_n^2} \end{aligned} \tag{3.22}$$

Where E represents the expectation operator and σ_s^2 and σ_n^2 are the signal and noise power, respectively. The second line in (3.22) stems from the white noise assumption $\mathrm{E}\left(n(t_1)n^*(t_2)\right) = \sigma_n^2 \delta_{t_1-t_2}$, and the third line in (3.22) comes from the Cauchy-Schwartz inequality i.e., $\left|\int w(t-\tau_{k'}) s(t-\tau'_k) \mathrm{dt}\right|^2 \leq \int |w(t-\tau_{k'})|^2 \, \mathrm{dt} \int |s(t-\tau'_k)|^2 \, \mathrm{dt}$. The maximum value of the SNR is obtained only if the filter $w(t-\tau_{k'})$ is a scaled version of $s^*(t-\tau'_k)$, which proves the optimality of the matched filter.

To normalize the output, the matched filter $w(t-\tau_{k'})$ is chosen as $s^*(t-\tau'_k) \ / \ \int |s(t)|^2$ and the corresponding estimate of $z_{k'}$ is given by

$$z_{k'} = \frac{\int_{-\infty}^{\infty} s^*(t-\tau'_k) y(t) \mathrm{dt}}{\int_{-\infty}^{\infty} |s(t)|^2 \, \mathrm{dt}} \tag{3.23}$$

The matching filter may also remove the clutter component in addition to enhancing the signal component and reducing the noise component (as easily seen from (3.21) and (3.23)) if the ACF of $s(t)$

$$R(\tau) = \int_{-\infty}^{\infty} s(t) s^*(t-\tau) \mathrm{dt}, \quad \infty < \tau < \infty \tag{3.24}$$

is zero $\forall \tau \neq 0$.

Discussion

Inverse filtering and Wiener filtering seems quite sensitive to noise as seen in the simulations and signal-to-clutter ratio is not retained after filtering. Furthermore when the reflections from targets or the echo signals are partly captured, the filtering produces arbitrary spikes (false targets) at the output.

The filter weights that are set to the conjugated time-reversed version of the template signal give us the highest signal-to-noise ratio (SNR) at the filter output under the conditions where there is no clutter (unwanted echoes from the ground or sea) and the received radar signal is contaminated by zero-mean white noise. Since the filter weights are matched to the transmit signal in this instance, the filtering is optimum and is known as 'Matched Filtering'. If the correlation range sidelobes are kept to a minimum, matching filter can reduce clutter in addition to noise. According to simulations, matched filtering offers effective noise suppression at the output. Signal-to-noise ratio is preserved at the filter's output when the transmit waveform has low sidelobes.

Lastly, it should be noted that Matched filter may also be Doppler-tolerant (can still output target response when frequency shift is imposed on return signal) when the waveform is carefully designed [83].

3.4 Metrics Based on Auto-Correlation Function

In the previous sections, the benefit of small auto correlation sidelobes $r(\tau)$ (for $\tau \neq 0$) has been outlined. In this section, we introduce the metrics related to autocorrelation function which are extensively used in many waveform optimization algorithms. The algorithms which utilize these metrics will be discussed later in Section 4. An exemplary autocorrelation function and its lateral lobes are illustrated in Figure 3.9.

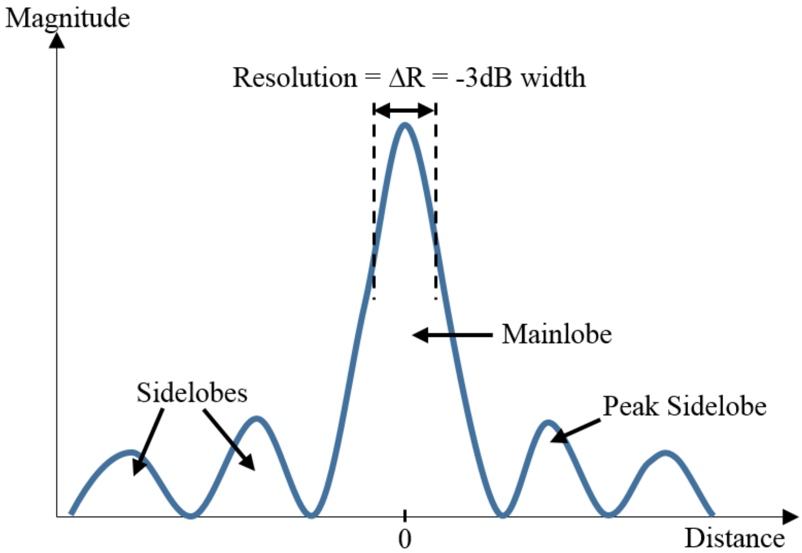

Figure 3.9: Autocorrelation function and lateral lobes

Since digital filtering is usually performed in modern radar systems, we use the discrete notation i.e. the sampled version of correlation function. For a given waveform sequence, the total energy in the sidelobes of its autocorrelation function is quantified by the integrated sidelobe level (ISL) metric which is defined as

$$\mathrm{ISL} = \sum_{\substack{k=-(N-1)\\k\neq 0}}^{N-1} |r(k)|^2 = 2\sum_{k=1}^{N-1} |r(k)|^2 \tag{3.25}$$

Another metric, which is called the merit factor (MF) is defined as follows

$$\mathrm{MF} = \frac{|r(0)|^2}{\sum\limits_{\substack{k=-(N-1)\\k\neq 0}}^{N-1} |r(k)|^2} = \frac{|r(0)|^2}{\mathrm{ISL}} \tag{3.26}$$

Since the goal of waveform design is to reduce the sidelobes, most computation algorithms involves the minimization of the ISL metric. This is also equivalent to the maximization of the MF defined in (3.26).

There exists weighted variants of ISL and MF metrics which are called Weighted

ISL (WISL) and Modified MF (MMF) respectively. Such weighted metrics are useful in situations when it is desirable to minimize interference from a known multipath or discrete clutter. These metrics are defined by

$$\text{WISL} = 2\sum_{k=1}^{N-1} w_k |r(k)|^2, \quad w_k \geq 0 \tag{3.27}$$

$$\text{MMF} = \frac{|r(0)|^2}{\text{WISL}} \tag{3.28}$$

Another widely used metric called Peak Sidelobe Level (PSL) which is defined as

$$\text{PSL} = \max_{k \neq 0} \left| \frac{r(k)}{r(0)} \right|^2 . \tag{3.29}$$

The ratio of the peak to the mean level of the sidelobes is referred as Peak-to-Sidelobe-Ratio (PSLR) that is given by

$$\text{PSLR} = \frac{|r(0)|^2}{\frac{1}{N-1}\sum_{k=1}^{N-1} |r(k)|^2} \tag{3.30}$$

3.5 Ambiguity Function

The response of a matched filter to a signal with different time delays and Doppler frequency shifts is measured by the Woodward's ambiguity function (AF) [72]. Assume that the transmit signal with the time support $[0, T]$ is $s(t)$. The ambiguity function of $s(t)$, is given as

$$\chi(\tau, f) = \int_{-\infty}^{\infty} s(t)s^*(t-\tau)e^{-j2\pi f(t-\tau)}dt \tag{3.31}$$

where f is the Doppler frequency shift and τ is the time delay. More precisely, (3.31) is the ambiguity function for narrowband signals which is commonly used in the analysis of signals that conforms to narrowband assumption. Typically, the radar signals having a bandwidth that is less than one-tenth of the carrier frequency, are regarded as narrowband signals [5]. A more elaborate discussion on AF is given in Appendix-A. We will utilize the ambiguity function to analyse the matched filter response of the waveforms in spatial and spectral domain.

Properties of narrowband AF can be summarized as follows.

- Symmetry Property: $|\chi(\tau, f))| = |\chi(-\tau, -f))|$
- Constant Volume: the volume of $|\chi(\tau, f))|^2$ is given by

$$V = \int_{-\infty}^{\infty} \int_{-\infty}^{\infty} |\chi(\tau, f))|^2 \mathrm{d}\tau\mathrm{df} = E^2 \tag{3.32}$$

  where E denotes the signal energy i.e., $E = \int_{-\infty}^{\infty} |s(t)|^2 \mathrm{dt}$

- Maximum at the origin : The maximum value of $|\chi(\tau, f))|$ is achieved by $|\chi(0, 0))|$ which is equal to the signal energy.

$$|\chi(0, 0))| = \int_{-\infty}^{\infty} s(t)s^*(t)\mathrm{dt} = E \tag{3.33}$$

An ideal thumbtack ambiguity function is shown in Figure 3.10. The width of spike in range axis defines the range resolution whereas the width of spike in Doppler axis defines the Doppler resolution. These resolutions are important for separating targets very close to each other and detecting moving targets at the same range cell with different velocities. This shows that as we increase the bandwidth B, we obtain better range resolution. Conversely, if we increase the pulse length T, we improve the Doppler resolution. Another important fact is that the autocorrelation function is simply the zero-Doppler cut of the ambiguity function for a given waveform.

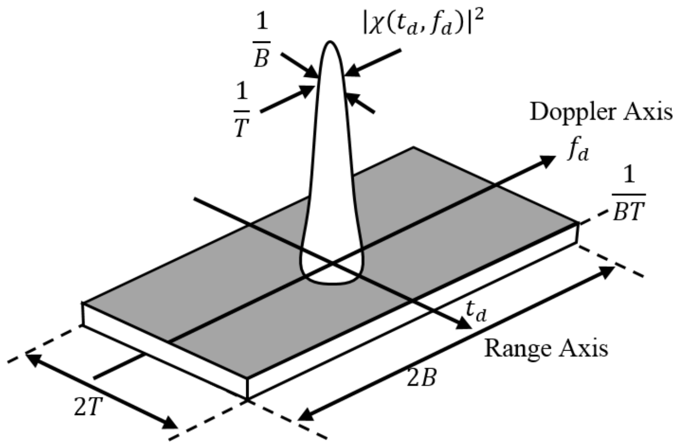

Figure 3.10: Ideal (thumbtack) ambiguity function

In Figure 3.11, the AF of a chirp signal with parameters $T = 10sec$ and $B = 1Hz$ is shown. It should be noted that a change in Doppler frequency shift due to the target velocity result a range offset after matched filtration. This AF has the Doppler-tolerance property i.e. a mismatch in Doppler frequency can still produce a detection peak at a cost of degradation in peak level. This Doppler-range coupling can be resolved by having a bank of filters matched to different Doppler frequency shifts.

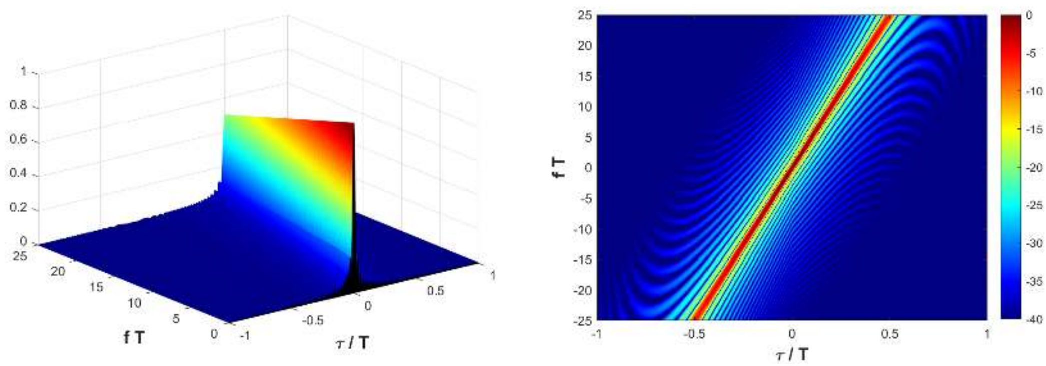

(a) (b)

Figure 3.11: Ambiguity function of a LFM signal: (a) 3D plot, (b) 2D plot.

In Figure 3.12, it can be seen that the ambiguity function of a noise waveform is thumbtack shaped which leads to high resolution both in range and Doppler. This kind of waveform is termed as Doppler-sensitive waveform.

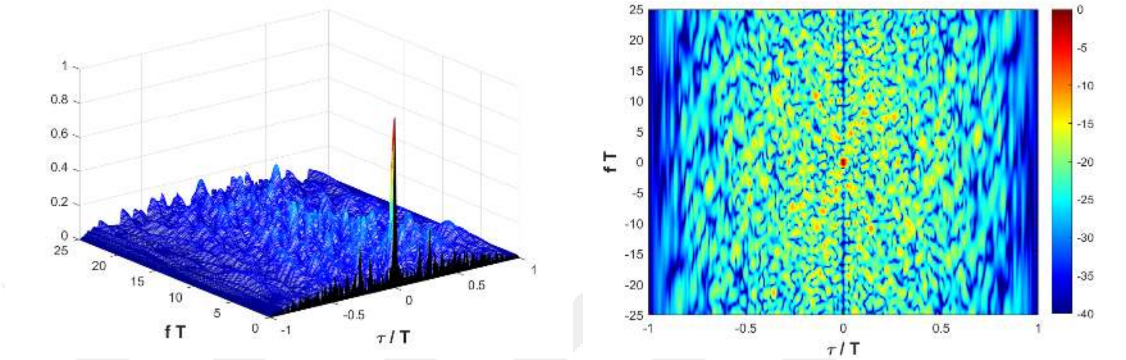

(a) (b)

Figure 3.12: Ambiguity function of a noise radar waveform: (a) 3D plot, (b) 2D plot.

3.6 Summary

We introduced the reader to the transmit waveform model, its processing by the optimal receive filter, i.e., the matched filter, as well as the autocorrelation function and the ambiguity function. We have compared the matched filter with inverse and Wiener filter, and demonstrated the optimality of matched filter along with drawback of other filtering methods. The chapter also establishes the foundation for understanding the waveform design principles used in the rest of the thesis. Autocorrelation and the Ambiguity function are shown to have significant uses in gaining insight into particular waveform properties such as range and Doppler resolution. Quality metrics are provided for assessing radar waveforms; these metrics are frequently incorporated into problem formulations for waveform optimization.

Chapter 4

EXISTING METHODS AND WAVEFORM DESIGN TECHNIQUES

Having presented the literature review on waveform design in Section 1.2, in this chapter, we narrow down our scope into the seminal methods proposed in the literature, including the classical waveforms and contemporary synthesis algorithms. We begin with the conventional radar waveforms, which have been used widely in legacy radar systems, and then we address the contemporary computation algorithms, primarily optimizing the correlation-related metrics introduced in Section 3.4.

4.1 Conventional Methods - Classical Radar Waveforms

In this section, we review several well-known waveforms that have good autocorrelation properties, especially phase-coded ones. We will provide an overview of these popular algebraic methods in the literature. These classical waveform synthesis methods include closed-form algebraic formulations, which does not include any optimization parameter. Their autocorrelation function has a deterministic envelope and sidelobe characteristics by definition. In the following, we refer to signals' aperiodic correlation function unless we explicitly state the periodic correlation function.

4.1.1 LFM Waveform (Chirp Signal)

The chirp waveform is a well-known radar signal. This is a pulse that has its frequency linearly swept over a specific bandwidth B over the course of a certain amount of time T. This type of pulse is referred to as linear frequency modulation (LFM) signal. As a result of their low correlation sidelobes at long range and their tolerance to Doppler frequency shifts, chirp signals have been widely utilized in conventional radar systems since World War II [5]. In addition, a chirp signal's power is spread out evenly over the frequency spectrum, resulting in excellent spectral efficiency.

A complex LFM signal $s(t)$ can be defined as

$$LFM \quad s(t) = \frac{1}{\sqrt{T}} e^{j\pi \frac{B}{T} t^2}, \quad 0 \leq t \leq T \tag{4.1}$$

where B/T denotes the sweep (chirp) rate. As an example, in Figure 4.1, a real part of a chirp signal with parameters $B = 1$ Hz and $T = 100$ sec, and its autocorrelation function $r(\tau)$ are illustrated.

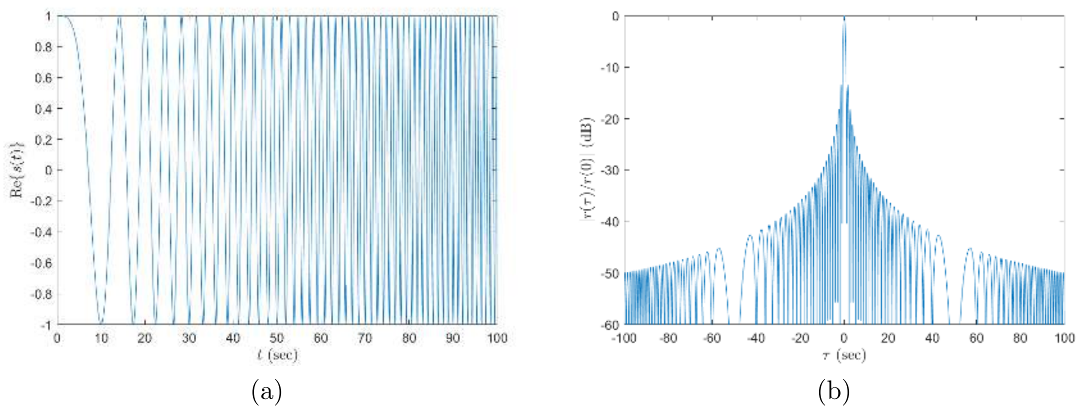

Figure 4.1: LFM signal $B = 1$ Hz, $T = 100$s and its autocorrelation: (a) Real part of the signal, (b) ACF.

4.1.2 Golomb Sequence

A Golomb sequence is another signal known to have perfect periodic correlations for odd N [20]. The Golomb signal can be defined by

$$x(n) = e^{j\pi \frac{n(n-1)}{N}}, \quad n = 1, ..., N \tag{4.2}$$

An exemplary Golomb signal of length $N = 127$ is shown in Figure 4.2.

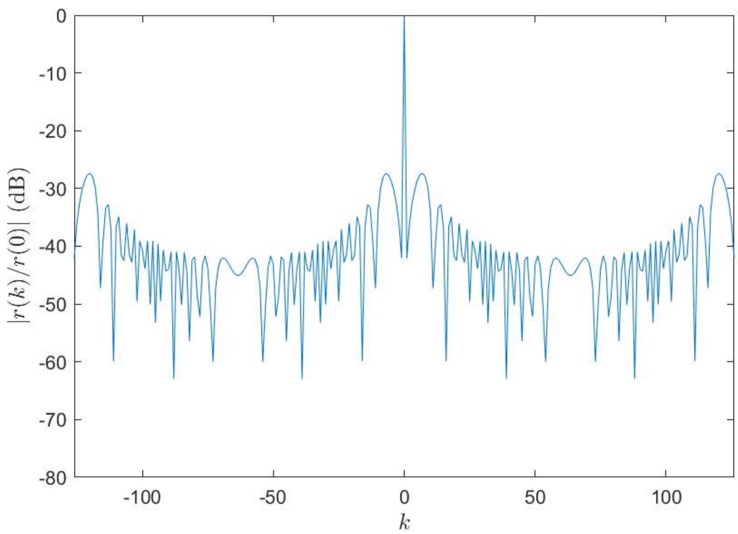

Figure 4.2: Autocorrelation of Golomb sequence, $N = 127$

4.1.3 Chu Sequence

A variant of the Golomb sequence, the Chu sequence [17] is formulated as follows

$$x(n) = \begin{cases} e^{jL\pi\frac{n^2}{N}}, & N \ even, \\ e^{jL\pi\frac{n(n-1)}{N}}, & N \ odd, \end{cases} \tag{4.3}$$

where L is any integer number that is prime to the sequence length N. This sequence has good periodic correlations for any choice of N.

4.1.4 Frank Sequence

Other than Golomb and Chu sequences, there are alternative phase-coded sequences with good periodic correlations, whose phases are quadratic functions of n, i.e., the Frank sequence and the P4 sequence. Frank sequence is defined for $N = Q^2$ as

$$x((m-1)Q+p) = e^{j2\pi\frac{(m-1)(p-1)}{Q}}, \quad m, p = 1, ..., Q \tag{4.4}$$

4.1.5 P4 Sequence

For any N, the P4 sequence is described as

$$x(n) = e^{j\frac{2\pi}{N}(n-1)(\frac{n-1-N}{2})}, \quad n = 1, ..., N \tag{4.5}$$

A P4 sequence of length $N = 100$ is shown in Figure 4.3.

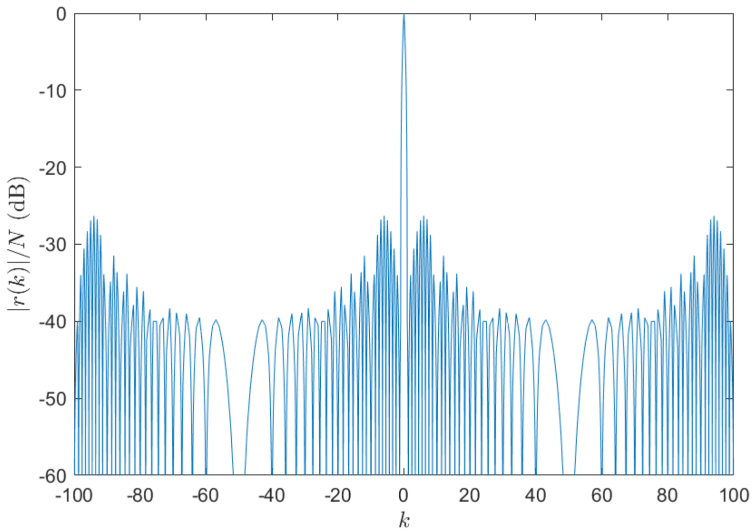

Figure 4.3: Autocorrelation of P4 sequence, $N = 100$

4.1.6 Maximum Length Sequence

Another widely used sequence is the m-sequence (maximum length sequence) which is the commonly known pseudo-noise sequence generated by a maximal linear shift register(LFSR). M-sequences have a distinct property that its periodic correlation sidelobes are always equal to -1. An example m-sequence of length $N = 127$ is depicted in Figure 4.4.

4.1.7 Barker Sequence

Barker code is another sequence widely used as radar transmit signals [15]. It was defined as binary sequence with correlation sidelobes not greater than 1. However

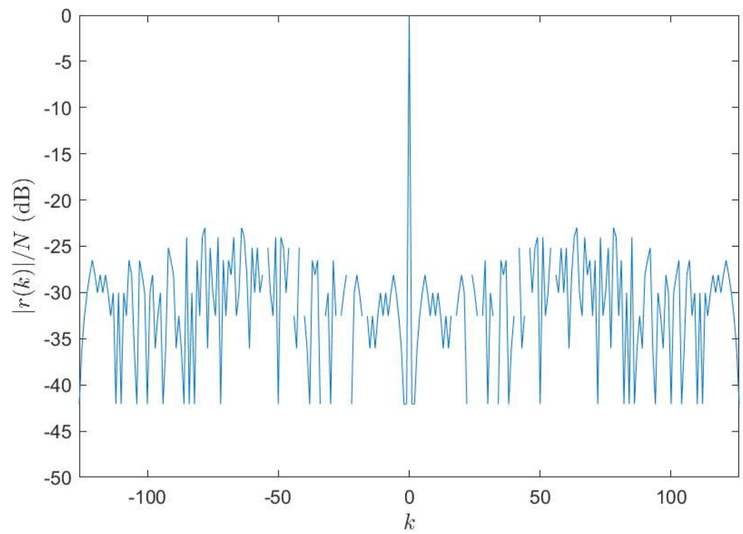

Figure 4.4: Autocorrelation of m-sequence, $N = 127$

the longest Barker code has length 13 and it is given as

$$\{x(n)\} = \{1, 1, 1, 1, 1, -1, -1, 1, 1, -1, 1, -1, 1\} \tag{4.6}$$

The classical sequences and waveforms mentioned above have closed-form construction methods. To find sequences with less autocorrelation sidelobes, researchers have also employed stochastic optimization and gradient descent approaches. [84–86]. Unfortunately, these methods are typically computationally costly and only perform adequately for very modest values of N ($N \sim 100$). For example in [85], a longer (length-45) polyphase Barker whose auto-correlation sidelobes are less than or equal to 1 is proposed. This polyphase Barker code is defined as

$$x(n) = e^{j\theta(n)}, \ \ n = 1, ..., 45 \tag{4.7}$$

where

$$\{\theta(n)\} = \frac{2\pi}{90}\{0\ 0\ 7\ 1\ 76\ 71\ 76\ 63\ 56\ 73\ 87\ 9\ 9\ 14\ 25\ 53\ 62\ 5\ 32\ 35\ 85\ 69\ 40\ 76\ 57\ 26\ 9\ 83$$
$$56\ 57\ 21\ 5\ 52\ 89\ 48\ 11\ 68\ 26\ 62\ 6\ 37\ 73\ 19\ 58\ 12\} \tag{4.8}$$

and its auto-correlation is demonstrated in Figure 4.5. It should be noted that that the lowest possible peak sidelobe is 1 for a unimodular sequence, since the last autocorrelation sample is $|r(N-1) = |x(1)x^*(N)| = 1$. When N=45, the PSL attains the value of $20log_{10}(1/N) = -33.1dB$ which is the case for the length-45 polyphase Barker code as shown in Figure 4.5.

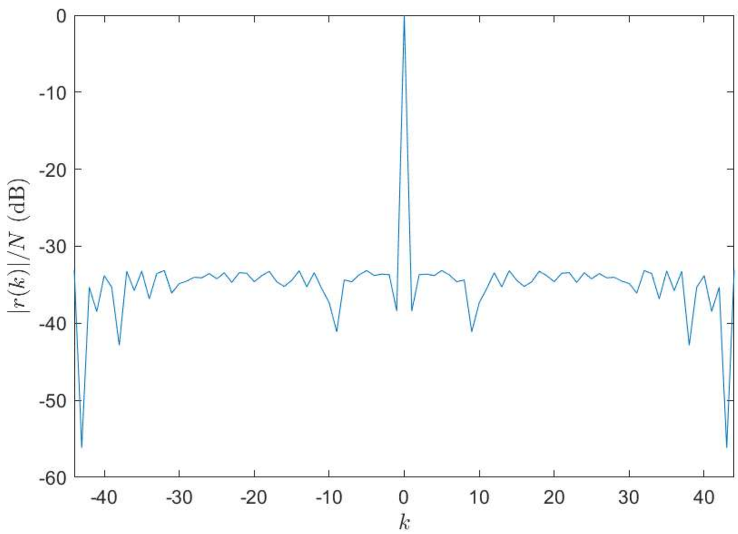

Figure 4.5: Autocorrelation of Barker sequence, $N = 45$

Up to this point, we have reviewed several classical sequences and waveforms widely used in conventional radar systems. These sequences have very low periodic or aperiodic correlation sidelobes and there are many others possessing good correlation properties, such as Kasami sequences, Gold sequences [87] in the literature. However, for some applications such as automotive radar or marine radar, the sequences built using algebraic approaches might be limiting by a lack of diversity and a lack of length flexibility due to various construction conditions.

4.2 Computational Methods - Waveform Synthesis Algorithms

In this section, we will introduce the important computational methods and optimization techniques utilized for waveform design problems in the literature. Although there exists algorithms optimizing various metrics (i.e., Ambiguity function [40], binary constraint [39],Peak Sidelobe Level (PSL) [27,43,44], Peak to Average Power Ratio constraint [42] and similarity [41]) in the literature, we concentrate down on ISL and Spectral Stopband energy minimization algorithms in our work.

Let $\mathbf{x} = \{x_n\}_{n=0}^{N-1}$ denote the unimodular sequence of length N to be designed. The m^{th} sample of a sequence is denoted as $e^{j\theta(m)}$, where $\theta(m)$ is an arbitrary phase that is distributed in $[0, 2\pi]$. The aperiodic auto-correlation function of a sequence $\mathbf{x}$ at any delay index k can be given as:

$$r(k) = \sum_{n=k}^{N-1} x(n)x^*(n-k) = r^*(-k), \quad k = 0, ..., N-1. \tag{4.9}$$

Then, the problem to design unimodular sequences that minimizes the ISL metric can be formulated as follows

$$\begin{aligned} \min_{\mathbf{x}} \quad & \text{ISL} = 2\sum_{k=1}^{N-1} |r(k)|^2 \\ \text{subject to} \quad & |x_n| = 1, \quad n = 0, ..., N-1. \end{aligned} \tag{4.10}$$

The existing algorithms which are developed based on solving the ISL minimization problem in (4.10) are CAN [24], MISL [25], ISL-NEW, ADMM [34], MWISL [27], CPM, FCGA [37], FISL [31], SMISLN [38]. In the following we will highlight the important approaches and explain their construction method.

4.2.1 The Cyclic Algorithm-New (CAN) Algorithm

The CAN algorithm, proposed by Stoica et al. [24], is based on the alternating-minimization method. By converting the objective function given by (4.10) to the frequency domain, they were able to find an alternate solution.

$$\sum_{k=1}^{N-1} |r(k)|^2 = \frac{1}{4N} \sum_{p=1}^{2N} \left(\left| \sum_{n=1}^{N} x_n e^{-j\omega_p n} \right|^2 - N \right)^2 \tag{4.11}$$

where $\omega_p = \frac{2\pi}{2N} p,\ p = 1, ..., 2N$ are the Fourier frequencies. Then the problem in (4.10) is transformed into:

$$\begin{aligned} \min_{\mathbf{x}} \quad & \frac{1}{4N} \sum_{p=1}^{2N} \left(\left| \sum_{n=1}^{N} x_n e^{-j\omega_p n} \right|^2 - N \right)^2 \\ \text{subject to} \quad & |x_n| = 1, \quad n = 0, ..., N-1. \end{aligned} \tag{4.12}$$

The objective function of the problem in (4.12) is quartic in $\mathbf{x}$ and it is difficult to solve further. So, they solved an approximate problem that is quadratic in $\mathbf{x}$ instead of solving the quartic (4.12) directly. The approximate problem is as shown below:

$$\begin{aligned} \min_{\mathbf{x}, \psi_p} \quad & \sum_{n=1}^{2N} \left| \sum_{p=1}^{N} x_n e^{-j\omega_p n} - \sqrt{N} e^{j\psi_p} \right|^2 \\ \text{subject to} \quad & |x_n| = 1, \quad n = 1, ..., N. \end{aligned} \tag{4.13}$$

where ψ_p, $p = 1, 2, ..., 2N$ denote the auxiliary phases. The resulting problem can be formulated more concisely as follows:

$$\begin{aligned} \min_{\mathbf{x}, \mathbf{y}} \quad & \left\| \mathbf{E}^H \hat{\mathbf{x}} - \sqrt{N} \mathbf{y} \right\|^2 \\ \text{subject to} \quad & |x_n| = 1, \quad n = 1, ..., N. \end{aligned} \tag{4.14}$$

where $\mathbf{E} = [\mathbf{e}_1, ..., \mathbf{e}_{2N}]$ be a $2N \times 2N$ matrix with $\mathbf{e}_p = \left[e^{j\omega_p(1)}, e^{j\omega_p(2)}, ..., e^{j\omega_p(2N)} \right]^T$, $\hat{\mathbf{x}} = [x_1, x_2, ..., x_{2N}, 0, ..., 0]^T_{1 \times 2N}$ and $\mathbf{y} = \left[e^{j\psi_1}, e^{j\psi_2}, ..., e^{j\psi_{2N})} \right]^T$. They solved the problem in (4.14) by alternatively minimizing between the variables $\mathbf{x}$ and $\mathbf{y}$. For a given $\mathbf{x}$, minimization of (4.14) with respect to $\mathbf{y}$ is given by:

$$\mathbf{y} = \frac{\mathbf{v}}{|\mathbf{v}|}, \tag{4.15}$$

where $\mathbf{v} = \mathbf{E}^H\hat{\mathbf{x}}$ ($\mathbf{E}^H$ is a FFT matrix of size $2N \times 2N$) and for a fixed $\mathbf{y}$ the minimizer over $\mathbf{x}$ would be:

$$\mathbf{x} = \frac{\mathbf{b}}{|\mathbf{b}|}, \tag{4.16}$$

where $\mathbf{b} = \mathbf{E}\hat{\mathbf{y}}$ ($\mathbf{E}$ is a IFFT matrix of size $2N \times 2N$). The pseudo code of the CAN algorithm is given in Algorithm 1.

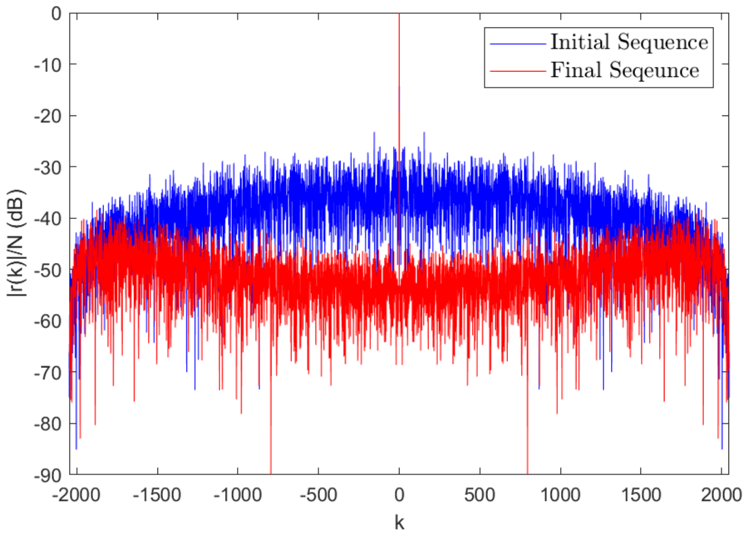

Figure 4.6: ACF of the CAN sequence, $N = 2048$

We would want to draw attention to the fact that the CAN algorithm, rather than solving problem in (4.10), has instead solved problem in (4.13), which is approximately equivalent to the problem in (4.10). Thus, there is no assurance that a minimum of (4.13) will also be a minimum in the original problem in (4.10).

Algorithm 1 The Cyclic Algorithm New (CAN) Algorithm [24]

Initialization: Set sequence length N, $k = 0$ and $\mathbf{x}^0$
Repeat
  $\mathbf{v} = \mathbf{E}^H \hat{\mathbf{x}}^k$
  $\mathbf{y} = \frac{\mathbf{v}}{|\mathbf{v}|}$
  $\mathbf{b} = \mathbf{E}^H \mathbf{y}$
  $\mathbf{x}^{k+1} = \frac{\mathbf{b}_{1:N}}{|\mathbf{b}_{1:N}|}$
  $k = \leftarrow k + 1$
Until convergence i.e., $\left\|\mathbf{x}^{k+1} - \mathbf{x}^k\right\| \leq \epsilon$

An example output of the CAN algorithm for random initialization of sequence length $N = 2048$ is illustrated in Figure 4.6.

4.2.2 Majorization-Minimization (MM) Framework

In the last decade, a number of waveform design methods such as MISL [25], FISL [31], SMISLN [38] have been developed based upon the Majorization-Minimization framework. Therefore, in this section we first introduce the reader to the general concepts of MM framework and then we describe the procedure for MM based algorithms in the ensuing sections.

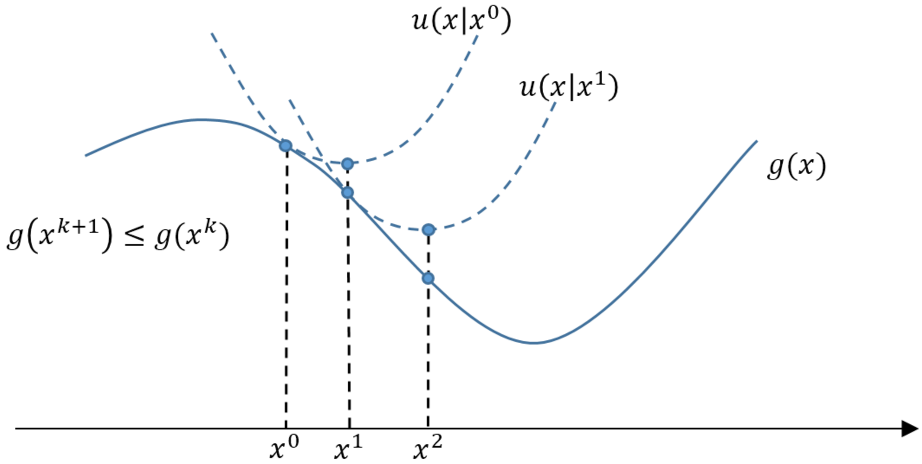

Figure 4.7: Majorization-Minimization procedure

Majorization-Minimization (MM) framework involves a two-step strategy, that is efficiently used to solve the hard (non-convex or even convex) problems [26,88]. The MM technique involves two steps: first, constructing a majorization (upper bound) function $u()$ to the original objective function $g()$ at any point $\mathbf{x}^k$ ($\mathbf{x}$ at the k^{th} iteration), and second, minimizing the upper bound function $u()$ to produce a next update $\mathbf{x}^{k+1}$. Thus, at each newly produced point, the aforementioned two processes are repeated until the optimal minimum point of the original function $g()$ is reached. Majorization function can be built in a variety of ways for any given problem, and there will be different majorization functions for the same problem.Therefore, the performance will purely depend on the majorization function used; examples of the various methods for majorization function construction are provided in [88, 89].The majorization function $u(\mathbf{x}|\mathbf{x}^k)$, which is created in the first stage of the MM technique, must adhere to the following criteria:

$$u(\mathbf{x}|\mathbf{x}^k) = g(\mathbf{x}^k), \quad \forall \mathbf{x}^k \in \mathbf{X}. \tag{4.17}$$

$$u(\mathbf{x}|\mathbf{x}^k) \geq g(\mathbf{x}^k), \quad \forall \mathbf{x}^k \in \mathbf{X}. \tag{4.18}$$

where $\mathbf{X}$ denotes the set consists of all the possible values for $\mathbf{x}$. Since the MM technique involves an iterative procedure, it will generate new sequences $\{\mathbf{x}\} = \mathbf{x}^1, \mathbf{x}^2, \mathbf{x}^3, ..., \mathbf{x}^m$ successively based on the following update rule:

$$\mathbf{x}^{k+1} \triangleq \arg\min_{\mathbf{x}\in\mathbf{X}} u(\mathbf{x}|\mathbf{x}^k). \tag{4.19}$$

The objective function value computed at every iteration with the updated $\mathbf{x}^k$ generated by (4.19) will satisfy the descent property, i.e.

$$g(\mathbf{x}^{k+1}) \leq u(\mathbf{x}^{k+1}|\mathbf{x}^k) \leq u(\mathbf{x}^k|\mathbf{x}^k) = g(\mathbf{x}^k). \tag{4.20}$$

The overall procedure of the MM framework is illustrated in Figure 4.7.

4.2.3 Monotonic Minimizer For Integrated Sidelobe Level (MISL) Algorithm

By using the MM technique to directly solve the original problem in (4.10), Song et al. introduced the MISL algorithm [25] in 2015 to address the CAN algorithm's flaws. So, from (4.12) we have,

$$\begin{aligned} \min_{\mathbf{x}} \quad & \frac{1}{4N} \sum_{p=1}^{2N} \left(\left| \sum_{n=1}^{N} x_n e^{-j\omega_p n} \right|^2 - N \right)^2 \\ \text{subject to} \quad & |x_n| = 1, \quad n = 0, ..., N-1. \end{aligned} \tag{4.21}$$

The above problem may be recast in a more compact form by expanding the cost function and removing the constant and multiplication terms, yielding:

$$\begin{aligned} \min_{\mathbf{x}} \quad & \sum_{p=1}^{2N} \left(\mathbf{e}_p^H \mathbf{x}\mathbf{x}^H \mathbf{e}_p \right)^2 \\ \text{subject to} \quad & |x_n| = 1, \quad n = 0, ..., N-1. \end{aligned} \tag{4.22}$$

The problem in (4.22) is quartic in $\mathbf{x}$, and further solution is very difficult. Therefore, assuming $\mathbf{X} = \mathbf{x}\mathbf{x}^H$ and $\mathbf{C}_p = \mathbf{e}_p\mathbf{e}_p^H$, the problem in (4.22) can be recast as;

$$\begin{aligned} \min_{\mathbf{x},\mathbf{X}} \quad & \text{vec}(\mathbf{X})^H \Phi \text{vec}(\mathbf{X}) \\ \text{subject to} \quad & |x_n| = 1, \quad n = 0, ..., N-1. \\ & \mathbf{X} = \mathbf{x}\mathbf{x}^H \end{aligned} \tag{4.23}$$

where $\Phi = \sum_{p=1}^{2N} \text{vec}(\mathbf{C}_p)\text{vec}(\mathbf{C}_p)^H$. Then, the cost function in (4.23) becomes quadratic in $\mathbf{X}$. So, they constructed a majorization function for it by using a second-order Taylor series method [88, 89], and by neglecting the constant terms, the surrogate problem can be rewritten more compactly as:

As a result, they developed a majorization function for it using a second-order Taylor series approach [88, 89], and by excluding the constant terms, the surrogate issue may now be expressed more compactly as:

$$\begin{aligned} \min_{\mathbf{x}} \quad & \mathbf{x}^H \left(\mathbf{E}\,\mathrm{Diag}\,(\mathbf{b}^k)\mathbf{E}^H - 2N^2\mathbf{x}^k(\mathbf{x}^k)^H\right)\mathbf{x} \\ \text{subject to} \quad & |x_n| = 1, \quad n = 0, ..., N-1. \end{aligned} \tag{4.24}$$

where $\mathbf{b}^k = |\mathbf{E}^H\mathbf{x}^k|$. The resultant problem in (4.24) is quadratic in $\mathbf{x}$, and they have majorized the cost function in the above problem once again as mentioned above, to obtain a simple closed-form solution. After majorizing for the second time and by ignoring the constant terms, the final surrogate minimization problem becomes:

They have again majorized the cost function in the aforementioned problem to get a straightforward closed-form solution because the resulting problem in (4.24) is quadratic in $\mathbf{x}$. After majorizing twice and omitting the constant terms, the last surrogate minimization problem becomes: .

$$\begin{aligned} \min_{\mathbf{x}} \quad & \mathrm{Re}\left(\mathbf{x}^H\left(\tilde{\mathbf{C}} - 2N^2\mathbf{x}^k(\mathbf{x}^k)^H\right)\mathbf{x}^k\right) \\ \text{s.t.} \quad & |x_n| = 1, \quad n = 1, ..., N. \end{aligned} \tag{4.25}$$

where $\tilde{\mathbf{C}} = \mathbf{E}\left(\mathrm{Diag}(\mathbf{b}^{2k}) - b^k_{max}\mathbf{I}\right)\mathbf{E}^H$ and $b^k_{\max} = \max_p (b^k_p)^2,\ p = 1, 2, ..., 2N$. Problem in (4.25) can be expressed more succinctly as:

$$\begin{aligned} \min_{\mathbf{x}} \quad & \|\mathbf{x} - \mathbf{d}\|_2^2 \\ \text{s.t.} \quad & |x_n| = 1, \quad n = 1, ..., N. \end{aligned} \tag{4.26}$$

where $\mathbf{d} = -\mathbf{E}\left(\mathrm{Diag}(\mathbf{b}^{2k}) - b^k_{max}\mathbf{I} - N^2\mathbf{I}\right)\mathbf{E}^H\mathbf{x}^k$. Finally, the problem in (4.26) leads to a closed-form solution:

$$\mathbf{x} = \frac{\mathbf{d}}{|\mathbf{d}|}, \tag{4.27}$$

The pseudocode of the MISL algorithm is summarized in Algorithm 2

Algorithm 2 The Monotonic Minimizer For Integrated Sidelobe Level (MISL) Algorithm [25]

Initialization: Set sequence length N, $k = 0$ and $\mathbf{x}^0$
Repeat
    $\mathbf{b}^k = |\mathbf{E}^H \mathbf{x}^k|$
    $b^k_{max} = \max_a \{(b^k_a)^2, \quad a = 1, ..., 2N\}$
    $\mathbf{b} = \mathbf{E}^H \mathbf{y}$
    $\mathbf{z}^{k+1} = \frac{\mathbf{b}_{1:N}}{|\mathbf{b}_{1:N}|}$
    $k = \leftarrow k + 1$
Until convergence i.e., $\left\|\mathbf{x}^{k+1} - \mathbf{x}^k\right\| \leq \epsilon$

In contrast to the CAN method, the MISL algorithm solves the original problem in (4.10). This ensures that the original optimal minimum point will be found in the first place. However, because the original objective function has been majorized twice, the MISL method suffers from slow convergence. To address the issue of slow convergence, they devised acceleration strategies to speed up the MISL algorithm.

4.2.4 Sparse Frequency Waveform Design

In some cases, it is desirable to have low spectral power in specified frequency bands. Besides frequency notching, the good correlation properties should be preserved for the designed sequence. The minimization problem which incorporates both spectral and correlation sidelobe constraints can be formulated as

$$\begin{aligned} \min_{\mathbf{x}} \quad & J = \lambda J_{\text{STOP}} + (1-\lambda)\, J_{\text{ISL}} \\ \text{subject to} \quad & |x_n| = 1, \quad n = 0, ..., N-1. \end{aligned} \tag{4.28}$$

where $\lambda \in [0, 1]$ is a weight parameter to trade off between the spectral stopband and ISL costs.

For the solution of the problem in (4.28), the cyclic Stopband CAN (SCAN) [13] algorithm is proposed. In [13], instead of solving the original problem they solve a quadratic approximation of the ISL. The SCAN algorithm is a variation of the CAN algorithm mentioned above. Later on, MM based algortihms such as Spectral MISL [25] and SMISLN [38] algorithms are proposed. Another method named "Fast Conjugate Gradient algorithm (FCGA)" using a nonlinear conjugate gradient algorithm is proposed in [37].

4.2.5 Stopband CAN (SCAN) Algorithm

As an extension of the CAN algorithm, SCAN was proposed in [13] for incorporating the additional spectral stopband constraint in addition to the minimization of the ISL constraint already involved in the CAN algorithm. The frequency stopbands of the unimodular sequence, $\{x_n\}_{n=1}^{N}$, can be defined as $\Omega = \bigcup_{i=1}^{N_s} (f_{\mathrm{a}_i}, f_{\mathrm{b}_i})$ where $(f_{\mathrm{a}_i}, f_{\mathrm{b}_i})$ and N_s denotes the stopband border frequencies and the number of stopbands, respectively. If the number of discrete Fourier transform (DFT) bins is denoted by $\tilde{N}$ which is chosen preferably large enough to densely cover the frequency stopbands Ω, the $(k+1, l+1)$th element of the $\tilde{N} \times \tilde{N}$ unitary DFT matrix, $\mathbf{F}_{\tilde{N}}^H$, is expressed as

$$[\mathbf{F}_{\tilde{N}}^H]_{k+1,l+1} = \frac{1}{\sqrt{\tilde{N}}} \exp\left(-j\frac{2\pi kl}{\tilde{N}}\right) \tag{4.29}$$

where $k, l = 0, ..., \tilde{N}-1$ and the constant term, $\frac{1}{\sqrt{\tilde{N}}}$, assures that the matrix $\mathbf{F}_{\tilde{N}}$ is unitary. Next, a matrix $\mathbf{S}$ is constructed from the columns of $\mathbf{F}_{\tilde{N}}$ corresponding to the frequency bins in the stopbands, Ω. Then, the following term can be minimized in order to suppress the stopband frequencies

$$\left\| \mathbf{S}^H \begin{bmatrix} \mathbf{x} \\ \mathbf{0}_{(\tilde{N}-N)\times 1} \end{bmatrix} \right\|^2 \tag{4.30}$$

where $\|\cdot\|^2$ denotes the squared norm of a vector and $\mathbf{0}_{(\tilde{N}-N)\times 1}$ denotes $\mathbf{0}_{(\tilde{N}-N)\times 1} = \begin{bmatrix} \underbrace{0 \; ... \; 0}_{\tilde{N}-N} \end{bmatrix}^T$. Defining $\hat{\mathbf{x}} = \begin{bmatrix} \mathbf{x} \\ \mathbf{0}_{(\tilde{N}-N)\times 1} \end{bmatrix}$ and denoting the null space of $\mathbf{S}^H$ by $\mathbf{G}$, the minimization of the term in (4.30) can be formulated equivalently as [13]

$$\begin{aligned} \min_{\mathbf{x},\boldsymbol{\alpha}} \quad & J_{STOP}(\mathbf{x},\boldsymbol{\alpha}) = \|\hat{\mathbf{x}} - \mathbf{G}\boldsymbol{\alpha}\|^2 \\ \text{subject to} \quad & |x_n| = 1, \quad n = 1, ..., N. \end{aligned} \tag{4.31}$$

where $\boldsymbol{\alpha}$ is an auxiliary vector of variables and $J_{STOP}(\mathbf{x},\boldsymbol{\alpha})$ constitutes the first part of the cost function in (4.28).

In order to work out the ISL part (J_{ISL}) of the cost function in (4.28), first, ISL is expressed in the frequency domain as [24]

$$\begin{aligned} ISL &= \frac{1}{4N}\sum_{p=1}^{2N}\left[|\sqrt{2N}\mathbf{a}_p^H\bar{\mathbf{x}}|^2 - N\right]^2 \\ &= N\sum_{p=1}^{2N}\left[|\mathbf{a}_p^H\bar{\mathbf{x}}|^2 - \frac{1}{2}\right]^2 \end{aligned} \tag{4.32}$$

where $\bar{\mathbf{x}} = \begin{bmatrix} \mathbf{x} \\ \mathbf{0}_{(N\times 1)} \end{bmatrix}$, $\mathbf{a}_p = \left[1, e^{j\omega_p}, ..., e^{j\omega_p(2N-1)}\right]^T$, $\omega_p = \frac{2\pi}{2N}(p-1)$, for $p = 1, ..., 2N$. The ISL metric above can be further simplified as $N\left\||\mathbf{F}_{2N}^H\bar{\mathbf{x}}|^2 - \frac{1}{2}\right\|^2$ which is a quartic function of x. Because the quartic function of x is difficult to solve further [24] proposes minimizing a quadratic approximation of the exact ISL metric. The "almost equivalent" approximation of the ISL metric is given in [24] as $N\left\|\mathbf{F}_{2N}^H\bar{\mathbf{x}} - \mathbf{v}\right\|^2$ where v is an auxiliary vector of variables defined as $\mathbf{v}_p = \frac{1}{\sqrt{2}}\left[e^{\psi_1}, ..., e^{\psi_{2N}}\right]^T$. Then, by utilizing this quadratic approximation of ISL, the cost function, $J_{ISL}(\mathbf{x},\mathbf{v})$, representing the second part (corresponding to J_{ISL}) of the cost function in (4.28), can be formulated as [13]

$$\begin{aligned} \min_{\mathbf{x},\mathbf{v}} \quad & J_{ISL}(\mathbf{x},\mathbf{v}) = \left\|\mathbf{F}_{2N}^H\bar{\mathbf{x}} - \mathbf{v}\right\|^2 \\ \text{subject to} \quad & |x_n| = 1, \quad n = 1, ..., N. \\ & |v_n| = \frac{1}{\sqrt{2}}, \quad n = 1, ..., 2N. \end{aligned} \tag{4.33}$$

Merging the spectral stopband and the ISL constraints, the following optimization problem is posed in [13]

$$
\begin{aligned}
\min_{\mathbf{x},\boldsymbol{\alpha},\mathbf{v}} \quad & J(\mathbf{x},\boldsymbol{\alpha},\mathbf{v}) = \lambda J_{STOP}(\mathbf{x},\boldsymbol{\alpha}) + (1-\lambda) J_{ISL}(\mathbf{x},\mathbf{v}) \\
& = \lambda \left\|\hat{\mathbf{x}} - \mathbf{G}\boldsymbol{\alpha}\right\|^2 + \ (1-\lambda) N \left\|\mathbf{F}_{2N}^H \bar{\mathbf{x}} - \mathbf{v}\right\|^2 \\
\text{subject to} \quad & |x_n| = 1, \quad n = 1, ..., N. \\
& |v_n| = \frac{1}{\sqrt{2}}, \quad n = 1, ..., 2N.
\end{aligned}
\tag{4.34}
$$

where $\lambda \in [0,1]$ is the relative weight parameter that is used to compromise between the two cost functions, $J_{STOP}(\mathbf{x},\boldsymbol{\alpha})$ and $J_{STOP}(\mathbf{x},\mathbf{v})$. The SCAN algorithm solves the above optimization problem by minimizing $J(\mathbf{x},\boldsymbol{\alpha},\mathbf{v})$ alternatively with respect to only one variable (either $\mathbf{x},\boldsymbol{\alpha},\mathbf{v}$)) at a time. An exemplary sequence generated with SCAN algorithm is shown in Figure 4.8.

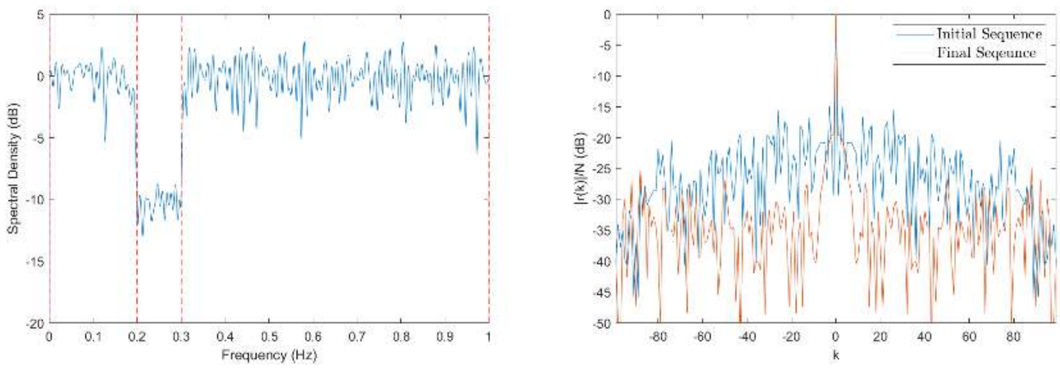

(a) (b)

Figure 4.8: SCAN algorithm output spectrum and ACF $\lambda = 0.7, \Omega = [0.2, 0.3], N = 100, \tilde{N} = 1000$: (a) Final sequence spectrum, (b) ACF.

4.2.6 FFT based Conjugate Gradient Algorithm (FCGA)

FFT based Conjugate Gradient method is proposed for the aperiodic/periodic/stopband sequence design by Tang et.al. [37]. The algorithm involves the computation of the gradient and and the step size in every iteration which relies on efficient FFT computation. Since they target at generating phase only signals (The samples of signal are complex exponentials), the step size is indeed the phase step added to the phase term of the samples in every iteration.

Based on this idea they devised an efficient method to obtain an approximate step size based on Taylor series expansion of the exponential term. In order to determine the search direction, they utilized the conjugate gradient method . As a result, the FCGA offered great speed improvement in comparison to the existing methods. The short algorithm definition is summarized in Algorithm 3. For in depth analysis, the reader may refer to [37].

Algorithm 3 FFT based Conjugate Gradient Algorithm (FCGA) [37]

1: **Initialization:** Set $k = 0$,λ,$\mathbf{w}_f$,N,$\tilde{N}$,$\mathbf{x}^0$,$\mathbf{f}^0 = \mathcal{F}_{\tilde{N}}(\mathbf{x}^0)$,$\mathbf{g}^0 = \nabla J_T(\mathbf{x}^0)$, $\mathbf{d}^0 = -\mathbf{g}^0$.

2: **Repeat**

3: $\quad \mathbf{f}_1^k = \mathcal{F}_{\tilde{N}}\left(\mathbf{x}^k \circ \mathbf{d}^k\right)$, $\mathbf{f}_2^k = \mathcal{F}_{\tilde{N}}\left(\mathbf{x}^k \circ \mathbf{d}^k \circ \mathbf{d}^k\right)$, $\mathbf{t}_2 = Im\left(\left(\mathbf{f}^k\right)^* \circ \mathbf{f}_1^k\right)$

4: $\quad$ compute the coefficients a, b, c, d according to [37](42).

5: $\quad$ solving the cubic equation [37](43), and then choose the positive root which is closest to zero as the step size μ^k

6: $\quad \mathbf{x}^{k+1} = \mathbf{x}^k \circ e^{j\mu^k \mathbf{d}^k}$, $\mathbf{f}^{k+1} = \mathcal{F}_{\tilde{N}}\left(\mathbf{x}^{k+1}\right)$

7: $\quad \mathbf{y} = \mathcal{F}_{\tilde{N}}^{-1}\left(\mathbf{w} \circ \left|\mathbf{f}^{k+1}\right|^2 \circ \mathbf{f}^{k+1}\right)$

8: $\quad \mathbf{g}^{k+1} = 4\tilde{N} Re\left(-j\left(\mathbf{x}^{k+1}\right)^* \circ \mathbf{y}_{1:N}\right)$

9: $\quad$ Compute the searching direction $\mathbf{d}^{k+1}$ according to [37](43)

10: $\quad k = \leftarrow k + 1$

11: **Until** convergence i.e., $\left\|\mathbf{x}^{k+1} - \mathbf{x}^k\right\| \leq \epsilon$

4.3 Summary

In this section, we have addressed the algorithm definition of the important waveform synthesis algorithms and their procedure. They rely on alternating minimization, majorization-minimization framework, and gradient-based approaches. The summary of the related literature can be given as follows: The CAN algorithm and its variants such as the SCAN, WeCAN have solved an approximate problem rather than the original problem. Thus there is no guarantee that these algorithms will converge to the global minimum of the original problem. On the other hand, the family of CAN algorithms which are based on alternating projection, are slow. The

MM based algorithms such as the MISL and its variants, the Spectral MISL, the MISL-NEW, the FISL and the SMISLN employ different types of majorization functions. Although they attempt to solve the original problem, their drawback is the double majorization of the original objective function. In contrast to CAN family, the MM based algorithms tend to converge faster. The ADMM method solves the approximate problem as the CAN does. Thus, they are not quite efficient. The CPM method is derived based on coordinate descent method, however, it suffers from computational complexity, particularly for large values of sequence length N.

Chapter 5

DESIGN OF LOW-PAPR WAVEFORMS FOR ENHANCED LOW PROBABILITY OF INTERCEPT NOISE RADARS

Noise radars utilizes random noise waveforms, as opposed to conventional radars. As advanced Low Probability of Intercept (LPI) radars, they are resistant to interference and jamming and less susceptible to adversarial exploitation than conventional radars. Using a random waveform as a probing signal, such as bandpass Gaussian noise, results in limited radar performance. In this chapter we discuss the need for synthesized (tailored) noise waveforms and propose the *Combined Spectral Shaping and Peak-to-Average Power Reduction (COSPAR)* algorithm for synthesizing noise-like sequences with a Taylor-shaped spectrum under correlation sidelobe level constraints and an assigned Peak-to-Average-Power-Ratio (PAPR). In addition, the Spectral Kurtosis measure is proposed for evaluating the LPI property of waveforms, and field trial results are reported.

The randomness of waveforms provides numerous benefits to both the civil and military radar applications. Noise radars are utilized in civilian applications such as automotive radar and marine navigation to reduce the risk of mutual interference brought on by a high number of radars operating in the same region and using the same frequency spectrum [70]. In case of military applications, noise radar has good Electronic Protection (EP) attributes and is robust to adversary Electronic Attacks (EA), like jammers, and can operate with a Low Probability of Interception (LPI) feature against Electronic Support Measure (ESM) or early warning receivers because of the random and unpredictable nature of its signals [90].

In the late 19th and early 20th centuries, random (analog) signals were used to identify objects. In 1897, Alexandr S. Popov employed random pulses in his radio experiments and stated that ship detection was achievable in a bistatic arrangement [91]. In 1904, Christian Huelsmeyer used the noise pulses of a spark generator in his Telemobiloscope, popularly known as the "radar precursor" [58, 59]. However, the technology was undeveloped at the time, and the sensing of objects relied on a simple radio detector (called a "coherer") instead of the coherent reception and correlation of signals. In 1957, R. Bourret made pioneering research on the coherent reception of random impulses [63]. His paper is regarded as the first to utilize noise signals in a coherent radar system. In 1959, B. M. Horton presented in detail the technique of measuring the distance of an object using random noise signals [64].

Much of the earliest work utilized physical delay lines to match the delay of the reference signal to the object's range, and as a result, could only provide limited range. However, due to the fact that intercept receivers can only capture noise from the transmitting radar, this technique has long been of interest. In addition, the nonrepetitive characteristics of transmissions would eliminate Doppler and range ambiguities in radar processing. However, due to technological challenges and a lack of noise-generating equipment, radar engineers at the time were unable to fully implement the noise radar concept. With the development of microwave and digital electronics in the late 20th century, there was a significant shift from analog to digital, and it became possible to synthesize random signals and do correlation processing entirely digitally. There has been great interest in noise radar technology over the past three decades, and remarkable progress has been made by research communities [52, 54, 92].

Physically generated by an analog source or digitally by a pseudo random noise generator, random signals are realizations of a random process. Once a realization of this random process is used as the modulating code, the radar is able to detect the presence of the broadcast signal by matched filtering. According to the principle of matched filter, noise radars can have comparable range and Doppler resolution to conventional radars, i.e. range resolution is dependent on signal bandwidth and Doppler resolution is dependent on coherent integration time. Low-power, high-duty-cycle noise waveforms can satisfy stealth criteria for covert missions, which has served as an additional incentive for researchers.

Noise radars provide numerous benefits over conventional radars [62]. The distinguishing characteristics of noise radars are as follows:

(i) Due to the randomness and unpredictability of noise signals, it is impractical for an adversary to intercept and exploit the transmitted signal.

(ii) Due to the (quasi) orthogonality of signals, mutual interference across radars sharing the same spectral band is reduced.

(iii) The signal's thumbtack-shaped Ambiguity Function enables for great resolution in both range and Doppler space.

Despite these benefits, noise radar is computationally intensive since it requires a large bandwidth for processing wideband noise waveforms on return and fast digitizers to offer a sufficient sample rate in comparison to conventional FMCW radars. Depending on the application, noise radars can operate either in pulsed or continuous wave (CW) mode. Due to the absence of edge modulations, however, the LPI features of the noise signal are best matched by CW emissions. Regardless of the emission regime chosen, the transmit waveform has a substantial impact on the radar's performance. Using a random waveform, such as a bandpass Gaussian noise (zero mean and unit variance), limits the dynamic range (as discussed in Section 5.3), namely leads to low sensitivity, and reduces detection performance. Therefore, noise radars necessitate optimized (tailored) synthetic waveforms to provide acceptable resolution, dynamic range, and detection capability.

The purpose of chapter is to introduce the reader to a new type of waveform that can strengthen LPI features and ensure orthogonality while enhancing the radar dynamic range. The remaining sections of this chapter are structured as follows. First, we introduce the reader to the continuous noise radar architecture of interest and the implementation of its associated correlation processing. In the next sections, we discuss the dynamic range issue, correlation sidelobes and leakage effects, as well as Peak-to-Average-Power-Ratio (PAPR) issues. We then give a clear justification for the use of customized noise waveforms. Next, we explain the procedure for the proposed Combined Spectral Shaping and Peak-to-Average Power Reduction (COSPAR) waveform design method as well as the cyclic PAPR reduction technique. In Section 5.6, we address the range resolution issue and widening of the mainlobe for COSPAR signals. Section 5.7 demonstrates the mutual orthogonality of COSPAR signals. Section 5.8 compares the Ambiguity Function and Doppler sensitivity of COSPAR signals with those of a typical LFM signal. Section 5.9 then compares the time–frequency distributions of COSPAR and LFM waveforms and proposes the Spectral Kurtosis (SK) measure for evaluating the LPI properties of signals. In Section 5.10 we address the experimental outcomes of the field trials.

5.1 Preferred Noise Radar Architecture

We find it beneficial to introduce the reader to the overall system architecture of noise radar of our interest. This will aid the reader in comprehending the noise radar operation and its accompanying signal processing.

Noise radar emits noise signals produced by analog noise sources (temperature-controlled resistors, Zener diodes, gas discharge tubes, etc.) or digital pseudo random noise generators. Due to the restricted capability of analog noise sources in terms of resolution and dynamic range, in our work, we are interested in digital waveforms created artificially on computing equipment such as computers, DSPs, and FPGAs. Therefore, we specifically refer to a conventional noise radar architecture with collocated transmit and receive antennas, as seen in Figure 5.1. In this architecture, the waveform is created or stored in a digital device, and the digital-to-analog converter feeds it to the transmitter. The block diagram has been simplified such that analog filters and signal conditioning components are not shown. For information on various kinds of architectures, interested readers can refer to [12].

In Figure 5.1, the complex baseband signal (noise waveform) is first created, followed by upsampling and digital upconversion (complex-to-real conversion) to the radar intermediate frequency (IF) band. Following this, the digital real IF band signal is sent into the Digital-to-Analog Converter (DAC) with sampling rate $f_{s_{\mathrm{DAC}}}$.

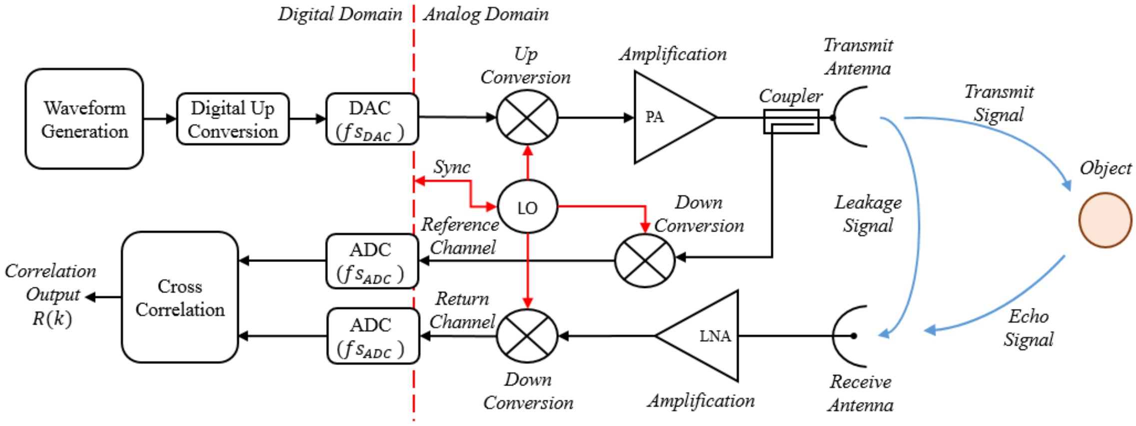

Figure 5.1: Block diagram of the preferred noise radar architecture

In the analog domain, the signal is first upconverted to the RF band by a mixer, next amplified by the power amplifier (PA), and then propagated via the antenna. A local oscillator (LO) provides the coherency by supplying the mixing signal required for up and down conversion. A copy of the transmit signal entering the antenna is tapped by an RF coupler and downconverted back into the IF band during transmission. The tapped IF signal is referred to as the "reference signal" because it is employed as the matching template in correlation processing. Alternately, the digital copy of the transmit signal stored in the digital processor can be employed for correlation processing. To include the nonlinear effects of the transmitter (i.e., those imposed on the transmit signal) in the correlation processing at the expense of an additional downconverter stage, the approach presented here is preferable. At the receive antenna, the weak echo signal that bounces back from the target object is first amplified by a low noise amplifier and then downconverted into the intermediate frequency (IF) band. This signal is known as the "return signal" (or "surveillance signal"), as its name implies. Analog-to-Digital Converters (ADCs) sample both reference and return signals at the ADC sampling rate $f_{s_{\mathrm{ADC}}}$, and cross-correlation is computed digitally in the hardware.

In this architecture, it is common to create the complex baseband signal with a sampling rate of $f_{s_{\mathrm{ADC}}}/2$, and to settle the IF band within the third Nyquist zone of ADCs ($f_{s_{\mathrm{ADC}}}$ to $3f_{s_{\mathrm{ADC}}}/2$). In this design, the ADCs subsample the incoming reference and return signals, and then the spectrum folds over to the 1st Nyquist zone, eliminating the requirement for an additional digital downconverter prior to cross-correlation processing.

The noise radar in Figure 5.1 transmits and receives concurrently, resulting in an unavoidable leakage into the receiver due to the coupling of co-located antennas. As a result, this leakage has an impact on the dynamic range, which will be examined more in Section 5.3. In addition, the noise radar employs continuous wave (CW) emission, which provides covertness by eliminating rising and falling pulse edges (which are easily detected by ESM receivers) from its emissions. The continuous emission calls for the continuous processing of return signals which requires the receiver to perform signal processing at a high speed and with a low latency.

5.2 Correlation Processing and Its Implementation in Spectral Domain

The Matched filtering is the primary method for computing cross-correlation in noise radar. This approach is also referred as ”pulse compression” since it compresses the signal energy into a considerably tighter correlation mainlobe at the filter output. The ideal linear filter for optimizing the signal-to-noise ratio (SNR) when the received signal is contaminated by additive white noise [82] is the Matched filter. As a result, matched filters are commonly utilized in radar, where a known a priori signal is transmitted and the return signal reflected from objects is inspected for matching copies of the transmit signal.

In signal processing, a matched filtering is done via correlating a (potentially delayed and Doppler-compensated) template signal with an unknown signal to search for the presence of the template signal in the unknown signal. This is the same as convolving the received signal with a conjugated, time-inverted version of the broadcast signal. In this regard, we define the auto-correlation function (ACF) $R(\tau)$ of signal $s(t)$ as follows:

$$R(\tau) = \int_{-\infty}^{+\infty} s(t)s^*(t-\tau)dt \qquad -\infty < \tau < \infty \tag{5.1}$$

In reality, considering discrete time case, the waveform is both time and band limited. Therefore, from the perspective of the waveform, two choices exist for the correlation processing. One is periodic correlation, which assumes that the waveform is periodic and calculates the correlation using cyclic convolution. The alternative method assumes that the signal is aperiodic and calculates the correlation using linear convolution [3]. Due to the non-interlaced reception of signals required by the CW operation of noise radar, we opt for periodic correlation in our work. Given the discrete sequence $\mathbf{x} = \{x(n)\}_{n=0}^{N-1}$, we favor the frequency domain computation of correlation $\mathbf{r} = \{r(k)\}_{k=0}^{N-1}$ for convenience of digital implementation.

$$\mathbf{r} = \mathcal{F}^{-1}\{\mathcal{F}(\mathbf{x}) \circ \mathcal{F}^{*}(\mathbf{x})\} \tag{5.2}$$

where $\mathcal{F}(\cdot)$, $\mathcal{F}^{-1}(\cdot)$, $\circ$ and $(\cdot)^{*}$ represent, respectively, the Discrete Fourier Transform (DFT), the Inverse Discrete Fourier Transform (IDFT), the Hadamard product, and the complex conjugate operator. The sampled form of the ACF is represented by the sequence $\mathbf{r}$, where $r(k) := R(kT_{\mathrm{s}})$ and T_{s} is the sampling period. FFT engines are often available on digital hardware and is used to calculate DFT and IDFT.

Figure 5.2 is a block diagram depicting the digital hardware implementation of a periodic correlator. All arithmetic operations, including complex conjugation and complex multiplication in the block diagram are done on digital hardware such as an FPGA. The Hilbert Transform is implemented as a FIR filter structure, and FFT/IFFTs are calculated using Radix-2 or Radix-4 decompositions for DFT and IDFT, respectively. [50] proposes an example implementation of this kind.

Figure 5.2 also depicts the calculation of a signal's periodic autocorrelation and shows the power spectrum at each step during low IF sampling and Hilbert filtering. Here, we assume that an analog IF band (200–300 MHz) signal is injected into both ADCs at a sampling rate of $f_{\mathrm{s}_{\mathrm{ADC}}} = 200$ MSPS. The undersampling process converts the signal from the third Nyquist zone to baseband (DC-100 MHz), generating a low-pass alias of the intermediate frequency (IF) signal, and then the sampled signal goes through the Hilbert Transform where the analytic form of the signal is derived in order to preserve phase information required for the subsequent Doppler processing. The periodic correlation in the spectral domain is then computed using (5.2). Alternately, the complex-valued output of the Hilbert Transform can be downsampled by half to remove negative frequency components from the spectrum and to provide a decimated autocorrelation with a lesser number of resources required for FFTs in digital hardware (see Figure 5.2). The samples of the complex baseband

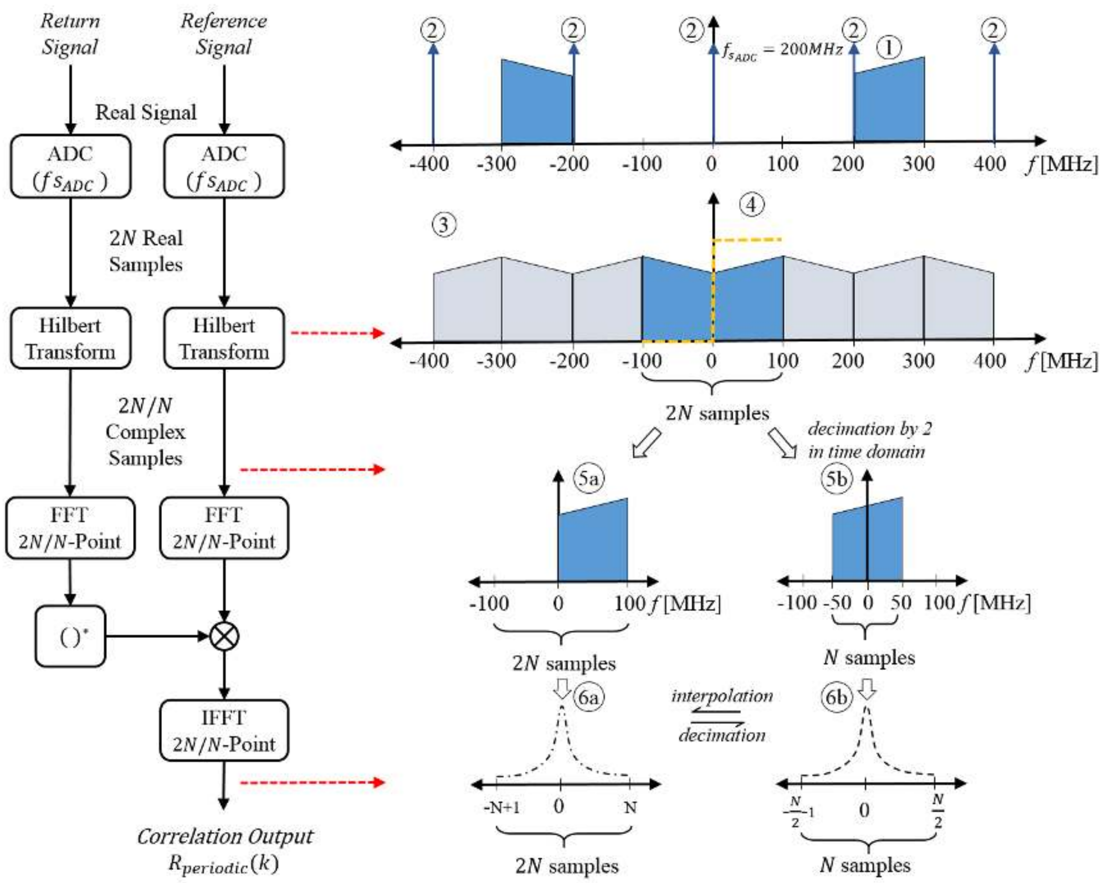

Figure 5.2: Periodic correlation processing in spectral domain. (1) Low IF signal spectrum. (2) The sampling comb spectrum at $f_{s_{ADC}} = 200$ MHz. (3) Their convolution and the low frequency alias (2N samples) of the IF signal. (4) Hilbert filter Transfer Function. (5a/b) Resulting low-pass component with 2N complex valued samples (N complex valued samples for the decimated case). (6a/b) Periodic cross-correlation result with 2N complex valued samples (N complex valued samples for the decimated case).

signal should be created at the sampling rate (e.g., $f_{s_{ADC}}/2$) at which the correlation of the signal is computed in the digital backend. This avoids the ACF sidelobe distortion caused by sample rate incompatibilities.

5.3 Dynamic Range Considerations

After demonstrating the implementation of correlation processing, we will explore the dynamic range pecularities for noise radars. There are two significant aspects that affect the receiver's sensitivity: the waveform and the noise bandwidth of the radar system.

5.3.1 Correlation Sidelobe Fluctuations of Noise Signals

In noise radar, when standard bandpass Gaussian noise is used as the probing waveform, the correlation processing of noise signals of duration T and bandwidth B generates 'random sidelobe fluctuations' (sometimes referred to as 'range sidelobes') whose mean level '$\mathrm{SLL}_{\mathrm{mean}}$' is equivalent to the 'time × bandwidth (BT)' product below the correlation mainlobe peak [53]:

$$\mathrm{SLL}_{\mathrm{mean(dB)}} = -10log_{10}(B \times T) \tag{5.3}$$

These "random sidelobe fluctuations" encompass the entire range swath, obscuring the visibility of weak objects with a low radar cross section (RCS), i.e., both adjacent and distant targets. This phenomenon is sometimes called the "masking effect."

Taking into account the unavoidable signal leakage caused by antenna coupling, the correlation processing brings up a zero-range target whose range sidelobes dictates the dynamic range lower bound of the noise radar. This leakage is regarded as the largest transmit signal (in terms of power) entering into the receiver; hence, cross-correlation computations are normalized relative to the leaking signal's peak response. In addition, the gain of the receiver is adjusted such that the leaking signal does not cause saturation.

5.3.2 Receiver Noise Considerations

In addition to the range sidelobes of the leakage signal, the cross-correlation of the reference signal with the receiver's internal noise must be considered. Assuming a receiver gain of G and a receiver noise figure of F, the receiver noise power P_{noise} at the ADC input is calculated as follows:

$$P_{\text{noise(dBW)}} = 10\log_{10}(\text{K} \times T_{\text{SYS}} \times B) + G_{\text{(dB)}} + F_{\text{(dB)}} \tag{5.4}$$

where K represents the Boltzmann constant, T_{SYS} represents the system temperature in Kelvin, and B represents the receiver bandwidth. Having an antenna isolation level of I, the leakage signal power P_{leakage} at the input of ADC is calculated as follows:

$$P_{\text{leakage(dBW)}} = P_{\text{tx(dBW)}} + I_{\text{(dB)}} + G_{\text{(dB)}} \tag{5.5}$$

where P_{tx} is the transmitted signal power from the transmitting antenna. The signal-to-noise ratio resulting from the leakage signal and receiver noise can then be defined as follows:

$$\text{SNR}_{\text{leakage}-\text{noise(dBW)}} = P_{\text{leakage}} - P_{\text{noise}} = P_{\text{tx(dBW)}} - I_{\text{dB}} - 10\log_{10}(\text{K}\times T_{\text{sys}} \times B) - F_{\text{(dB)}} \tag{5.6}$$

Ignoring quantization noise caused by the fixed wordlength of ADCs, the noise floor after correlation processing is finally defined as:

$$\text{Noise Floor}_{\text{(dB)}} = -\{\text{SNR}_{\text{leakage}-\text{noise}} + 10\log_{10}(B \times T)\} \tag{5.7}$$

Presuming a positive $\text{SNR}_{\text{leakage}-\text{noise}}$ ($P_{\text{leakage}} \gg P_{\text{noise}}$), this indicates that when a typical Gaussian noise signal is used as the transmission signal, the dynamic range lower bound is defined by the random sidelobe modulations of the leaking signal rather than the real noise floor due to the system internal noise ($\text{SLL}_{\text{mean}} >$ Noise Floor). As a result, an undesired sensitivity loss corresponding to $\text{SNR}_{\text{leakage}-\text{noise}}$ (in dBs) occurs. To avoid the SNR loss, the range sidelobes of

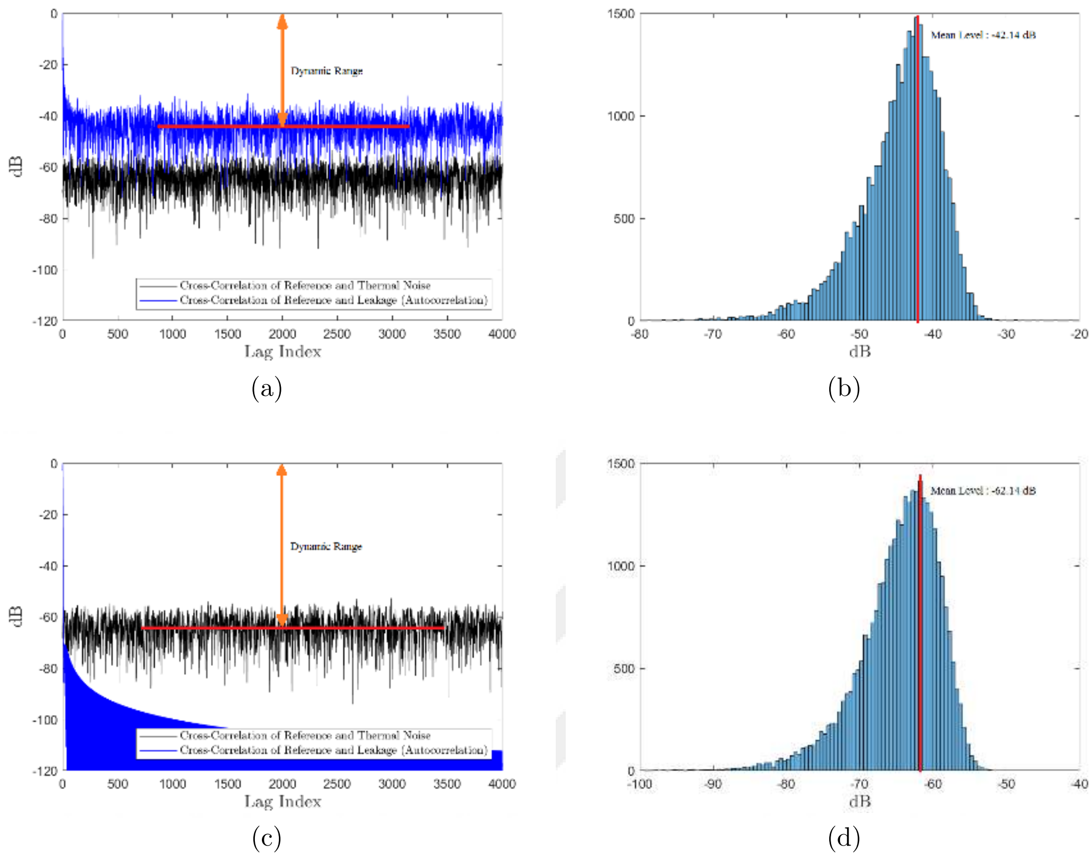

Figure 5.3: Dynamic range of noise radar. (a) Dynamic range is bounded by waveform sidelobes. (b) Dynamic range is bounded by noise floor. (c) Histogram of ACF sidelobes of Gaussian noise in Figure 5.3(a). (d) Histogram of correlation noise floor in Figure 5.3(c).

the noise waveforms must be reduced at least to the sidelobe level ($\mathrm{SLL}_{\mathrm{target}}$) defined as:

$$\mathrm{SLL}_{\mathrm{target}} < -\{\mathrm{SNR}_{\mathrm{leakage-noise}} + 10log_{10}(B \times T)\} \tag{5.8}$$

Figure 5.3(a, b) compares the dynamic ranges of bandpass Gaussian noise and an exemplary*tailored* noise signals with the same bandwidth and duration (B = 100 MHz, T = 164.84 μs), based on one-sided correlation plots (up to lag index 4000). Given a transmit power of 100 mW (20 dBm) and an antenna isolation level of 90 dB, the leakage power level at the receiving antenna is -70 dBm. Taking into account a receiver bandwidth of 100 MHz and a system temperature of 273 K, the thermal noise power is -93.97 dBm. If a typical receiver noise figure of 4 dB is considered, then the ratio of leakage power to noise power at the ADC input is:

$$\mathrm{SNR}_{\mathrm{leakage-noise}} = P_{\mathrm{leakage}} - P_{\mathrm{noise}} - F = -70 - (-93.97) - 4 \cong 20 \text{ dB} \tag{5.9}$$

In both instances, the cross-correlation between the reference signal and thermal noise would result in a mean noise floor equal to:

$$\text{Noise Floor}_{\mathrm{dB}} = -\mathrm{SNR}_{\mathrm{leakage-noise}} - 10\log_{10}(B \times T) = -(20 + 42.14) = -62.14 \text{ dB} \tag{5.10}$$

which corresponds to the histogram depicted in Figure 5.3d. As shown in Figure 5.3c, the dynamic range of the radar is constrained by the transmit signal's range sidelobes, which have a mean level of -42.14 dB for the Gaussian noise waveform. In contrast, when a tailored noise waveform is employed, such as an exemplary COSPAR waveform with -70 dB peak sidelobe level, the range sidelobes are significantly lower than Noise Floor (dB); as a result, the dynamic range is constrained by the system's thermal noise floor rather than the leakage range sidelobes leading to a wider dynamic range. The latter scenario is preferable in noise radar, and the example given here highlights the dynamic range issue and the requirement to manage the range sidelobes of noise waveforms. This mandates us to develop customized waveforms with the required correlation sidelobe qualities.

5.4 *Peak-to-Average Power Ratio Considerations*

The Peak-to-Average Power Ratio (PAPR) of signals is another significant parameter in noise radar. The PAPR of the radiated signal $x(t)$, represented here by discrete samples $\{x(n)\}_{n=0}^{N-1}$, is defined as follows:

$$\mathrm{PAPR} = \frac{\max\limits_{n} |x(n)|^2}{\frac{1}{N}\sum_{n=0}^{N-1} |x(n)|^2} \tag{5.11}$$

Signals with a constant amplitude envelope (termed "unimodular") have a PAPR

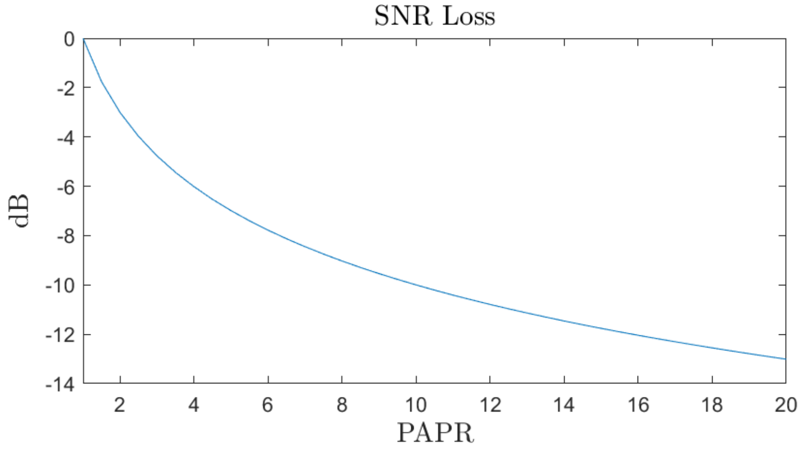

(a)

Figure 5.4: SNR loss versus PAPR.

rating of 1, making them the most power-efficient signals possible. LFM, Barker, and Polyphase codes are illustrative examples of waveforms belonging to this group. Such signals can drive the power amplifiers close to saturation, allowing the transmission power to be maximized. Any variation from the unitary amplitude level results in a loss of energy in the correlation mainlobe, hence decreasing the peak response level. This can be considered a reduction in SNR, resulting in a degraded detection capability. This unavoidable loss is characterized as:

$$\mathrm{SNR}_{\mathrm{loss}} = -10\log_{10}(\mathrm{PAPR}) \tag{5.12}$$

Figure 5.4 depicts the SNR loss versus various PAPR values. In this regard, a PAPR $<$ 2 is negligible in noise radar applications without significant detection performance degradation ($\mathrm{SNR}_{\mathrm{loss}} < 3$ dB).

In addition to SNR loss, nonconstant envelope signals are susceptible to nonlinear distortion effects of amplifiers, such as clipping, which degrades the correlation qualities of radiated signals. Therefore, signals with a large PAPR require highly linear converters, and amplifiers with a wide dynamic range add to the cost of designing a radar system.

5.5 Proposed Method: Combined Spectral Shaping and Peak-to-Average Power Ratio Reduction (COSPAR)

Having demonstrated the specific noise radar architecture and the fundamental periodic correlation processing scheme, along with some important noise radar technology-related aspects, we now propose a noise waveform generation method for controlling sidelobes and an accompanying PAPR reduction method for SNR maximization and linear amplifier operation. This approach for generating noise waveforms relies on a proper spectral shape (such as a Taylor window function), allowing for the sidelobes in its transformed domain to be controlled.

The Wiener-Khinchin theorem states that a signal's Power Spectral Density (PSD) is the Fourier transform of its Autocorrelation Function (ACF). The PSD and ACF therefore constitute a Fourier pair. Using this relationship, if one can specify a decent spectral shape (square root of PSD) with the appropriate ACF sidelobe qualities, then adding an arbitrary phase spectrum to that spectral shape and performing the inverse Fourier transform results in a single realization of a noise-like waveform. Using this strategy, it is possible to generate an infinite number of waveforms with the same PSD and ACF by randomly varying the phase term for each realization of signal spectra. In this regard, we utilize the Taylor window function for spectral shape creation, and after each realization, we employ our suggested PAPR reduction technique. Figure 5.5 illustrates the procedure, and the steps of the COSPAR approach are described in the subsections that follow.

5.5.1 Phase I: Spectral Shape Synthesis

The COSPAR technique begins with the construction of the spectral shape, which provides the desired correlation qualities. In this context, we refer to window functions in which designers can alter coefficients or window weights to make tradeoffs among mainlobe width, peak sidelobe level, and sidelobe fall-off rate factors.

In digital signal processing, window functions are commonly used to regulate unwanted sidelobes or decrease spectral leakage and Gibbs oscillations. Window

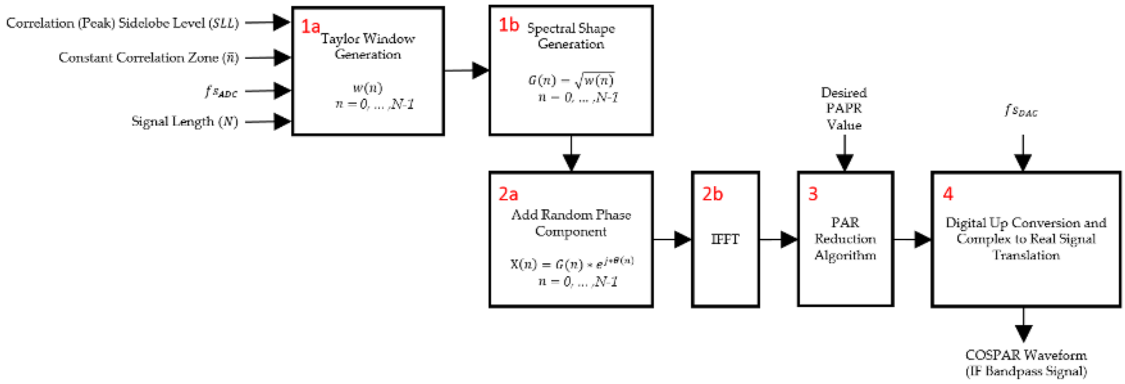

Figure 5.5: Illustration of COSPAR waveform synthesis method.

functions, also known as taper or apodization functions, have been created over the years to accomplish specific sidelobe features. Consequently, there is a vast body of research on window functions, and they are utilized extensively in applications such as spectral analysis, beamforming, and antenna design [93, 94].

In the COSPAR process, we rely specifically on the Taylor window function [95]. The Taylor window offers various advantages for noise radar waveform creation in comparison to other window functions:

(i) Peak sidelobe level (PSL) can be specified based on the correlation PSL that the radar design dictates.

(ii) It is possible to specify the length of near-in sidelobes for the desired range where flat sidelobe response is needed.

(iii) The tradeoff between mainlobe width and sidelobes has no appreciable impact on radar resolution. In Section 5.6, the modest broadening of the mainlobe width is addressed.

(iv) The favorable roll-off factor and monotonic decrease in sidelobes outside the constant sidelobe zone allow for the weak targets to be seen at large distance.

In fact, Taylor windows are comparable to the Chebyshev window, which is known to have the narrowest mainlobe for a given level of sidelobes; however, the

Chebyshev window comes at a cost in that flat equiripple sidelobes lead to edge discontinuity in the window function (in our case, the spectral shape), which is undesirable for LPI radar operation. The Taylor window allows us to make compromises between the sidelobe level and the mainlobe width while avoiding edge discontinuity.

After discussing the advantageous characteristics of the Taylor window, we construct a parameterized discrete Taylor window [96] with three parameters: N, $\bar{n}$ and SLL, where:

(i) N is the number of coefficient samples in the Taylor window;

(ii) $\bar{n}$ is the number of virtually constant sidelobe samples adjacent to the mainlobe.

(iii) SLL is the peak sidelobe level (in dB) relative to the peak of the mainlobe.

The Taylor window $\{w(n)\}_{n=0}^{N-1}$ of length N constructed as the sum of weighted $\bar{n}-1$ cosine functions as given in the following:

$$w(n) = \text{Taylor}(n, N, \text{SLL}, \bar{n}) = 1+2\sum_{m=1}^{\bar{n}-1} F_m \cos\left[\frac{2\pi m\left(n-\frac{N}{2}+\frac{1}{2}\right)}{N}\right] \quad n=0,\ldots,N-1 \tag{5.13}$$

In (5.13), the cosine weights are determined by:

$$F_m = \frac{(-1)^{(m+1)}\prod_{i=1}^{\bar{n}-1}\left[1-\frac{\frac{m^2}{\sigma^2}}{a^2+\left(i-\frac{1}{2}\right)^2}\right]}{2\prod_{\substack{j=1\\ j\neq m}}^{\bar{n}-1}\left(1-\frac{m^2}{j^2}\right)} \tag{5.14}$$

where

$$a = \frac{\ln(\eta+\sqrt{\eta^2-1})}{\pi} \tag{5.15}$$

$$\eta = 10^{-\frac{\text{SLL}}{20}} \tag{5.16}$$

$$\sigma^2 = \frac{\bar{n}^2}{a^2+(\eta-1/2)^2} \tag{5.17}$$

Figure 5.6 depicts an example of a discrete Taylor window with the parameters $N = 128$, $\bar{n} = 20$ and SLL $= -70$ dB, and its PSD. Once the Taylor window $w(n)$ is generated, it is used to construct the spectral shape function $\mathbf{G} = \{G(n)\}_{n=0}^{N-1}$ specified by $G(n) = \sqrt{w(n)}$ for $n = 0, \ldots, N-1$.

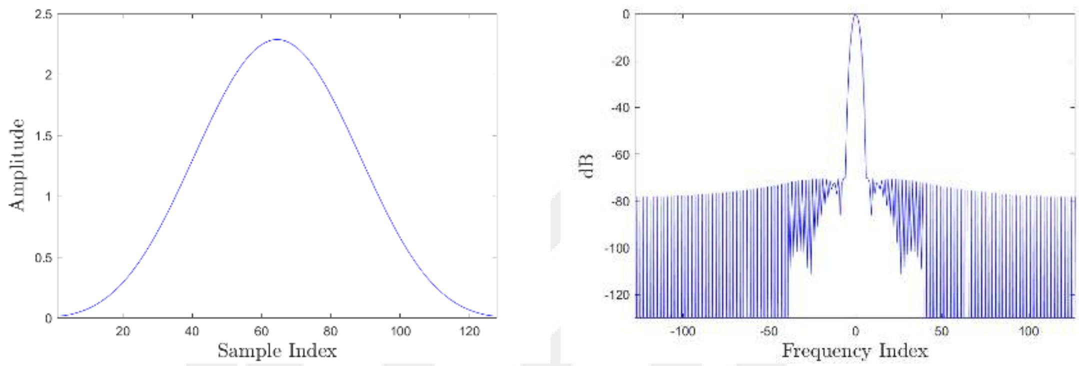

(a) (b)

Figure 5.6: Taylor window and its power spectral density.

5.5.2 *Phase II Signal Synthesis*

After synthesizing the spectral shape according to the desired level of correlation sidelobes in Step I, we have $N = BT$ degrees of freedom, i.e., the ability to choose an arbitrary phase to generate the signal spectrum $\mathbf{X} = \{X(n)\}_{n=0}^{N-1}$, which is defined as:

$$X(n) = G(n) \cdot e^{j\theta(n)} = \sqrt{w(n)} \cdot e^{j\theta(n)} \qquad n = 1, 2, \ldots, N. \tag{5.18}$$

where $\theta = \{\theta(n)\}_{n=0}^{N-1}$ is a random vector on $(-\pi, +\pi)$ with a probability density function $p(\theta) = 1/2\pi$. Then, the baseband complex signal $\mathbf{x} = \{x(n)\}_{n=0}^{N-1}$ is calculated by the Inverse Fourier Transform of $\mathbf{X}$.

Up until this point, the COSPAR waveform synthesis technique will be illustrated with an example. However, in the later sections we will demonstrate how to lower the PAPR of the synthesized signal by optimizing the signal spectrum's phase samples.

Example 1

As an illustration of the design technique, suppose it is desired to develop an ACF pattern with near-in sidelobes of 20 samples ($\bar{n}$) and a sidelobe level of -60 dB. We wish to send and receive a radar waveform with a 100 MHz bandwidth and a 163.84 μs duration. This amounts to a total of 32768 samples, assuming an ADC sampling rate of 200 MSPS in the receiver. Since the signal has real-valued components, its power spectrum is symmetric, and thus we only need to construct the positive side of the power spectrum. Consequently, our waveform design challenge reduces down to the synthesis of a 16384-length complex sequence. This complex sequence is the complex envelope representation of the real-valued radar signal.

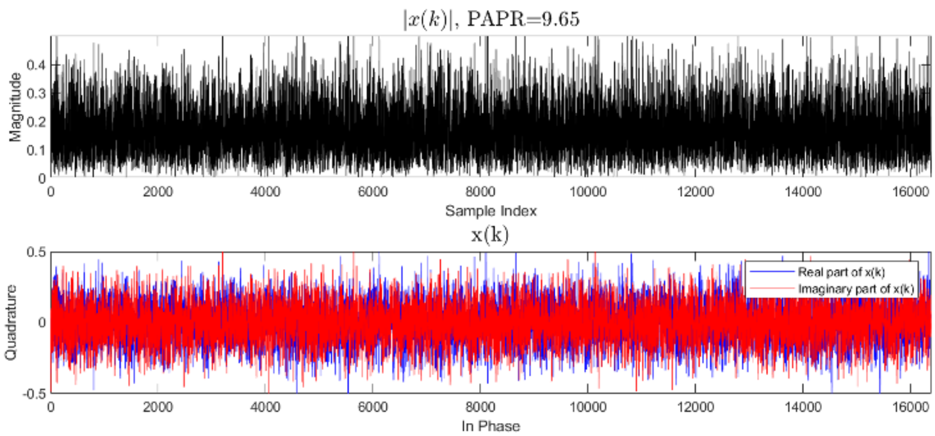

(a)

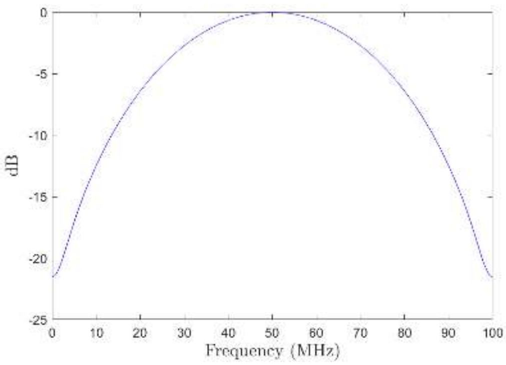

(b)

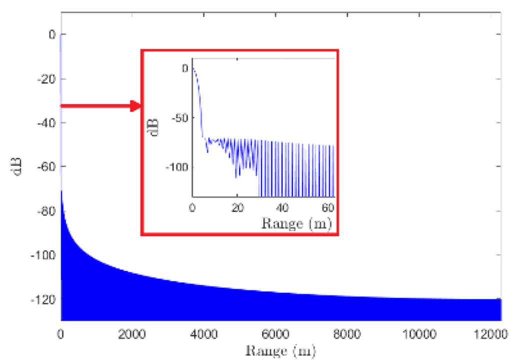

(c)

Figure 5.7: (a) COSPAR signal. (b) Normalized power spectral density of COSPAR signal. (c) Normalized one-sided autocorrelation of COSPAR signal.

After specifying the parameters, (5.13) is used to generate the spectral form. The constant-level sidelobe zone given by $\bar{n} = 20$ corresponds to a distance of $d = 30$ m, which is defined by $d = \frac{c}{2 \cdot f_{s_{ADC}}} \cdot \bar{n}$ where c is the speed of light.

Once the Taylor-shaped magnitude spectrum has been generated, a random phase vector is appended to the modulus of the spectrum, followed by the IDFT, which results in a single realization of the noise signal depicted in Figure 5.7a. Figure 5.7(b and c) depicts the Taylor-shaped power spectrum and the one-sided autocorrelation of the noise signal, respectively. We observe that the signal attains a considerably high valued $PAPR$ ($PAPR = 9.65$) as this can lead to inefficient transmitter power or degraded waveform features due to amplifier clipping.

5.5.3 Phase III: PAPR Reduction Procedure

Post-synthesis, the waveforms resemble noise because neither the envelope nor the quadrature and in-phase components have a predictable structure. In addition, randomizing the phase term of the Taylor-shaped spectrum in Phase II allowed us to construct infinitely many unique noise waveforms with distinct time–frequency distributions for each realization. In terms of power efficiency, the waveforms generated by this method are much inferior to classical waveforms such as LFM or NLFM, which have constant modulus, i.e. unimodular envelope. Experiments have shown that signals generated by COSPAR without the PAPR reduction step typically have a PAPR value between 8 and 11.

The challenge now is "how to lower PAPR without altering the signal's PSD and ACF envelope?" There are numerous PAPR reduction techniques for wireless communication, particularly for OFDM signals [97, 98]. Nonetheless, these algorithms are not directly applicable to radar signals because they are designed to preserve the information content (i.e. symbols) of the transmission signal while improving the code. For radar signals, there is an algorithm [99] based on alternating projection that gives a viable and efficient approach for forcing the signal to achieve the necessary PAPR. This approach searches a tight frame for a given structure (e.g., PAPR, norm) by projecting a frame whose spectrum describes it. The solution is located

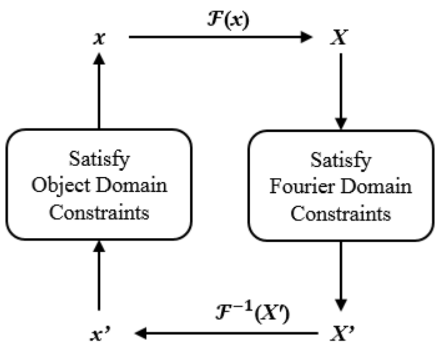

(a)

Figure 5.8: Gerchberg–Saxton phase retrieval algorithm.

at the intersection of the vectors that fulfill the provided PAPR constraint and the vectors that satisfy specific spectral restrictions. The disadvantage of this method is that the final solution has a somewhat modified spectrum, which degrades the excellent sidelobe features of the ACF. We choose not to utilize this strategy and instead propose a new technique based on alternating time–frequency domain projection. In our method, we approach the problem analogously to the Phase Retrieval problem [100], and our procedure is based on the well-known Gerchberg–Saxton algorithm [101], which is frequently used for recovering the underlying complex signal (e.g., a picture) from Fourier magnitude data. In this algorithm, the signal is projected onto the Fourier and object domains successively until a defined criterion is reached, while Fourier domain constraints and object domain constraints are applied, respectively, to each domain. Figure 5.8 illustrates the technique.

Algorithm 4 PAPR Reduction Procedure

```
Initialization:
Initialize x = {x(n)}_{n=0}^{N-1} having a known spectral shape G = {G(n)}_{n=0}^{N-1} (e.g., Taylor window) or ACF
Set PAPR_target or improvement factor ϵ as a termination condition
i=1
Repeat
Calculate PAPR^(i) of x
γ = rms(x)
for k = 0 to N − 1 do
    if |x(k)|^2 > PAPR_target · γ^2 then
        x(k) = sqrt(PAPR_target · γ^2) · x(k)/|x(k)|
        Θ = arg(F(x))
        x = F^{-1}(G ∘ e^{jΘ})
    else
        x(k) = x(k)
    end if
end for
i = i + 1
Calculate PAPR^(i+1) of x
Until a prespecified PAPR (PAPR^(i+1) ≤ PAPR_target) is reached or stop criterion (|PAPR^(i) − PAPR^(i+1)| ≤ ϵ) is satisfied
```

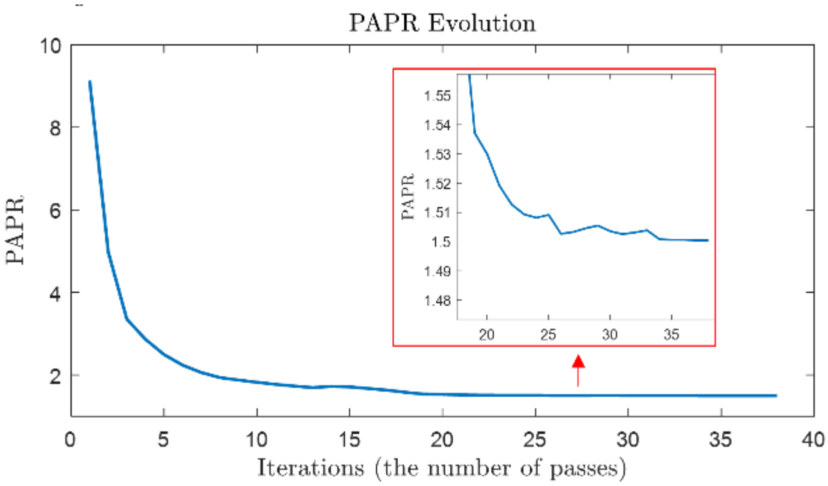

(a)

Figure 5.9: PAPR evolution over iterations.

In our procedure, the sequence created at Phase II is used to initialize our algorithm. In time domain, the overshooting sample ($|x(k)|^2 > \mathrm{PAPR}_{\mathrm{target}} \cdot \mathrm{rms}(x)^2$) of the sequence is subjected to a time domain constraint i.e., clipping, and whenever clipping takes place on a sample-by-sample basis, it is subsequently projected to the frequency domain. We project it back to the time domain after applying the spectral constraint in the frequency domain, which forces it to have the magnitude spectrum acquired in Phase I while preserving the adjusted phase spectrum. This alternation is repeated for each overshooting sample in turn across the full vector while the projection is carried out using FFT/IFFT procedures. At the end of each pass through the full vector, this iteration continues until a desired stop criterion (such as a PAPR value or PAPR improvement) is achieved. It should be noticed that in order to reduce overshooting sample regrowth and speed up convergence, this cyclic iteration acts sample-by-sample on each overshooting sample. When the last sample of the sequence is reached, the stop requirement is only ever tested once. It has been found that the suggested method reduces PAPR on each pass across the full sequence and converges to the target PAPR level. As a result, it is possible to achieve almost unitary (PAPR ≈ 1) signals without changing the PSD and ACF. In Algorithm 4, we define the steps of algorithm for the PAPR reduction process. The approach is then illustrated with an example.

Example 2

We start the PAPR reduction procedure with the sequence obtained in *Example 1* ($\mathbf{x} = \{x(n)\}_{n=0}^{N-1}$). The initial PAPR of the sequence is 9.13, and our target PAPR is set to 1.5. After multiple passes, it has been demonstrated that the PAPR value quickly falls below 2. The rate of improvement and convergence declines as the PAPR value approaches the target PAPR. Therefore, in order to save runtime, it is better to halt the algorithm according to an improvement factor ($|\mathrm{PAPR}^{(i)} - \mathrm{PAPR}^{(i+1)}| \leq \epsilon$) as opposed to satisfying an exact PAPR value condition. In Figure 5.9, the convergence graph is illustrated.

The final sequence depicted in Figure 5.10 has the same power spectrum as the starting sequence (shown in Figure 5.7a), and its ACF (shown in Figure 5.7b) has been preserved. Note that when the waveform is upconverted to IF band, the PAPR may increase by 2–3 dB [102] on average. Therefore, it is recommended that either an a priori margin be considered for the system or the signal be upsampled (stretched in the frequency domain via zero padding) to the $f_{s_{\mathrm{DAC}}}$ rate prior to executing the PAPR reduction procedure.

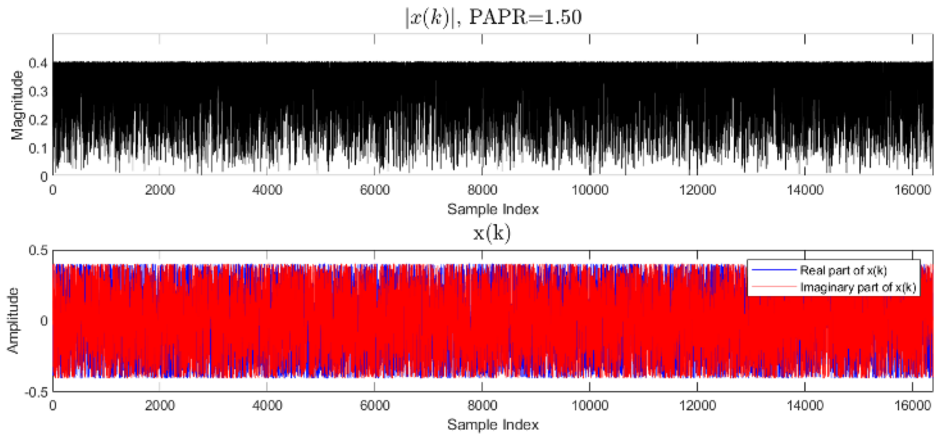

Figure 5.10: The PAPR optimized COSPAR signal (PAPR = 1.5). The power spectrum and ACF of the signal are retained and they are the same as in Figure 5.7(b and c), respectively.

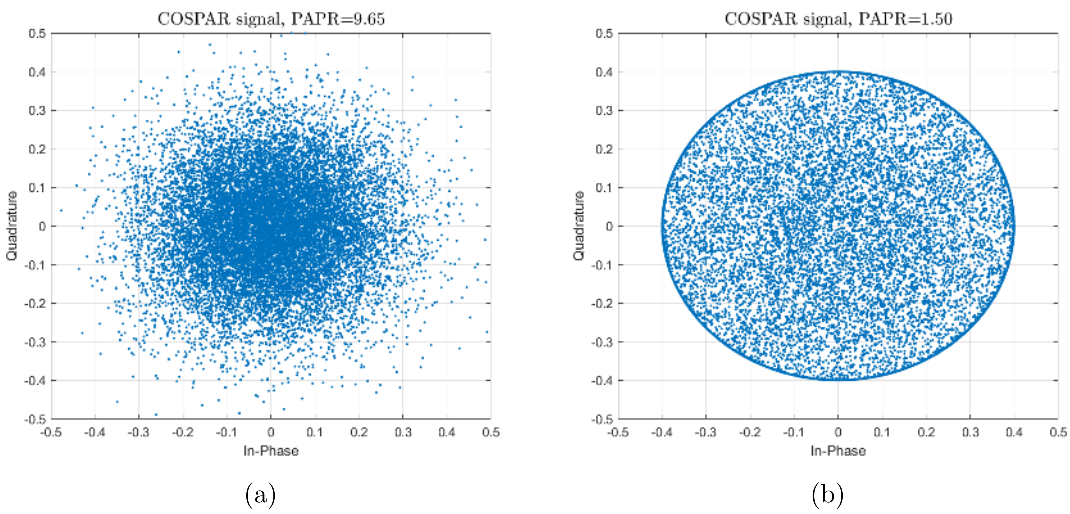

Figure 5.11: Constellation diagram of the COSPAR signal. (a) Before PAPR reduction. (b) After PAPR reduction

5.5.4 Phase IV: Quadrature Vector Modulator and Upconversion

In the final phase, the PAPR optimized complex baseband COSPAR signal $\{x(n)\}_{n=0}^{N-1}$ must be upconverted to the IF band so that discrete samples of the synthetic waveform can be converted to analog signal by the DAC for transmission. Assuming an integer oversampling factor $\eta = f_{\text{sDAC}}/f_{\text{sADC}}$, we add zeros to both sides of the COSPAR spectrum so that the new sample size becomes $N' = 2\eta N$, where N is the sample size of the complex baseband signal. This frequency domain extension is equivalent to $SINC$ interpolation time domain. Next, using the quadrature vector modulation method described below, we upconvert the interpolated complex signal $\{x'(n)\}_{n=0}^{N'-1}$ to the IF band:

$$y(n) = Re\,(x'(n))\,cos(2\pi f_{\text{c}} n/f_{\text{sDAC}}) - Im\,(x'(n))\,sin(2\pi f_{\text{c}} n/f_{\text{sDAC}}) \tag{5.19}$$

where f_{c} denotes the center frequency of the IF band and $\{y(n)\}_{n=0}^{N'-1}$ is the real

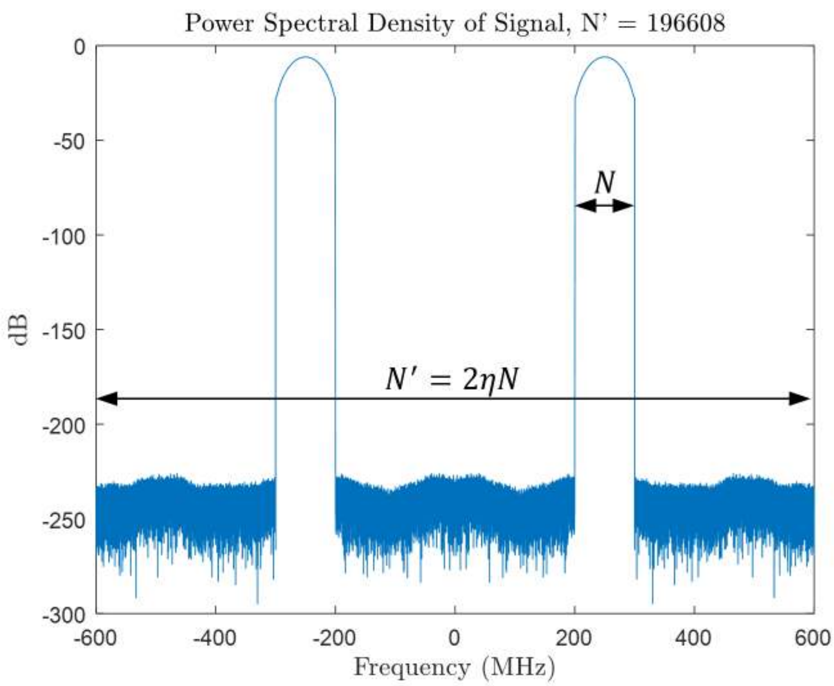

Figure 5.12: PSD of the COSPAR signal (feeded to the Digital-to-Analog Converter) in IF band (200–300MHz). Note that the PSD floor outside the IF band is theoretically zero.

signal in the IF band.

Example 3

Using the COSPAR waveform generated in Step III (Example 2), we wish to up-convert the baseband signal to the IF band (200 MHz–300 MHz) at the 1200 MSPS DAC sampling rate. The oversampling factor is therefore $\eta = (f_{s_{\mathrm{DAC}}})/(f_{s_{\mathrm{ADC}}}) = 6$. The sample size is then increased in the frequency domain, resulting in a new sample size of $N' = 2\eta N = 196608$. Applying quadrature vector modulation with a carrier frequency of $f_c = 250$ MHz yields the final signal. Figure 5.12 depicts the power spectrum of the real COSPAR signal.

5.6 Range Resolution Considerations

In theory, the radar range resolution ΔR for radars employing modulated signals with a bandwidth of B is $\Delta R = c/2B$, where c is the speed of light. This is the distance between the -3 dB points in the ACF mainlobe relative to the peak response. In the COSPAR signal production technique, the intended level of correlation sidelobes and the parameters used to construct the Taylor window function somewhat affect the initial ΔR by a factor ρ. The following expression can be used to approximate the altered range resolution $\Delta R'$ for a COSPAR signal with a bandwidth extension of B:

$$\Delta R' \cong \rho \cdot \Delta R = \rho \cdot \frac{c}{2B} \tag{5.20}$$

the mainlobe broadening factor ρ is defined by the following:

$$\rho = \sigma \frac{2}{\pi} \sqrt{(arccosh\ \eta)^2 - \left(arccosh\ \frac{\eta}{\sqrt{2}}\right)^2} \tag{5.21}$$

where η and σ are calculated according to (5.16) and (5.17), respectively. Figure 5.13 illustrates the mainlobe modification factor for different lateral lobe characteristics.

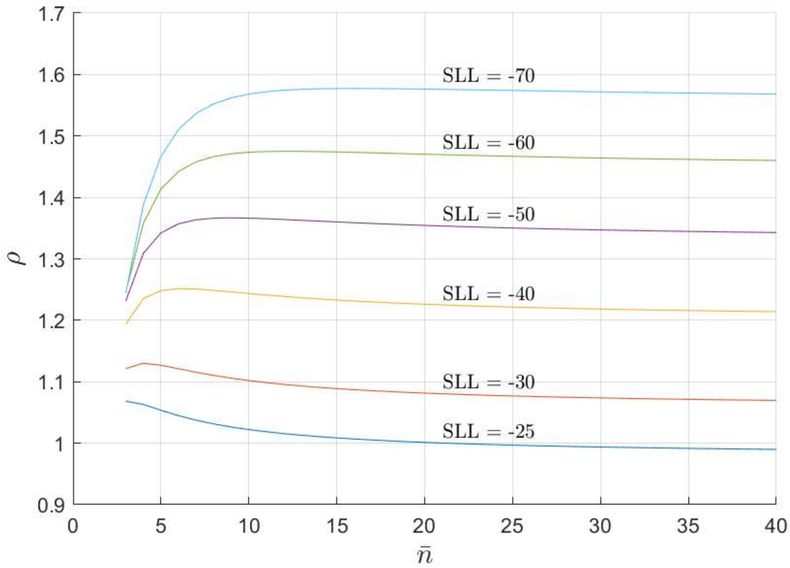

Figure 5.13: Mainlobe broadening factor versus $\bar{n}$ and SLL values.

5.7 Orthogonality Considerations

Each COSPAR synthesis results in a unique realization of a noise signal and enables the generation of a collection of mutually orthogonal noise waveforms. When utilized in succession, these orthogonal waveforms eliminate range ambiguities in the radar while simultaneously enhancing the LPI feature. Additionally, it allows many radars to operate in the same area and share the same spectrum. Cross-correlation of two separate COSPAR signals with the same energy and $PAPR = 1.5$ is depicted in Figure 5.14. The cross-correlation level reaches a mean of $-10\log_{10}(B \cdot T) \cong -42.17$ dB.

5.8 Ambiguity Function of COSPAR Signals

The Ambiguity Function (AF) of a signal is a representation of the signal's matched filter response against varying time delays and Doppler shifts, and it can be used for evaluating signal resolution in Doppler and range space and determining waveforms' Doppler tolerance [5,72]. Ambiguity Function of a narrowband signal $s(t)$ is defined

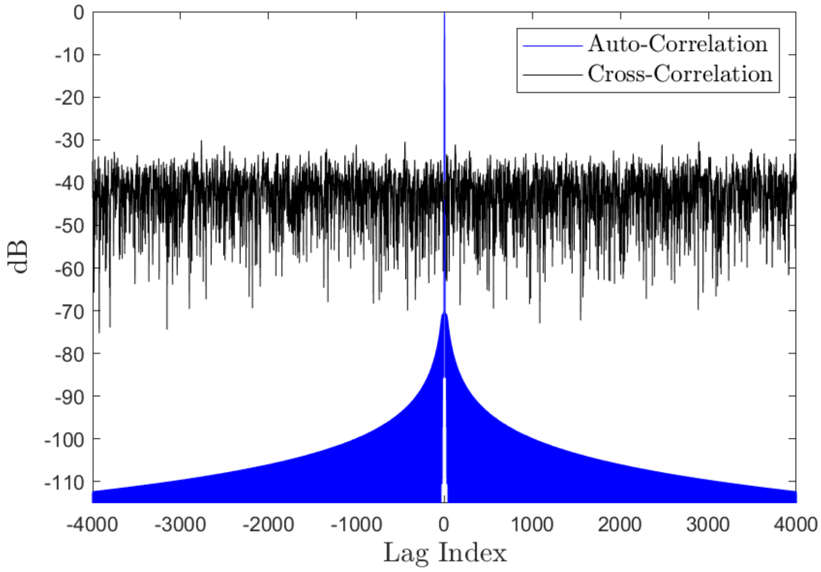

Figure 5.14: Crosscorrelation and autocorrelation of two COSPAR realizations (Normalized with respect to $r(0)$.

as follows:

$$\chi(\tau, f_d) = \int_{-\infty}^{\infty} s(t)s^*(t-\tau)e^{-j2\pi f_d(t-\tau)}dt \tag{5.22}$$

where τ is the time delay and f_d is the Doppler frequency. However, in the ensuing analysis for the COSPAR signal, we will use the discrete (narrowband) ambiguity function $\tilde{\chi}(k,p)$ defined in (A.31), as we are dealing with complex baseband signals. The modulus equivalence of the RF signals' AF and the AF of their underlying baseband signal is also shown in Appendix-A.

Figure 5.15 depicts a comparison of COSPAR and conventional LFM (chirp) signal AFs. In this regard, the LFM waveform is *Doppler-tolerant*, so that the matched filter still outputs a peak when the return signal incurs a Doppler frequency shift despite some offset in the apparent range of the target. This is referred to as *"range-Doppler coupling,"* and to determine the true range, an up and down chirp pair is typically utilized to average the detection offset from each chirp's opposing slopes [103]. COSPAR, on the other hand, shows a typical noise waveform with an AF shape resembling a thumbtack that has a high range and Doppler resolution. In

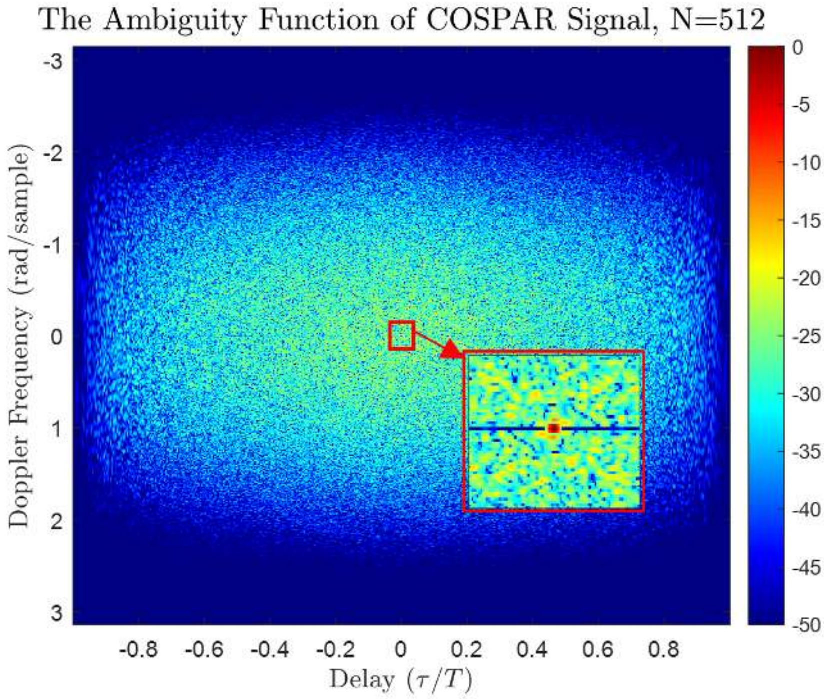

(a)

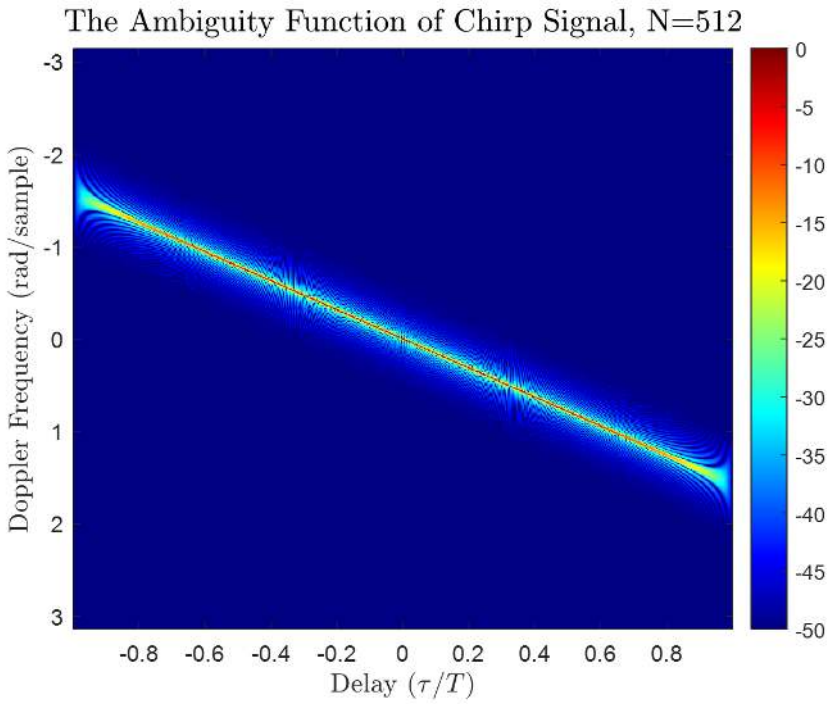

(b)

Figure 5.15: (a) Ambiguity function of a COSPAR signal. (b) Ambiguity function of a LFM signal.

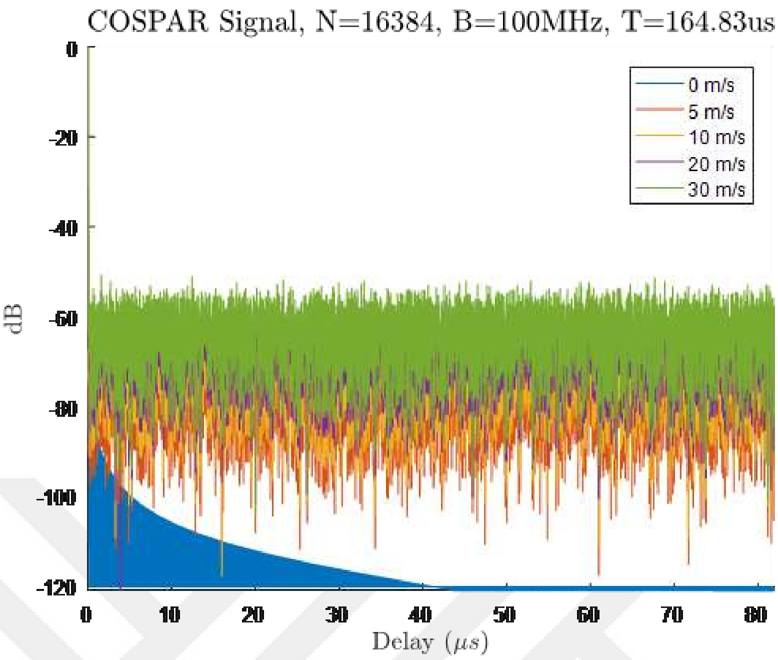

(a)

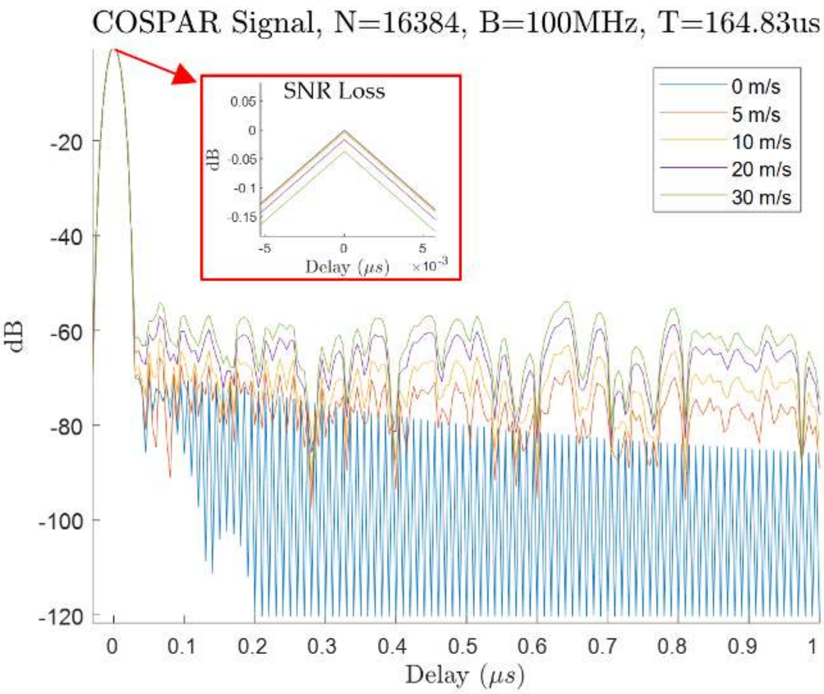

(b)

Figure 5.16: (a) ACF versus target radial velocity for 0 m/s, 5 m/s, 10 m/s, 20 m/s, 30 m/s. (b) Correlation sidelobes adjacent to mainlobe and negligible SNR loss due to Doppler mismatch.

this case, however, the Doppler shift will result in a loss in processing gain, and as a result, the SNR of the target response will drop significantly. Therefore, noise waveforms are regarded as *Doppler-sensitive*. This issue is remedied in noise radars by either performing pulse compression with a bank of filters suited to a selection of desired Doppler frequencies, or utilizing the efficient range-filter bank method introduced in [104].

In continuous wave noise radar, however, the waveform can still be Doppler-tolerant for some Doppler frequency shifts given the proper integration time. In case of a X-band (e.g., 9.3-9.4 GHz) marine radar, the typical vessel velocities range from 0 to 30 m/s (0 to 60 knots), resulting in a maximum Doppler frequency shift of $f_{\mathrm{D}} \cong \pm 2$ kHz. Figure 5.16a demonstrates that if we employ a tailored noise signal with a duration of 164.83 μs, such as the COSPAR signal generated in *Example 3*, we would still observe a moving target response from the matched filter. For COSPAR signals, there is no range offset and the SNR loss ($\sim$ 0.05 dB) in peak response due to the negligible Doppler shift (see Figure 5.16b). Moreover, despite minor degradation, the range sidelobes are still well below the $10\log(1/BT) = -42.14$dB level.

5.9 LPI Considerations and Time–Frequency Analysis

In terms of temporal analysis, the noise-like characteristics of COSPAR signals have been covered in preceding sections. From a spectral perspective, the COSPAR signal develops a deterministic spectral shape throughout its synthesis that is dictated by the Taylor window function (see, for example, Figure 5.7b), which at first glance can be viewed as a vulnerability in terms of Electronic Protection. Unless the exact bandwidth and length of the signal is known in advance, calculating the spectrum of the continuously emitted COSPAR signal from an arbitrary capture of its broadcasts is no easier than predicting the spectrum of any other legacy LPI waveforms. As a result of the Taylor window function, there are no spectral discontinuities, and its smooth roll-off at band edges makes it an excellent option for LPI operation. In addition, its strength is derived from the time–frequency representation explained below. In addition to standard spectral analysis approaches, modern ESM systems may provide time–frequency analysis maps [60]. In this manner, these ESM systems can intercept the commonly utilized LFM and its variant NLFM signals of so-called LPI radars. Several approaches utilized in time–frequency domain signal analysis are founded on:

- Short Time Fourier Transform (STFT) [105].
- Wigner–Ville Distribution (WVD) [106].
- Choi–Williams Distribution (CWD) [107].

Time-frequency graphs offer more understanding of the signal than conventional techniques. Therefore, the STFT and Wigner-Ville Distribution of these signals are shown in Figure 5.17(a-d) to evaluate and compare the time-frequency distribution of conventional LFM and COSPAR waveforms. Our first finding is that the COSPAR signal's energy is evenly distributed across the whole time-frequency plane, turning out challenging for an electronic reconnaissance system to analyze the signal. As a result, it is thought that for ESM receivers, obtaining signal features from the COSPAR signal analysis is a difficult task. Then, the following question arises: "How can we determine if a signal resembles noise and is viable for LPI operation?"

In this work, the Spectral Kurtosis (SK) measure is utilized to quantify the LPI features. Spectral Kurtosis is a statistical method that can reveal nonstationary and non-Gaussian frequency component distributions. A low value of Spectral Kurtosis for a frequency bin suggests the presence of stationary Gaussian noise, whereas a high value indicates the presence of a transient or structured signal at that frequency [108,109]. This makes Spectral Kurtosis a valuable and effective method for assessing the LPI features of radar noise waveforms. The Spectral Kurtosis of a signal $x(t)$ can be calculated using its spectrogram, which is generated using the STFT (Short

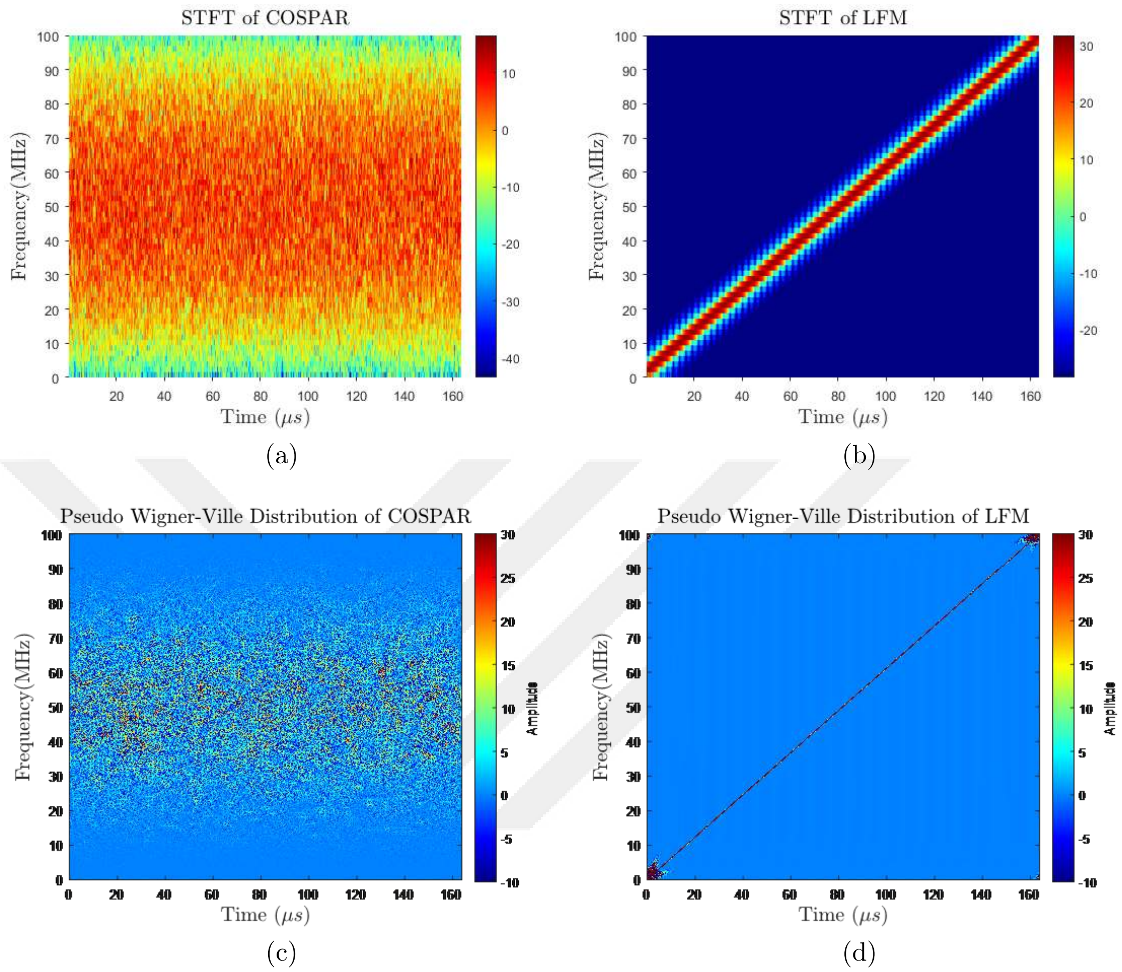

Figure 5.17: (a) STFT of COSPAR signal. (b) STFT of LFM signal. (c) Pseudo Wigner–Ville Distribution of COSPAR signal. (d) Pseudo Wigner–Ville Distribution of LFM signal.

Time Fourier Transform) $S(t, f)$:

$$S(t,f) = \int_{-\infty}^{\infty} x(t)l(t-\lambda)e^{(-j2\pi ft)}dt \tag{5.23}$$

where $l(t)$ is the window function used in STFT. Then, SK is defined by:

$$\text{Spectral Kurtosis } K(f) = \frac{\langle |S(t,f)|^4 \rangle}{\langle |S(t,f)|^4 \rangle^2} - 2 \quad f \neq 0, \tag{5.24}$$

where $\langle \cdot \rangle$ denotes the time-average operator.

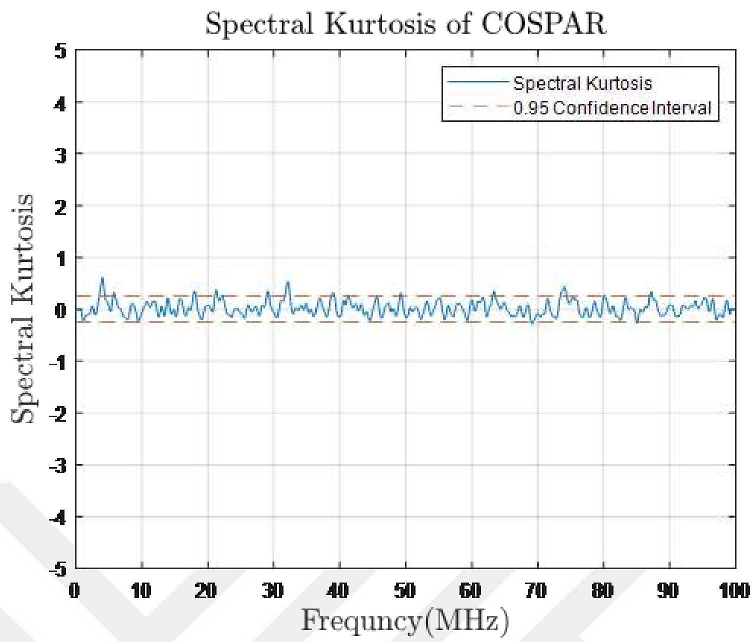

(a)

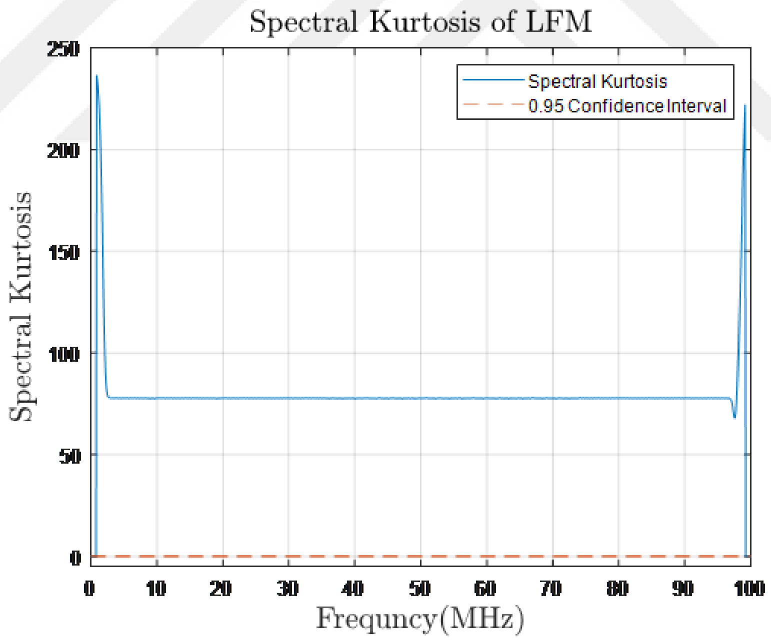

(b)

Figure 5.18: (a) Spectral Kurtosis of COSPAR signal. (b) Spectral Kurtosis of LFM signal.

As depicted in Figure 5.18, the distribution of frequency bins over time for the COSPAR signal tends to have a normal distribution, resulting in a practically zero

Spectral Kurtosis value, suggesting a noise-like distribution (normal distribution) for all frequency bins over time. In contrast, the LFM signal has a high Spectral Kurtosis value across the whole frequency band, indicating that the signal has a structured time–frequency support. Due to the signal's noise-like characteristics, the COSPAR signal might be obscured by the ESM receiver's internal thermal noise, making it difficult for the ESM system to distinguish the signal from its internal noise and to identify the radar emitter.

5.10 Experimental Results

In January 2021, sea experiments of the noise radar demonstrator developed by the Turkish Naval Research Center Command (TNRCC) were undertaken at a shore-based test location. The architecture of the demonstrator system is depicted in Figure 5.1. During trials, the demonstrator was configured to operate in X-band, and raw data from marine targets of opportunity were gathered for offline analysis. Figure 5.19 is a radar scan view of the scene obtained using COSPAR recordings, which reveals numerous ship targets at sea and land buildings within eight kilometers of the test location.

The COSPAR signal, which was produced in *Example 3* with a bandwidth of 100 MHz and a period of $T = 164.84\ \mu s$, was utilized in these tests, and the outcomes were compared to those of a 100 MHz Gaussian noise waveform produced with the identical radar settings. We captured the raw data while the demonstrator was staring at the ship target at a distance of around 2400 m, which is marked with a dashed white circle in Figure 5.19, in order to assess the COSPAR sidelobe performance against a Gaussian noise counterpart. Both of the range profile plots in Figure 5.20 clearly show the correlation spikes of ship's echoes. The strongest echo from the ship is roughly 8 dB above the leakage level (normalized to 0 dB), and the target's SNR is equivalent to ~ 48 dB for the COSPAR waveform, compared to ~ 38 dB for the case of Gaussian noise, based on the range profile. The sidelobes of the target response, not the leakage, dominate the matched filter dynamic range floor when the strongest echo from the ship is taken into account. Ground clutter

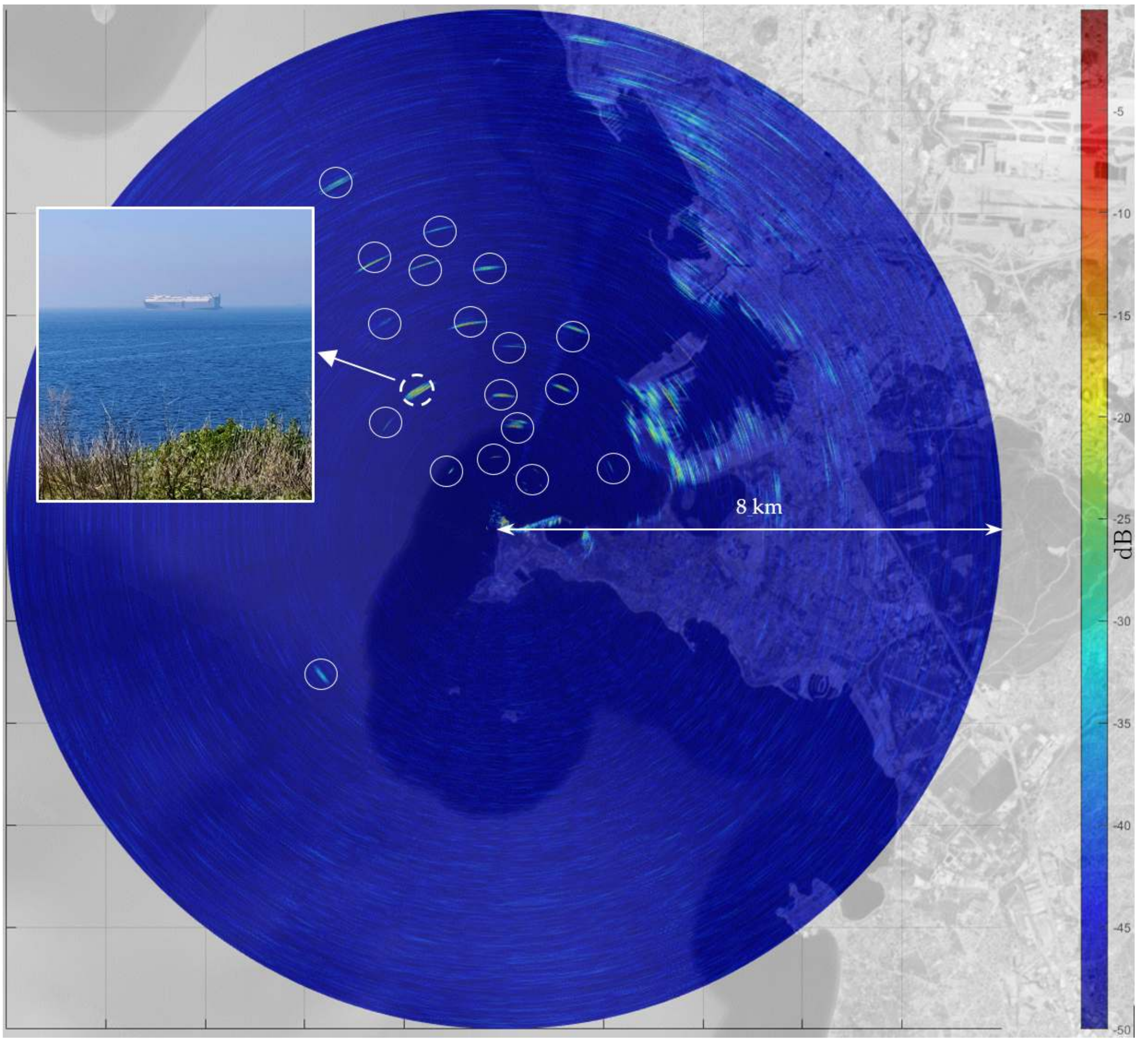

Figure 5.19: A surveillance scan (PPI) view obtained using COSPAR signal. Ship targets are encircled in white. The large ship target marked with dashed white circle is used for 1D range profile analysis.

close to the radar and the quantization noise of the digital converters cause the sidelobes for both waveforms to be higher than expected (-42 dB for Gaussian noise and -60 dB for COSPAR), which is why they are not at the predicted level. However, it is evident that using tailored waveforms, such as COSPAR signals, can increase the dynamic range and improve the sensitivity. We have demonstrated the utility of the suggested COSPAR waveform in this regard for a typical noise radar application.

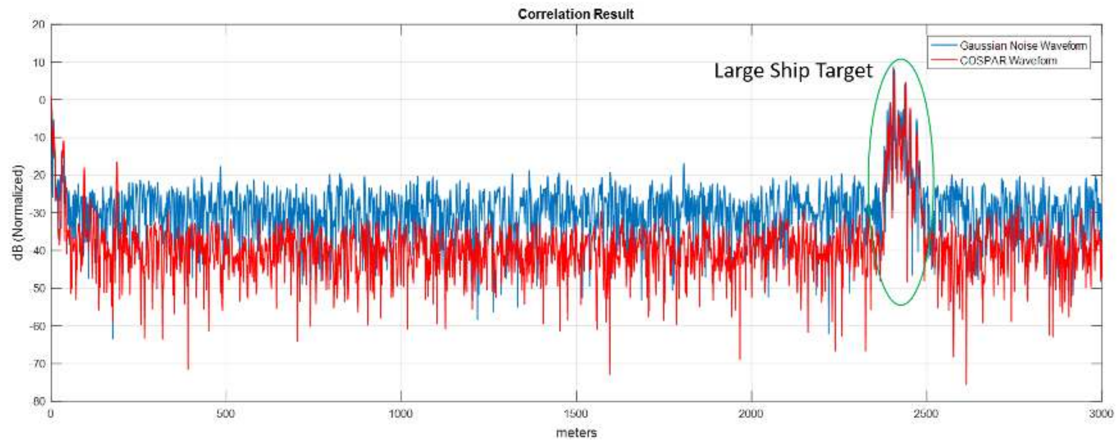

Figure 5.20: Comparison of range profiles of the ship target for Gaussian noise signal and proposed COSPAR waveform. COSPAR signal provides more room for better target SNR with lower sidelobes than Gaussian noise counterpart.

5.11 Summary

A novel noise waveform synthesis technique (named "Combined Spectral Shaping and Peak-to-Average Power Reduction, COSPAR") that incorporates a cyclic PAPR reduction algorithm has been presented in this chapter along with a review of the fundamental noise radar architecture and its correlation processing. Its low computational complexity and the ease of hardware implementation are its key features. By using the method, designers can adjust the Taylor window features for spectral shape synthesis and modify the related ACF near-in sidelobes and peak sidelobe level as necessary.

The COSPAR waveforms are an exception to the general category of noise radar waveforms in that, despite having a deterministic power spectral shape, each realization produces a distinct time domain signal with a unique time-frequency distribution, making them suitable for enhanced LPI operation. These waveforms are non-repetitive in this sense, making it difficult for ESM receivers to forecast or intercept them. The good attributes of COSPAR waveforms can be summed up as follows:

- The COSPAR waveforms resemble noise. It has been demonstrated that the signal energy is evenly distributed across their time-frequency plane despite the fact that they have a deterministic spectral form. The ESM receiver can easily intercept signals at a long distance if they have structured time-frequency support or the signal energy is concentrated within a specific band. COSPAR waveforms have strong LPI properties in this regard.

- Due to the assigned PAPR of the signal, the signal energy does not significantly change from pulse to pulse. Target SNR fluctuation caused by the varying transmit signal energy from pulse-to-pulse is therefore eliminated.

- Due to its prespecified autocorrelation envelope due to Taylor window, the matched filter outputs are unaffected by random range sidelobe modulation, and typical pulse compression radar signal processing techniques can be employed.

- Its thumbtack-shaped Ambiguity Function typically eliminates range and Doppler ambiguities.

In addition, the ability to shape the underlying autocorrelation function via parametric spectral shape synthesis (i.e., Taylor window) renders this type of waveform potentially useful for a variety of sensing applications, including automotive radar, marine navigation radar, surveillance radar, SAR imaging, and MIMO radar. As a result, COSPAR signals constitute a sort of waveform diversity for noise radars, providing degrees of freedom to modify sidelobe level and crest factor that may be readily utilized in a variety of sensing measurements.

Chapter 6

DESIGN OF SPECTRALLY COMPATIBLE WAVEFORMS FOR SPECTRUM-AWARE RADARS

In this chapter, we concentrate on designing unimodular periodic/aperiodic sequences with desirable spectral stopband features and good correlation sidelobes. We also propose an effective methodology based on a quasi-Newton optimization technique called the Limited Memory Broyden–Fletcher–Goldfarb–Shanno (L-BFGS) method. The proposed technique is hence referred to as the "L-BFGS-based Sequence Design (LBSD) Algorithm." The bi-objective (ACF sidelobe and spectral stopband restrictions) optimization issue is first converted via scalarization into an unconstrained single objective optimization problem and then it is handled as a nonlinear large-scale problem in the proposed LBSD algorithm. Then, this nonlinear and nonconvex objective function is efficiently solved using the L-BFGS method, in which the search direction is determined by a two-loop L-BFGS recursion [110].

An algorithm based on the L-BFGS was initially proposed in [111] for the creation of Multiple-Input-Multiple-Output (MIMO). Nevertheless, the algorithm in [111] differs from our suggested solution in a number of ways, including;

(i) Since the sequence set design problem is considered rather than a single sequence design problem, an objective function minimizes the autocorrelation sidelobes as well as the crosscorrelation level.,

(ii) It does not account for spectral stopbands, hence the approach cannot be used for SFW design.,

(iii) Step length is determined using the classic linear search method (Armijo line search), which is computationally intensive and results in a slow convergence rate.

Contrarily, our suggested method considers the Single-Input-Single-Output (SISO) signal design issue, resulting in a unique objective function. Additionally, we construct a cost function to concurrently handle the spectral stopband power and the autocorrelation sidelobes. By using the unit step length along the well-scaled search direction vector that was acquired by the L-BFGS recursion, our technique avoids the cost of step length computation. The only outliers in terms of step length selection are the initial m iterations and the iterations when L-BFGS recursion results in an ascending search direction. The Taylor series expansion strategy in [37], which is more efficient than the traditional searching strategies, and the typical steepest descent vector (i.e., the negative gradient) are both used in these few iterations to estimate the step length. Since step length calculation is mostly avoided and the gradient and step length are both computed by Fast Fourier Transform (FFT) operations together with Hadamard products, the proposed LBSD approach proves to be computationally efficient.

Following is a summary of the unique contributions made by this study:

(i) In order to generate unimodular aperiodic/periodic sequences with minimal autocorrelation sidelobes, a unique approach based on nonlinear optimization theory has been devised. In the quest for a quicker means of generating desired waveforms, this strategy is being explored.

(ii) This novel technique solves the bi-objecive (ISL and Spectral Stopband) sequence design problem more quickly and with less computing complexity than previous methods.

(iii) The algorithmic contribution is a nonlinear optimization method applied to the sequence design problem, together with a criterion for choosing the step size that improves the convergence rate of the iterative operation.

(iv) The numerical simulations verify that our suggested approach outperforms the state-of-the-art techniques in terms of convergence speed and suppression of correlation sidelobes and spectral stopbands.

The following sections of this chapter are organized as follows: In Section II, we outline the issue and propose the objective function that combines both the sidelobe correlation and spectral restrictions. Section III begins with the derivation of the phase gradient and the step length, followed by the derivation of the search direction through the L-BFGS technique and the phases of the LBSD algorithm. Section IV presents numerical findings from computer simulations and compares the algorithm's performance to that of contemporary algorithms. The topic finishes in Section V.

Notation

The following conventions and mathematical symbols are utilized throughout the remainder of this chapter. Matrices are represented by uppercase boldface letters, whereas column vectors are represented by lowercase boldface letters. $(.)^H$, $(.)^T$ and $(.)^*$ denote the conjugate transpose, transpose and complex conjugate operations, respectively. Element-wise product (Hadamard product) is denoted by $\circ$ and the Euclidean norm of vectors is denoted by $\|.\|$. $\mathrm{Diag}(\mathbf{x})$ is a diagonal matrix constructed from the elements of $\mathbf{x}$. Real and imaginary parts are denoted by $\mathrm{Re}(.)$ and $\mathrm{Im}(.)$, respectively. $\mathbf{X}(i,j)$ and $\mathbf{x}(i)$ denote the (i,j)'th entry of a matrix and ith element of a vector, respectively while $\mathbf{X}_{ij}$ and x_i denote the $(i+1, j+1)$'th element of a matrix and the $(i+1)$'th element of a vector, respectively. N-point FFT and inverse FFT (IFFT) operations are denoted by $\mathcal{F}_N(.)$ and $\mathcal{F}_N^{-1}(.)$, respectively.

6.1 Signal Model and Problem Formulation

This section deals with the design of a phase-only sequence with low autocorrelation sidelobes and appropriate spectral stopbands. Let $\mathbf{x} = \{x_n\}_{n=0}^{N-1} \in \mathbb{C}^{N\times 1}$ represent the N-length sequence to be designed. This sequence can be expressed directly in vector form as follows:

$$\mathbf{x} = [x_0, \cdots, x_{N-1}]^T. \tag{6.1}$$

Without imposing any limitations, we can suppose that the sequence is unimodular, i.e.,

$$|x_n| = 1, \quad n = 0, ..., N-1. \tag{6.2}$$

In the following subsections, we will first describe the Autocorrelation Function (ACF) and then discuss the constraints designed to reduce the power in the correlation sidelobes and frequency stopbands. Then, we will illustrate how to construct a unified (single) cost function to handle both constraints.

6.1.1 Autocorrelation Functions

The periodic and aperiodic autocorrelation functions of a sequence in (6.1) can be stated as follows:

$$\begin{aligned} \tilde{r}_i &= \sum_{n=0}^{N-1} x_n x^*_{((n-i) \bmod N)} = \tilde{r}^*_{-i}, \quad i = 0, ..., N-1, \\ r_i &= \sum_{n=i}^{N-1} x_n x^*_{(n-i)} = r^*_{-i}, \quad i = 0, ..., N-1, \end{aligned} \tag{6.3}$$

where mod is the modulo operator, and $\tilde{r}_i$ and r_i are the discrete samples of periodic and aperiodic autocorrelations, respectively. It should be noticed that the zero-lag correlation (peak response) is equal to N i.e., $r_0 = \tilde{r}_0 = \sum_{n=0}^{N-1} x_n x_n^* = N$ due to the unit-modulus property of the samples in (6.2).

6.1.2 Correlation Sidelobe Constraint

Correlation sidelobe quality is measured by the integrated sidelobe level (ISL), which is a measure of the total energy in the sidelobes. Our goal is to get an impulse-like correlation with almost null sidelobes by reducing the ISL. The ISL metric characterized by periodic and aperiodic correlation sidelobes are defined by:

$$\mathrm{ISL}_{\mathrm{pe}} = \sum_{i=1}^{N-1} |\tilde{r}_i|^2, \quad \mathrm{ISL}_{\mathrm{ap}} = \sum_{i=1}^{N-1} |r_i|^2, \tag{6.4}$$

where the terms $\mathrm{ISL}_{\mathrm{pe}}$ and $\mathrm{ISL}_{\mathrm{ap}}$ refer to the periodic and aperiodic ISL, respectively. Let

$$\begin{aligned}\mathbf{r}_{\mathrm{pe}} &= \left[\tilde{r}_0, \tilde{r}_1, ..., \tilde{r}_{N-1}\right]^T, \\ \mathbf{r}_{\mathrm{ap}} &= \left[r_0, r_1, ..., r_{N-1}, 0, r_{N-1}^*, ..., r_1^*\right]^T,\end{aligned} \tag{6.5}$$

be the respective periodic and aperiodic autocorrelation vectors. The ISL expressions in (6.4) can then be stated as

$$\begin{aligned}\mathrm{ISL}_{\mathrm{pe}} &= \sum_{i=0}^{N-1} |\tilde{r}_i|^2 - |\tilde{r}_0|^2 = \mathbf{r}_{\mathrm{pe}}^H \mathbf{r}_{\mathrm{pe}} - N^2, \\ \mathrm{ISL}_{\mathrm{ap}} &= \frac{1}{2} \sum_{i=1-N}^{N-1} |r_i|^2 - |r_0|^2 = \frac{1}{2}\left(\mathbf{r}_{\mathrm{ap}}^H \mathbf{r}_{\mathrm{ap}} - N^2\right).\end{aligned} \tag{6.6}$$

Let $\mathbf{D}_{\tilde{N}}$ represent the $\tilde{N} \times \tilde{N}$ Discrete Fourier Transform (DFT) matrix specified by

$$\mathbf{D}_{\tilde{N}}(m,n) = e^{-j\frac{2(m-1)(n-1)\pi}{\tilde{N}}}, \quad m,n = 1, ..., \tilde{N}, \tag{6.7}$$

the inverse Discrete Fourier transform (IDFT) matrix may then be calculated using $\mathbf{D}_{\tilde{N}}^H/\tilde{N}$. By executing the inverse Fourier transform of the power spectral density and applying the Wiener-Khinchin theorem, one may derive the autocorrelation function (PSD). Using this relationship, we can come up with the following expressions for the autocorrelation functions in the frequency domain:

$$\begin{aligned}\mathbf{r}_{\mathrm{pe}} &= \mathcal{F}_N^{-1}(\mathbf{p}_{\mathrm{pe}}) = \frac{1}{N}\mathbf{D}_N^H \mathbf{p}_{\mathrm{pe}}, \\ \mathbf{r}_{\mathrm{ap}} &= \mathcal{F}_{2N}^{-1}(\mathbf{p}_{\mathrm{ap}}) = \frac{1}{2N}\mathbf{D}_{2N}^H \mathbf{p}_{\mathrm{ap}},\end{aligned} \tag{6.8}$$

where $\mathbf{p}_{\mathrm{pe}}$ and $\mathbf{p}_{\mathrm{ap}}$ are the relevant N-tuple and $2N$-tuple PSDs. Substituting (6.8) into (6.6), we can represent the $\mathrm{ISL}_{\mathrm{pe}}$ and $\mathrm{ISL}_{\mathrm{ap}}$ in frequency domain as the following where N and 2N-tuple PSDs, respectively, are represented by $\mathbf{p}_{\mathrm{pe}}$ and $\mathbf{p}_{\mathrm{ap}}$. In the frequency domain, the $\mathrm{ISL}_{\mathrm{pe}}$ and $\mathrm{ISL}_{\mathrm{ap}}$ can be represented as the following by replacing (6.8) with (6.6).

$$\begin{aligned}
\mathrm{ISL}_{\mathrm{pe}} &= \frac{1}{N^2}\mathbf{p}_{\mathrm{pe}}^H \mathbf{D}_N \mathbf{D}_N^H \mathbf{p}_{\mathrm{pe}} - N^2 = \frac{1}{N}\left(\mathbf{p}_{\mathrm{pe}}^H \mathbf{p}_{\mathrm{pe}} - N^3\right), \\
\mathrm{ISL}_{\mathrm{ap}} &= \frac{1}{2}\left(\frac{1}{4N^2}\mathbf{p}_{\mathrm{ap}}^H \mathbf{D}_{2N} \mathbf{D}_{2N}^H \mathbf{p}_{\mathrm{ap}} - N^2\right) \\
&= \frac{1}{4N}\left(\mathbf{p}_{\mathrm{ap}}^H \mathbf{p}_{\mathrm{ap}} - 2N^3\right).
\end{aligned} \tag{6.9}$$

In (6.9), $\mathbf{D}_{\tilde{N}}\mathbf{D}_{\tilde{N}}^H = \tilde{N}\mathbf{I}_{\tilde{N}}$ where $\mathbf{I}_{\tilde{N}}$ is the $\tilde{N} \times \tilde{N}$ identity matrix and $\tilde{N} = N, 2N$. Generally, lowering the ISL metric results in reduced autocorrelation sidelobes. Consequently, we can describe our problem as

$$\begin{aligned}
\min \quad & \mathrm{ISL} \\
\text{s.t.} \quad & |x_n| = 1, \quad n = 0, ..., N-1.
\end{aligned} \tag{6.10}$$

Due to the similarity in form between the periodic and aperiodic ISL metrics in (6.9) , we may eliminate the constant terms and obtain the following common cost function:

$$J_{\mathrm{ISL}} = \frac{1}{2\tilde{N}}\mathbf{p}^H \mathbf{p}, \tag{6.11}$$

where $\mathbf{p} = \left[p_0, ..., p_{\tilde{N}-1}\right]^T$ and the length of the FFT is defined by $\tilde{N}$. Consequently, ZZ becomes the objective function for the periodic case when $\tilde{N} = N$ and for the aperiodic case when $\tilde{N} = 2N$.

6.1.3 Spectral Stopband Constraint

Since there are numerous users of the electromagnetic spectrum, it is frequently necessary to notch some frequency bands that are already in use or prohibited in order to reduce interference in spectrally dense places. Therefore, when designing such transmit waveforms, spectral stopbands must be considered. Taking the normalized frequency into account, the set of frequency stopbands $\Omega \subset [0, 1]$ is defined as

$$\Omega = \bigcup_{i=1}^{I} \left(f_{\mathrm{a}_i}, f_{\mathrm{b}_i}\right), \tag{6.12}$$

where I signifies the number of stopband intervals and $(f_{\mathrm{a}_i}, f_{\mathrm{b}_i})$ indicates a single stopband interval (start frequency, end frequency). The spectral stopband set can be described as follows, considering a discrete $\tilde{N}$-point frequency domain representation of the sequence.

$$\Omega_s = \bigcup_{i=1}^{I} \left[\lfloor \tilde{N} f_{\mathrm{a}_i} \rfloor, \lceil \tilde{N} f_{\mathrm{b}_i} \rceil\right] \subset \left[0, \tilde{N}\right], \tag{6.13}$$

where $\lceil \cdot \rceil$ and $\lfloor \cdot \rfloor$ respectively represent the ceiling and floor operations. From (6.12) and (6.13), we may deduce that suppressing the stopband Ω minimizes the spectral density in Ω_s, i.e., $\mathbf{p}(i), i \in \Omega_s$. With the following expression, we assign weights to PSD with regard to Ω_s, the spectral weighting vector. Let v be the weighting vector for the spectral bins defined by the expression below.

$$\begin{aligned} \mathbf{v} &= \left[v_0, ..., o_{\tilde{N}-1}\right]^T, \\ v_i &= \begin{cases} 1, & i \in \Omega_s \\ 0, & \text{otherwise} \end{cases} \end{aligned} \tag{6.14}$$

Because PSD takes on nonnegative values, the cost of spectral stopband suppression can be represented as follows.

$$J_{\mathrm{STOP}} = \|\mathbf{v} \circ \mathbf{p}\|^2 = \mathbf{p}^H \operatorname{Diag}(\mathbf{v})\mathbf{p}. \tag{6.15}$$

As a matter of fact, as the squared Euclidean norm of weighted PSD, the cost J_{STOP} represents the overall power in the spectral stopbands. Minimizing the criterion in (6.15) corresponds to reducing the spectral power in Ω.

6.1.4 Unified Objective Function

Our ultimate aim is to consolidate the requirements for autocorrelation and spectral stopband restrictions into a single objective function, after having shown their respective cost functions. The design challenge is regarded as a bi-objective (Pareto) optimization problem due to the need for minimizing both J_{ISL} and J_{STOP}. Consider the fact that eliminating autocorrelation sidelobes yields a flat spectrum, whereas stopband (notch) edge modulations in the spectrum cause autocorrelation sidelobes to oscillate. That's why it's important to achieve a compromise between spectral stopband reduction and suppression of the correlation sidelobe. As a result of this, we begin by linearizing each of the subproblems in order to transform the dual-objective optimization issue into a single-objective optimization problem. Then, we formulate the unified goal function J in terms of J_{ISL} and J_{STOP}, with scalarization parameter λ acting as a balancer.

$$\begin{aligned} J &= (1-\lambda)\, J_{\text{ISL}} + \lambda J_{\text{STOP}} \\ &= \frac{1-\lambda}{2\tilde{N}} \mathbf{p}^H \mathbf{p} + \lambda \mathbf{p}^H \operatorname{Diag}(\mathbf{v}) \mathbf{p} \\ &= \mathbf{p}^H \operatorname{Diag}(\mathbf{w}) \mathbf{p}, \end{aligned} \tag{6.16}$$

where $\mathbf{w} = \lambda \mathbf{v} + \frac{1-\lambda}{2\tilde{N}}$ denotes the weighting vector and $\lambda \in [0,1]$. Let $\mathbf{a}_i$ and $\mathbf{f}$ denote an arbitrary column vector and the $\tilde{N}$-point DFT of $\mathbf{x}$, respectively, with the following expressions

$$\begin{aligned} \mathbf{a}_i &= \left[1, e^{j\omega_i}, ..., e^{j\omega_i (N-1)}\right]^T, \ \omega_i = \frac{2\pi}{\tilde{N}} i, \ i = 0, ..., \tilde{N}-1, \\ \mathbf{f} &= \left[f_0, ..., f_{\tilde{N}-1}\right]^T = \left[\mathbf{a}_0^H \mathbf{x}, ..., \mathbf{a}_{\tilde{N}-1}^H \mathbf{x}\right]^T, \end{aligned} \tag{6.17}$$

The PSD can then be expressed using $\mathbf{x}$ as follows.

$$\mathbf{p} = \mathbf{f}^* \circ \mathbf{f} = \left[\mathbf{x}^H \mathbf{a}_0 \mathbf{a}_0^H \mathbf{x}, ..., \mathbf{x}^H \mathbf{a}_{\tilde{N}-1} \mathbf{a}_{\tilde{N}-1}^H \mathbf{x}\right]. \tag{6.18}$$

Using (6.17), the unified objective function (6.16) can be written more explicitly as

$$J = \sum_{i=0}^{\tilde{N}-1} w_i \left(\mathbf{x}^H \mathbf{a}_i \mathbf{a}_i^H \mathbf{x}\right)^2, \tag{6.19}$$

where $w_i = \lambda v_i + \frac{1-\lambda}{2\tilde{N}}$.

As previously indicated, our work is concerned with unimodular sequences.

Hence, we can formalize our sequence design problem as follows:

$$\begin{aligned} \min \quad & J = \sum_{i=0}^{\tilde{N}-1} w_i \left(\mathbf{x}^H \mathbf{a}_i \mathbf{a}_i^H \mathbf{x}\right)^2 \\ \text{s.t.} \quad & |x_n| = 1, \quad n = 0, ..., N-1 \end{aligned} \tag{6.20}$$

It is evident that the size of the complex sequence must equal one due to the unimodular property of sequence. As a result, it is possible to think of the sequence design problem as an optimization on the phase term of the sequence. Defining $\boldsymbol{\Theta} = \left[\theta_0, ..., \theta_{\tilde{N}-1}\right]^T$ as the phase vector and

$$\mathbf{x} = \left[e^{j\theta_0}, \ldots, e^{j\theta_{N-1}}\right]^T, \tag{6.21}$$

The minimization problem in (6.20) turns into an unconstrained optimization problem on $\boldsymbol{\Theta}$

$$\min \quad J\left(\boldsymbol{\Theta}\right) = \sum_{i=0}^{\tilde{N}-1} w_i \left(\mathbf{x}^H \mathbf{a}_i \mathbf{a}_i^H \mathbf{x}\right)^2. \tag{6.22}$$

6.2 Optimization: the Minimization Problem

Recent algorithms with monotonic decreasing properties include the Spectral-MISL [25], MISL [25], SMISLN [38] and FCGA [37]. In the Spectral-MISL, SMISLN and MISL algorithms, the majorizing function (Surrogate Function) is minimized as opposed to the original objective function, but in the FCGA approach, the original objective function is minimized by means of the conjugate gradient algorithm. In the FCGA algorithm, the search direction is the conjugate direction calculated using the Polak-Ribiere-Polyak-CGA (PRP-CGA) method [112], and the step size is properly predicted using the Taylor series expansion approach presented in [37]. Instead of nonlinear conjugate gradient approaches, we deduce the search direction using the Limited-Memory Broyden Fletcher Goldfarb Shanno (L-BFGS) method [110] in our work. The L-BFGS approach is appropriate for computers with limited memory and approximates the Broyden-Fletcher-Goldfarb-Shanno (BFGS) method, in which storing the Hessian matrix of size $N \times N$ required for calculating the search vector becomes prohibitively expensive for large scale applications. In L-BFGS, the inverse Hessian is implicitly estimated with the aid of the gradient and multiple auxiliary vector pairs that are updated at each iteration, and the estimated inverse Hessian is utilized to determine the search direction. For further information on the L-BFGS method, interested readers might refer to [110].

In the sections that follow, we will first determine the phase gradient and then the step size using the Taylor series expansion approach described in [37] Noteworthy is the fact that in our method, the unit step length is applied to search direction obtained by the L-BFGS recursion. This is owing to the fact that the L-BFGS recursion produces a optimally-scaled search direction (See Appendix-B). Due to the nonconvex and nonlinear structure of the cost function and the imprecise inverse Hessian estimation, the L-BFGS recursion seldom produces an ascent search direction. In this instance, as a corrective step, we carry on to the next iteration using the negative gradient vector (i.e., the descent direction) as the search direction and the step size determined by the Taylor series expansion approach. Later in this part, the algorithmic flow is presented.

6.2.1 Computation of Phase Gradient

Using the $\mathbf{a}_i$ matrix defined in (6.17) we introduce the $\mathbf{A}_i$ matrix defined as

$$\mathbf{A}_i = \mathbf{a}_i \mathbf{a}_i^H, \ \mathbf{A}_i\left(m+1, n+1\right) = a^i_{mn}, \ m, n = 0, ..., N-1. \tag{6.23}$$

By using (6.23), the gradient $\nabla_\theta J$ of (6.22) may be expressed as

$$\nabla_\Theta J = 2 \sum_{i=0}^{\tilde{N}-1} w_i \left(\mathbf{x}^H \mathbf{A}_i \mathbf{x}\right) \nabla_\Theta (\mathbf{x}^H \mathbf{A}_i \mathbf{x}). \tag{6.24}$$

For an explicit expression of (6.24), $\nabla_\Theta (\mathbf{x}^H \mathbf{A}_i \mathbf{x}^H)$ must first be deduced. Therefore, we begin by calculating the partial derivative of $J(\Theta)$ with regard to each phase component $\theta_l,\ l = 0, ..., N-1$ as follows:

$$\frac{\partial J}{\partial \theta_l} = 2 \sum_{i=0}^{\tilde{N}-1} w_i \left(\mathbf{x}^H \mathbf{A}_i \mathbf{x}\right) \frac{\partial \mathbf{x}^H \mathbf{A}_i \mathbf{x}}{\partial \theta_l}. \tag{6.25}$$

By further expanding $\mathbf{x}^H \mathbf{A}_i \mathbf{x}$ as

$$\mathbf{x}^H \mathbf{A}_i \mathbf{x} = \sum_{m=0}^{N-1} \sum_{n=0}^{N-1} a_{mn}^i e^{j(\theta_n - \theta_m)}, \tag{6.26}$$

the derivative of $\mathbf{x}^H \mathbf{A}_i \mathbf{x}$ with respect to θ_l can be written as

$$\frac{\partial \mathbf{x}^H \mathbf{A}_i \mathbf{x}}{\partial \theta_l} = jx_l \sum_{m=0}^{N-1} a_{ml}^i x_m^* - jx_l^* \sum_{n=0}^{N-1} a_{ln}^i x_n. \tag{6.27}$$

Because $\mathbf{A}_i = \mathbf{A}_i^H$, the equality $a_{ml}^i = (a_{lm}^i)^*$ holds. Hence, the derivative (6.27) can be expressed as

$$\frac{\partial \mathbf{x}^H \mathbf{A}_i \mathbf{x}}{\partial \theta_l} = 2\,\mathrm{Re}\left(-jx_l^* \sum_{n=0}^{N-1} a_{ln}^i x_n\right). \tag{6.28}$$

Then, we can convert (6.28) into a vector form and formulate the gradient $\nabla_\theta \left(\mathbf{x}^H \mathbf{A}_i \mathbf{x}\right)$ as follows

$$\nabla_\theta \left(\mathbf{x}^H \mathbf{A}_i \mathbf{x}\right) = 2\,\mathrm{Re}\left(-j\mathbf{x}^* \circ (\mathbf{A}_i \mathbf{x})\right). \tag{6.29}$$

Next, the gradient $\nabla_\Theta J$ can be rewritten by substituting (6.29) for (6.24) as the following

$$\begin{aligned}
\nabla_\Theta J =& 2 \sum_{i=0}^{\tilde{N}-1} w_i \left(\mathbf{x}^H \mathbf{A}_i \mathbf{x}\right) 2\,\mathrm{Re}\left(-j\mathbf{x}^* \circ (\mathbf{A}_i \mathbf{x})\right) \\
=& 4\,\mathrm{Re}\left(-j\mathbf{x}^* \circ \left(\sum_{i=0}^{\tilde{N}-1} \mathbf{a}_i w_i \left(\mathbf{x}^H \mathbf{a}_i \mathbf{a}_i^H \mathbf{x}\right) \mathbf{x}_i^H \mathbf{x}\right)\right) \\
=& 4\,\mathrm{Re}\left(-j\mathbf{x}^* \circ \left(\left[\mathbf{a}_0, ..., \mathbf{a}_{\tilde{N}-1}\right] \begin{bmatrix} w_0 |\mathbf{a}_0^H \mathbf{x}|^2 \mathbf{a}_0^H \mathbf{x} \\ \vdots \\ w_{\tilde{N}-1} |\mathbf{a}_{\tilde{N}-1}^H \mathbf{x}|^2 \mathbf{a}_{\tilde{N}-1}^H \mathbf{x} \end{bmatrix}\right)\right).
\end{aligned} \tag{6.30}$$

Defining $\mathbf{B} = \left[\mathbf{a}_0, ..., \mathbf{a}_{\tilde{N}-1}\right]$ as an auxiliary matrix, then we write the following expression

$$\begin{bmatrix} w_0|\mathbf{a}_0^H\mathbf{x}|^2\mathbf{a}_0^H\mathbf{x} \\ \vdots \\ w_{\tilde{N}-1}|\mathbf{a}_{\tilde{N}-1}^H\mathbf{x}|^2\mathbf{a}_{\tilde{N}-1}^H\mathbf{x} \end{bmatrix} = \begin{bmatrix} w_0 \\ \vdots \\ w_{\tilde{N}-1} \end{bmatrix} \circ \begin{bmatrix} |\mathbf{a}_0^H\mathbf{x}|^2 \\ \vdots \\ |\mathbf{a}_{\tilde{N}-1}^H\mathbf{x}|^2 \end{bmatrix} \circ \begin{bmatrix} \mathbf{a}_0^H\mathbf{x} \\ \vdots \\ \mathbf{a}_{\tilde{N}-1}^H\mathbf{x} \end{bmatrix} \\ = \mathbf{w} \circ |\mathbf{B}^H\mathbf{x}|^2 \circ \left(\mathbf{B}^H\mathbf{x}\right), \tag{6.31}$$

where $|.|^2$ is applied element-by-element to the vector. By substituting (6.31) into (6.30), $\nabla_\Theta J$ can be rewritten as

$$\nabla_\Theta J = 4\,\mathrm{Re}\left(-j\mathbf{x}^* \circ \left(\mathbf{B}\left(\mathbf{w} \circ |\mathbf{B}^H\mathbf{x}|^2 \circ \left(\mathbf{B}^H\mathbf{x}\right)\right)\right)\right). \tag{6.32}$$

It should be noted that $\mathbf{B}$ is an $\tilde{N} \times N$ matrix and $\mathbf{B}^H$ is identical to the first N columns of DFT matrix $\mathbf{D}_{\tilde{N}}$, i.e. $\mathbf{B}^H = \mathbf{D}_{:,1:N}$ (For a simpler notation, we drop the subscript of $\mathbf{D}_{\tilde{N}}$). By substituting $\mathbf{D}$ for $\mathbf{B}$, (6.32) can be reformulated as

$$\nabla_\Theta J = 4\tilde{N}\,\mathrm{Re}\left(-j\mathbf{x}^* \circ \left(\frac{1}{\tilde{N}}\mathbf{D}_{:,1:N}^H\left(\mathbf{w} \circ |\mathbf{D}_{:,1:N}\mathbf{x}|^2 \circ \left(\mathbf{D}_{:,1:N}\mathbf{x}\right)\right)\right)\right). \tag{6.33}$$

Therefore, the phase gradient in (6.33) can be derived through a number of (I)FFTs. Let

$$\mathbf{h} = \mathcal{F}_{\tilde{N}}^{-1}\left(\mathbf{w} \circ |\mathcal{F}_{\tilde{N}}(\mathbf{x})|^2 \circ \mathcal{F}_{\tilde{N}}(\mathbf{x})\right), \tag{6.34}$$

Finally, the simple formulation for the phase gradient (henceforth abbreviated $\mathbf{g}$) can be defined as follows:

$$\mathbf{g} = \nabla_\Theta J = 4\tilde{N}\,\mathrm{Re}(-j\mathbf{x}^* \circ \mathbf{h}_{1:N}), \tag{6.35}$$

where $\mathbf{h}_{1:N}$ is composed of the first N elements of $\mathbf{h}$.

6.2.2 Computation of Step Length

In optimization problems, conventional linear search methods are frequently utilized for calculating step length [110]. In the case of large-scale problems, however, these conventional techniques frequently result in excessive processing and iteration. For the phase optimization problem, Tang et. al. proposes a direct step length approximation based on Taylor series expansion as an alternative to the conventional linear search approach [37]. In our proposed LBSD approach, we often take a unit step, which saves us substantial computation and iteration costs. However, a precise step length computation is still required for the first m iterations and corrective steps in the event that the L-BFGS recursion returns an ascending search direction. The correction process will be detailed in detail in 6.2.3 later on. In this subsection, for the sake of thoroughness, we describe the steps of the Taylor series expansion method.

Assume that in the (kth) iteration, we have the vector $\mathbf{x}^k$ and the search direction is $\mathbf{d}^k = \left[d_0^k, ..., d_{N-1}^k\right]$. Then, the subsequent iteration and phase term is denoted as

$$\begin{aligned} \mathbf{x}^{k+1} &= \mathbf{x}^k \circ \left[e^{j\tilde{\mu}d_0^k}, ..., e^{j\tilde{\mu}d_{N-1}^k}\right], \\ \boldsymbol{\theta}^{k+1} &= \boldsymbol{\theta}^k + \tilde{\mu}\mathbf{d}^k, \end{aligned} \tag{6.36}$$

where $\tilde{\mu}$ represents the step size. As indicated in the following problem statement, the optimal solution for $\tilde{\mu}$ can be determined by solving a minimization problem with regard to $\tilde{\mu}$.

$$\min_{\tilde{\mu}>0} J(\tilde{\mu}) = \sum_{i=0}^{\tilde{N}-1} w_i \left(\left(\mathbf{x}^{k+1}\right)^H \mathbf{A}_i \mathbf{x}^{k+1}\right)^2. \tag{6.37}$$

Suppose $\mathbf{u}^{k+1}$ is defined as

$$\mathbf{u}^{k+1} = \left[\left(\mathbf{x}^{k+1}\right)^H \mathbf{A}_0 \mathbf{x}^{k+1}, ..., \left(\mathbf{x}^{k+1}\right)^H \mathbf{A}_{\tilde{N}-1} \mathbf{x}^{k+1}\right]^T. \tag{6.38}$$

Now, we can express the derivative of $J(\tilde{\mu})$ with respect to $\tilde{\mu}$ as

$$\begin{aligned}\frac{\partial J(\tilde{\mu})}{\partial \tilde{\mu}} =& \frac{\partial(\mathbf{w}^T(\mathbf{u}^{k+1} \circ \mathbf{u}^{k+1}))}{\partial \tilde{\mu}} \\ =& 2\mathbf{w}^T \left(\mathbf{u}^{k+1} \circ \frac{\partial \mathbf{u}^{k+1}}{\partial \tilde{\mu}} \right).\end{aligned} \tag{6.39}$$

To simplify (6.39) further, we first expand $(\mathbf{x}^{k+1})^H \mathbf{A}_i \mathbf{x}^{k+1}$ as

$$\left(\mathbf{x}^{k+1}\right)^H \mathbf{A}_i \mathbf{x}^{k+1} = \sum_{m=0}^{N-1} \sum_{n=0}^{N-1} a_{mn}^i \left(x_m^k\right)^* x_n^k e^{j\tilde{\mu}\left(d_n^k - d_m^k\right)}, \tag{6.40}$$

where d_n^k and x_n^k are $(n+1)$'th element of $\mathbf{d}^k$ and $\mathbf{x}^k$, respectively. Using the Taylor Series expansion, we can get a good approximation of the exponential term $e^{j\tilde{\mu}\left(d_n^k - d_m^k\right)}$ in (6.40). Keeping the expansion's first three terms, the approximation can be stated as

$$e^{j\tilde{\mu}\left(d_n^k - d_m^k\right)} \approx 1 + j\tilde{\mu}\left(d_n^k - d_m^k\right) - \frac{\tilde{\mu}^2}{2}\left(d_n^k - d_m^k\right)^2. \tag{6.41}$$

Then, we can rewrite $\left(\mathbf{x}^{k+1}\right)^H \mathbf{A}_i \mathbf{x}^{k+1}$ by substituting (6.41) into (6.40) as

$$\begin{aligned}\left(\mathbf{x}^{k+1}\right)^H \mathbf{A}_i \mathbf{x}^{k+1} = & \left(\mathbf{x}^k\right)^H \mathbf{A}_i \mathbf{x}^k - 2\tilde{\mu}\,\mathrm{Im}\left(\left(\mathbf{x}^k\right)^H \mathbf{A}_i \mathbf{x}_1^k\right) \\ & - \tilde{\mu}^2 \left(\mathrm{Re}\left(\left(\mathbf{x}^k\right)^H \mathbf{A}_i \mathbf{x}_2^k\right) - \left(\mathbf{x}_1^k\right)^H \mathbf{A}_i \mathbf{x}_1^k\right),\end{aligned} \tag{6.42}$$

where $\mathbf{x}_1^k = \mathbf{x}^k \circ \mathbf{d}^k$, $\mathbf{x}_2^k = \mathbf{x}^k \circ \mathbf{d}^k \circ \mathbf{d}^k$. Next we define

$$\begin{aligned}\mathbf{f}^k &= \mathcal{F}_{\tilde{N}}\left(\mathbf{x}^k\right) = \left[\mathbf{a}_0^H \mathbf{x}^k, ..., \mathbf{a}_{\tilde{N}-1}^H \mathbf{x}^k\right]^T, \\ \mathbf{f}_1^k &= \mathcal{F}_{\tilde{N}}\left(\mathbf{x}_1^k\right) = \left[\mathbf{a}_0^H \mathbf{x}_1^k, ..., \mathbf{a}_{\tilde{N}-1}^H \mathbf{x}_1^k\right]^T, \\ \mathbf{f}_2^k &= \mathcal{F}_{\tilde{N}}\left(\mathbf{x}_2^k\right) = \left[\mathbf{a}_0^H \mathbf{x}_2^k, ..., \mathbf{a}_{\tilde{N}-1}^H \mathbf{x}_2^k\right]^T,\end{aligned} \tag{6.43}$$

and

$$\begin{aligned}\mathbf{z}_1 &= \mathrm{Re}\left(\left(\mathbf{f}^k\right)^* \circ \mathbf{f}_2^k\right) - \left(\mathbf{f}_1^k\right)^* \circ \mathbf{f}_1^k, \\ \mathbf{z}_2 &= \mathrm{Im}\left(\left(\mathbf{f}^k\right)^* \circ \mathbf{f}_1^k\right).\end{aligned} \tag{6.44}$$

By using (6.42), (6.43), and (6.44), the (6.38) can be written much more simply as

$$\mathbf{u}^{k+1} = \left|\mathbf{f}^k\right|^2 - 2\tilde{\mu}\mathbf{z}_2 - \tilde{\mu}^2\mathbf{z}_1. \tag{6.45}$$

By finally substituting (6.45) into (6.39), we may get the derivative (6.39) expressed as follows:

$$\begin{aligned} \frac{\partial j(\tilde{\mu})}{\partial \tilde{\mu}} =& - 4\mathbf{w}^T \left(\left(|\mathbf{f}^k|^2 - 2\tilde{\mu}\mathbf{z}_2 - \tilde{\mu}^2\mathbf{z}_1 \right) \circ (\mathbf{z}_2 + \tilde{\mu}\mathbf{z}_1) \right) \\ =& - 4(c_1\tilde{\mu}^3 + c_2\tilde{\mu}^2 + c_3\tilde{\mu} + c_4), \end{aligned} \tag{6.46}$$

where

$$\begin{aligned} c_1 &= -\mathbf{w}^T(\mathbf{z}_1 \circ \mathbf{z}_1), \\ c_2 &= -3\mathbf{w}^T(\mathbf{z}_1 \circ \mathbf{z}_2), \\ c_3 &= -2\mathbf{w}^T(\mathbf{z}_2 \circ \mathbf{z}_2) + \mathbf{w}^T \left(|\mathbf{f}^k|^2 \circ \mathbf{z}_1 \right), \\ c_4 &= \mathbf{w}^T \left(|\mathbf{f}^k|^2 \circ \mathbf{z}_2 \right). \end{aligned} \tag{6.47}$$

By forcing the derivative to *zero* i.e., $\frac{\partial J(\tilde{\mu})}{\partial \tilde{\mu}} = 0$, the following cubic equation is obtained:

$$c_1\tilde{\mu}^3 + c_2\tilde{\mu}^2 + c_1\tilde{\mu} + c_4 = 0. \tag{6.48}$$

According to the fundamental theorem of algebra, a cubic polynomial must have at least one real root among its three roots. Solving (6.48) enables us to obtain an approximation of a viable step length. Providing that we have a descent search direction, there is at least one positive real root. Then, we can select the real root as the smallest positive value that is larger than zero but less than all other positive values.

6.2.3 L-BFGS based Algorithm Definition

Now that we've established how the phase gradient and the step size were derived, we can use the L-BFGS method to solve the unconstrained minimization problem (6.22). We use a two-loop recursion scheme based on L-BFGS to determine the

Table 6.1: Computational cost of Algorithm 5 (The multiplications and additions for each line are counted)

Step	Multiplication	Addition
4	$N + \tilde{N}\log\tilde{N}$	$\tilde{N}\log\tilde{N}$
5	$2N + \tilde{N}\log\tilde{N}$	$\tilde{N}\log\tilde{N}$
6	$2\tilde{N}$	$\tilde{N}$
7	$\tilde{N}$	0
8	$10\tilde{N}$	$5\tilde{N}$
15	$\tilde{N}$	0
16	$\tilde{N}\log\tilde{N}$	$\tilde{N}\log\tilde{N}$
17	$3\tilde{N} + \tilde{N}\log\tilde{N}$	$\tilde{N}\log\tilde{N}$
18	N	0
19	0	N
20	0	N
21	N	N
23-26	$2Nm$	$2Nm$
27	$2N$	$2N$
28	N	0
29-32	$2Nm$	$2Nm$
Total	$8N + 17\tilde{N}+$ $4Nm + 4\tilde{N}\log\tilde{N}$	$5N + 6\tilde{N}+$ $4Nm + 4\tilde{N}\log\tilde{N}$

search direction. Appendix-B provides a quick overview of the L-BFGS two-loop recursion in place of a comprehensive analysis of the L-BFGS optimization approach.

As illustrated in Appendix-B, the L-BFGS recursion always uses the most recent m pairs of $\{\mathbf{s}^i, \mathbf{y}^i\}, i = k, k-1, \ldots, k-m$ vectors to determine the current $\tilde{\mathbf{d}}^{k+1}$ search direction. Due to the absence of these $\{\mathbf{s}^i, \mathbf{y}^i\}, i = -1, -2, \ldots, -m$ vector pairs at the outset, we simply assign them the value *zero* before to starting the LBSD procedure. Following this, in the first m iterations, we calculate and take the step length $\tilde{\mu}$. After m iterations, we switch to taking unit steps.

However, because of the inaccurate inverse Hessian matrix approximation in L-

BFGS recursion, $\tilde{\mathbf{d}}^k$ is not always a descent direction, i.e.

$$\left(\mathbf{g}^{k+1}\right)^T \tilde{\mathbf{d}}^{k+1} < 0, \tag{6.49}$$

does not hold. To ensure the convergence of L-BFGS updates, we use the modified search direction rule shown below.

$$\mathbf{d}^{k+1} = \begin{cases} \tilde{\mathbf{d}}^{k+1}, & \left(\mathbf{g}^{k+1}\right)^T \tilde{\mathbf{d}}^{k+1} < 0 \\ -\mathbf{g}^{k+1}, & \left(\mathbf{g}^{k+1}\right)^T \tilde{\mathbf{d}}^{k+1} \geq 0 \end{cases}, \tag{6.50}$$

and the step length rule

$$\mu^k = \begin{cases} 1\ , & \left(\mathbf{g}^{k+1}\right)^T \tilde{\mathbf{d}}^{k+1} < 0 \\ \tilde{\mu}\ , & \left(\mathbf{g}^{k+1}\right)^T \tilde{\mathbf{d}}^{k+1} \geq 0 \end{cases}. \tag{6.51}$$

According to (6.50) and (6.51) we know that the $\tilde{\mathbf{d}}^{k+1}$ is selected as the search direction and the unit step is applied when the prospective search direction $\tilde{\mathbf{d}}^{k+1}$ (derived from L-BFGS recursion) is descendent (i.e., $\left(\mathbf{g}^{k+1}\right)^T \tilde{\mathbf{d}}^{k+1} < 0$). If, on the other hand, $\tilde{\mathbf{d}}^{k+1}$ is an ascent direction (i.e., $\left(\mathbf{g}^{k+1}\right)^T \tilde{\mathbf{d}}^{k+1} \geq 0$), the negative gradient is chosen as the searching direction, and the step length is calculated using the Taylor series approximation approach. This rule ensures convergence and satisfies the descending direction at all times. Using the above derivations, Algorithm 5 describes the L-BFGS based sequence design (LBSD) technique that has been developed.

Observed from Algorithm 5, the proposed LBSD algorithm requires just (I)FFT computations, Hadamard products, and fundamental vector operations for the L-BFGS recursion. To determine the computational complexity of the proposed algorithm, the total number of arithmetic operations in Algorithm 5 are counted. Table-1 displays the number of multiplications and additions in each step of Algorithm 5 (excluding stages with no additions or multiplications). According to Table-1, the total number of multiplications and additions is $13N+23\tilde{N}+8Nm+8\tilde{N}\log\tilde{N}$, which includes the infrequently used routine for calculating the step length. Due to the fact that m is a small number, such as $(3 \leq m \leq 20)$, it has no major impact on the computational complexity. As N becomes larger, the total number of multiplications and additions approaches $8\tilde{N}\log\tilde{N}$; consequently, the computational complexity per iteration can be described as $\mathcal{O}(\tilde{N}\log\tilde{N})$.

In comparison to contemporary algorithms such as Accelerated-MISL, CAN, and FCGA the proposed LBSD method performs more arithmetic operations every iteration. The cost of arithmetic operations per iteration for the CAN, Accelerated-MISL, FISL, Spectral MISL ,FCGA, and SMISLN are $8N\log 2N$, $15\tilde{N}+8\tilde{N}\log\tilde{N}$, $12N+8N\log 2N$, $15\tilde{N}+8\tilde{N}\log\tilde{N}$, $33\tilde{N}+8\tilde{N}\log\tilde{N}$, $24\tilde{N}+4\tilde{N}\log\tilde{N}$, respectively. However, a greater computation per iteration does not necessarily result in slower convergence. Despite having a little larger computation per iteration than the state-of-the-art FCGA method, the proposed LBSD algorithm outperforms all of existing contrast algorithms in terms of efficiency. In addition, these computation per iteration statistics are based on the worst-case scenario in which all algorithmic steps are run. Due to the L-BFGS recursion, the LBSD algorithm does not require the additional computation for the step length in the majority of iterations (i.e., unit step length is chosen mostly), resulting in a significant reduction in runtime per iteration. The results of computational simulations illustrating the relative performance metrics of several contrast algorithms will be presented in the next section.

Algorithm 5 The L-BFGS Based Sequence Design (LBSD)

Initialization: Set $k = 0,\ \lambda,\ \mathbf{w},\ N,\ \tilde{N},\ \mathbf{x}^0,\ \mathbf{f}^0 = \mathcal{F}_{\tilde{N}}\left(\mathbf{x}^0\right),\ \mathbf{g}^0 = \nabla_\theta J\left(\mathbf{x}^0\right),\ \mathbf{d}^0 = -\mathbf{g}^0,\ m,\ \epsilon$

Repeat

if $k < m$ **or** $ResetDirection = 1$ **then**

  $\mathbf{f}_1^k = \mathcal{F}_{\tilde{N}}\left(\mathbf{x}^k \circ \mathbf{d}^k\right)$

  $\mathbf{f}_2^k = \mathcal{F}_{\tilde{N}}\left(\mathbf{x}^k \circ \mathbf{d}^k \circ \mathbf{d}^k\right)$

  $\mathbf{z}_1 = Re\left(\left(\mathbf{f}^k\right)^* \circ \mathbf{f}_2^k\right) - \left(\mathbf{f}_1^k\right)^* \circ \mathbf{f}_1^k$

  $\mathbf{z}_2 = Im\left(\left(\mathbf{f}^k\right)^* \circ \mathbf{f}_1^k\right)$

  Compute the coefficients c_1, c_2, c_3, c_4 according to (6.47)

  Solve the cubic equation (6.48) and compute $\tilde{\mu}$.

  $\mu^k = \tilde{\mu}$.

  $ResetDirection = 0$

else

  $\mu^k = 1$

end if

$\mathbf{x}^{k+1} = \mathbf{x}^k \circ e^{j\mu^k \mathbf{d}^k}$

$\mathbf{f}^{k+1} = \mathcal{F}_{\tilde{N}}\left(\mathbf{x}^{k+1}\right)$

$\mathbf{h} = \mathcal{F}_{\tilde{N}}^{-1}\left(\mathbf{w} \circ \left|\mathbf{f}^{k+1}\right|^2 \circ \mathbf{f}^{k+1}\right)$

$\mathbf{g}^{k+1} = 4\tilde{N} Re\left(-j\left(\mathbf{x}^{k+1}\right)^* \circ \mathbf{h}_{1:N}\right)$

$\mathbf{y}^k = \mathbf{g}^{k+1} - \mathbf{g}^k$

$\mathbf{s}^k = \mathbf{x}^{k+1} - \mathbf{x}^k = \mu^k \mathbf{d}^k$

$\rho^k = \frac{1}{\left(\mathbf{y}^k\right)^T \mathbf{s}^k}$

$\mathbf{q} = \mathbf{g}^{k+1}$

for $p = k-1, \cdots, k-m$ **do** {L-BFGS}

  $\alpha_p = \rho^p \left(\mathbf{s}^p\right)^T \mathbf{q}$

  $\mathbf{q} = \mathbf{q} - \alpha_p \mathbf{y}^p$

end for

$\boldsymbol{\gamma}^k = \frac{\left(\mathbf{s}^k\right)^T \mathbf{y}^k}{\left(\mathbf{y}^k\right)^T \mathbf{y}^k}$

$\mathbf{b} = \mathrm{Diag}\left(\boldsymbol{\gamma}^k\right)\mathbf{q}$

for $p = k-m, k-m+1, \cdots, k-1$ **do**

  $\beta = \rho^p \left(\mathbf{y}^p\right)^T \mathbf{r}$

  $\mathbf{b} = \mathbf{b} + \mathbf{s}^p\left(\alpha_p - \beta\right)$

end for

$\tilde{\mathbf{d}} = -\mathbf{b}$

if $\left(\mathbf{g}^{k+1}\right)^T \tilde{\mathbf{d}} < 0$ **then**

  $\mathbf{d}^{k+1} = \tilde{\mathbf{d}}$

else

  $\mathbf{d}^{k+1} = -\mathbf{g}^{k+1}$

  $ResetDirection = 1$

end if

$k = k + 1$

Until convergence i.e., $\left\|\mathbf{x}^{k+1} - \mathbf{x}^k\right\| \le \epsilon$

Table 6.2: The list of experiments

Experiment	**Stopping Criteria ϵ**	**Sequence Length N**	$\tilde{N}$	λ	**Algorithms**
Periodic Sequence Design	$\epsilon = 10^{-14}$	$N = 128$	$\tilde{N} = N$	$\lambda = 0$	PECAN [28], FCGA [37], LBSD
Aperiodic Sequence Design	$\epsilon = 10^{-3}$	$N = 32, ..., 8192$	$\tilde{N} = 2N$	$\lambda = 0$	CAN [24], ACC-MISL [25], FISL [31], FCGA [37], LBSD
Sequence Design with Spectral Stopbands (SFW)	$\epsilon = 10^{-3}$	$N = 128, 8192$	$\tilde{N} = 2N$	$\lambda = 0.9$ ($\lambda = 10^4$ for Spectral MISL)	SCAN [13], Spectral MISL [25], FCGA [37], SMISLN-acc [38], LBSD

6.3 Numerical Simulations

Numerical examples based on computer simulations are presented to show the potential of the proposed LBSD algorithm in different settings and to compare its performance to that of other existing algorithms. All simulations are conducted on a computer with a 2.60 GHz Intel i7-5600U processor and 16 GB of RAM. The software scripts are developed using MathWorks® Matlab 2019b. In these simulations, all algorithms are initialized with the identical unimodular sequence, i.e. $x^0 = \left\{e^{j2\pi\theta_n}\right\}_{n=0}^{N-1}$, where $\{\theta_n\}_{n=0}^{N-1}$ are independent random variables uniformly distributed in [0,1]. The stopping condition for simulations is determined by the l_2-norm ($\left\|\mathbf{x}^{k+1} - \mathbf{x}^k\right\| < \epsilon$) such that all algorithms are terminated when the Euclidean distance of sequences between subsequent iterations is smaller than a set threshold ϵ.

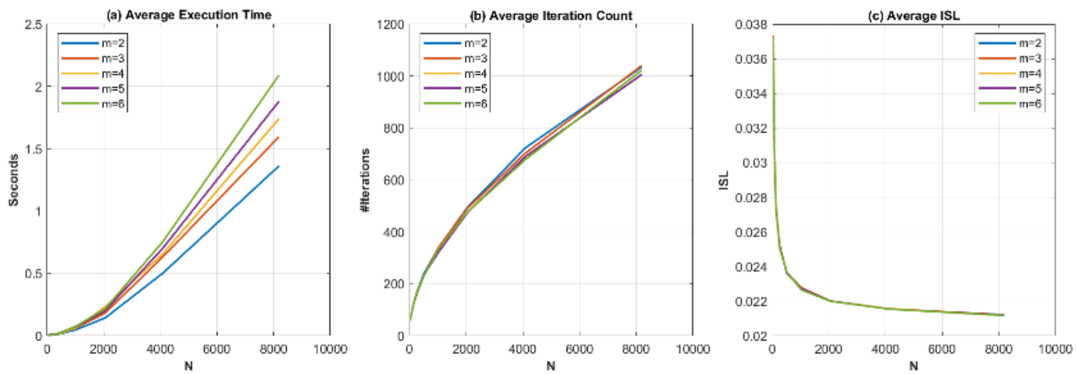

Figure 6.1: The performance figures based on history parameter m: (a) Avg. execution time, (b) Iteration cnt. and (c) ISL versus N.

Based on empirical findings, we prefer to set the L-BFGS recursion history parameter for the proposed LBSD method to $m = 2$. The average metrics of 1000

Table 6.3: The list of algorithms

Algorithm	Synthesis Goal	Methodology	Objective Function	Parameters	Complexity per Iteration
PECAN [28]	Periodic	Alternating Minimization	ISL	-	$\mathcal{O}(4N \log N)$
CAN [24]	Aperiodic	Alternating Minimization	ISL	-	$\mathcal{O}(8N \log 2N)$
FISL [31]	Aperiodic	Alternating Minimization	ISL	-	$\mathcal{O}(8N \log 2N)$
ACC-MISL [25]	Periodic\Aperiodic	Majorization-Minimization	ISL	-	$\mathcal{O}(8\tilde{N} \log \tilde{N})$
FCGA [37]	Periodic\Aperiodic\Stopband	Conjugate Gradient	$(\lambda)SC + (1-\lambda)ISL$	$\lambda \in [0,1]$	$\mathcal{O}(8\tilde{N} log \tilde{N})$
SCAN [13]	Aperiodic\Stopband	Alternating Minimization	$(\lambda)SC + (1-\lambda)ISL$	$\lambda \in [0,1]$	$\mathcal{O}(8N \log 2N)$
Spectral-MISL [25]	Periodic\Aperiodic\Stopband	Majorization-Minimization	$(\lambda)SC + ISL$	$\lambda \geq 0$	$\mathcal{O}(8\tilde{N} \log \tilde{N})$
SMISLN-acc [38]	Periodic\Aperiodic\Stopband	Majorization-Minimization	$(\lambda)SC + (1-\lambda)ISL$	$\lambda \in [0,1]$	$\mathcal{O}(4\tilde{N} log \tilde{N})$
LBSD	Periodic\Aperiodic\Stopband	L-BFGS (Quasi Newton)	$(\lambda)SC + (1-\lambda)ISL$	$\lambda \in [0,1],\ m : m \in \mathbb{Z}^+, m \geq 2$	$\mathcal{O}(8\tilde{N} \log \tilde{N})$

Monte Carlo simulations for aperiodic sequence synthesis are provided in Figure 6.1 for different values of the parameter m. Figure 6.1(a),(b) and (c) show the execution time, iteration count, and ISL values with respect to sequence length, respectively. The results demonstrate that, for big sequences ($N > 4000$), a lower value of parameter m can be traded off for a longer execution time, although all simulations roughly approach the same average iteration count and ISL for each m choice. If a marginally better ISL metric is desired, $m = 3$ can be chosen even though it does not offer a significant improvement.

Depending on the design objective (ISL or Stopband minimization), we compare the output sequence quality in the experiments in both the temporal and spectral domains. To evaluate the quality of sidelobes in temporal domain, we refer to the generally employed performance metrics such as integrated sidelobe level (ISL)(6.4), peak sidelobe level (PSL), and Merit Factor (MF). The PSL is as follows:

$$\text{PSL} = \max_{i \neq 0} \left| \frac{r_i}{r_0} \right|^2, \tag{6.52}$$

while MF is defined as

$$\text{MF} = \frac{|r_0|^2}{\sum_{i=1}^{\tilde{N}-1} |r_i|^2} = \frac{N^2}{\text{ISL}}. \tag{6.53}$$

As can be seen, MF is closely related and inversely proportional to ISL, and therefore, a bigger MF indicates a more effective suppression of correlation sidelobes.

For simulations of sparse frequency sequence design, we additionally evaluate the resulting sequences' quality based on their spectral features. To evaluate the quality of the sequences in the spectral domain, the normalized spectral power is first calculated. Assuming $\mathbf{f}$ represents the $\tilde{N}$-point DFT of $\mathbf{x}$ as given in (6.17), we normalize the spectral power $\mathbf{p}$ so that the average value of $|f_i|^2$ in the passband is unity. The normalized spectral density can be computed using the formula:

$$\hat{\mathbf{p}} = \left|\hat{f}_i\right|^2 = (\tilde{N} - N_s)\frac{|f_i|^2}{\sum_{k\in\Omega_s}|f_k|^2} \tag{6.54}$$

where N_s represents the number of frequency bins within the stopband. Then, to evaluate the degree of suppression in spectral stopbands, we utilize normalized stopband power (NASP) and peak stopband power (PSP), which are defined as follows:

$$\mathrm{PSP} = \max_{i\in\Omega_s}\left|\hat{f}_i\right|^2, \tag{6.55}$$

$$\mathrm{NASP} = \frac{1}{N_s}\sum_{i\in\Omega_s}\left|\hat{f}_i\right|^2. \tag{6.56}$$

After defining the performance parameters, we conduct three distinct experiments to numerically assess the LBSD algorithm's performance and compare the outcomes with those of other algorithms. The periodic ($\tilde{N} = N$) and aperiodic ($\tilde{N} = 2N$) sequence design problems are covered in the first and second examples, respectively, with the sole objective being to minimize the ISL metric. Next, in the third example, we take into account the spectral stopband suppression as well as the autocorrelation sidelobes suppression. For the synthesis of aperiodic and periodic sequences, we set the Pareto parameter in (6.16) to $\lambda = 0$, and for the synthesis of sparse frequency sequences, we set $\lambda = 0.9$. We note that when $\lambda > 0.5$, spectral stopband suppression is prioritized, while $\lambda < 0.5$ emphasizes correlation sidelobe suppression. The settings and parameters selected for the three experiments are shown in Table 6.2 and in Table 6.3, all of the algorithms included in these experiments are listed together with their properties, such as their synthesis type, methodology, objective function, input parameters, and computational complexity.

Table 6.4: Periodic sequence synthesis trials: Numerical results for ($N = 128$)

Algorithm	ISL $\leq 10^{-24}$	ISL $\leq 10^{-20}$	$\mathrm{ISL}_{\min}$	PSL $\leq -300dB$	PSL $\leq -250dB$	$\mathrm{PSL}_{\min}$	$t_{run} \leq 0.1sec$	$t_{run} \leq 1sec$
PeCAN [28]	0%	56.9%	2.3×10^{-23}	0%	57.7%	-285.4	0%	13%
FCGA [37]	24.8%	58.2%	8.12×10^{-26}	11%	58.3%	-318.1	50%	99.4%
LBSD	41.6%	59.8%	4.02×10^{-26}	27%	59.6%	-319.1	92%	100%

6.3.1 Case I: Periodic Sequence Design

The periodic unimodular sequence design ($\tilde{N} = N$ and $\lambda = 0$) experiment is performed using the well-known PeCAN [28], the state-of-art FCGA [37], and the proposed LBSD method. For PeCAN and FCGA, the suggested stopping criteria are $10-10$ [28] and $10-14$ [37], respectively. To provide for a fair comparison, all of the algorithms in this experiment use the same halting condition ($\epsilon = 10^{-14}$). We run 1000 Monte Carlo trials for each algorithm, starting with separate random unimodular sequences of length $N = 128$, and then record the normalized autocorrelations of the sequences to assess performance.

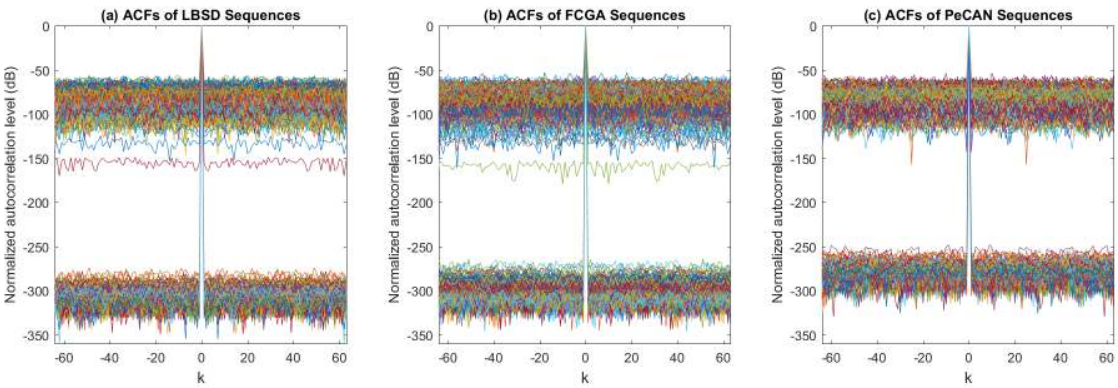

Figure 6.2: *Periodic Sequence Design Trials* - Autocorrelation Functions (a) Proposed LBSD sequences.(b) FCGA sequences. (c) PeCAN sequences.

In Figure 6.2, the autocorrelation functions of output sequences acquired by executing contrast algorithms are depicted, and the correlation sidelobes are observed to be clustered around two distinct sidelobe zones in each plot. Due to the nonconvex structure of the objective function, this conclusion is mostly explained by the possibility that these algorithms may stagnate at a local minima rather than

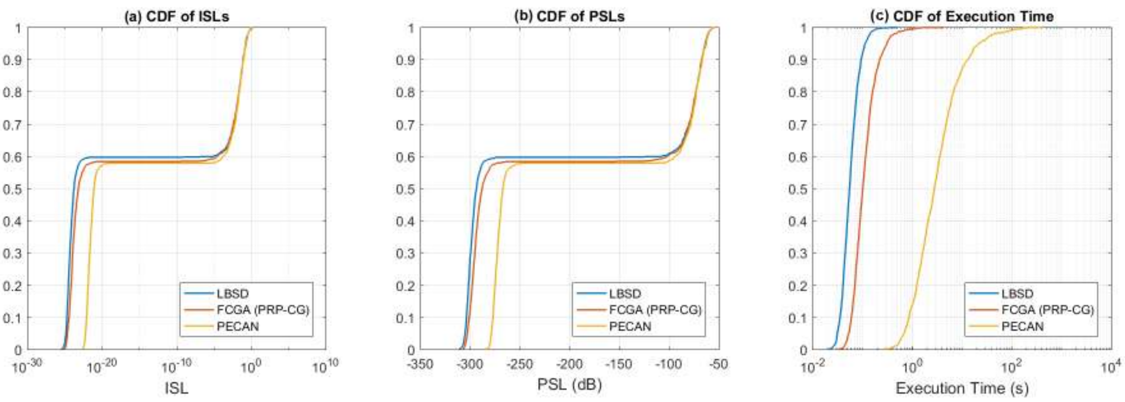

Figure 6.3: *Periodic Sequence Design Trials* - The cumulative distribution functions of metrics: (a) ISL CDF. (b) PSL CDF (c) Execution Time CDF.

the global solution. As demonstrated in these autocorrelation plots, the sidelobe level around $-300dB$ can be considered the global minimum; nevertheless, these techniques may not always converge to the global minimum. In this regard, we believe that a statistical study of the distribution of ISL, PSL, and execution time parameters over a number of runs is more relevant than a single-run comparison.

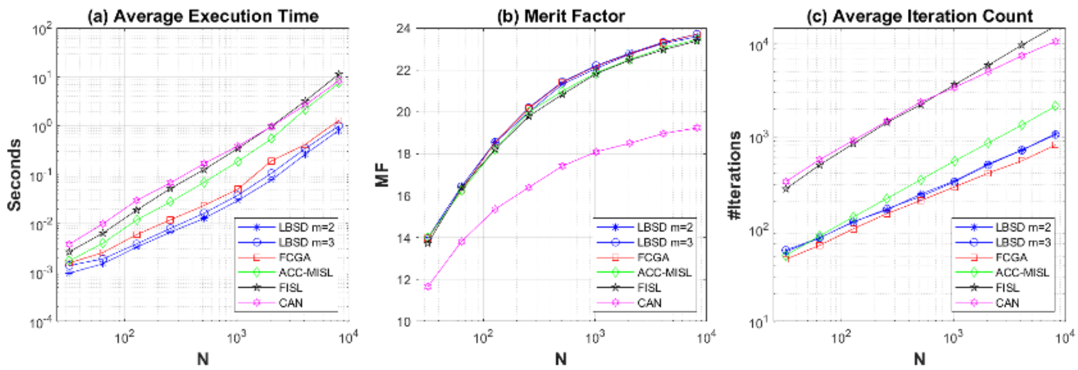

Figure 6.4: *Aperiodic Sequence Design Trials* - Average Performance Metrics (a) Avg. running time. (b) Avg. merit factor. (c) Avg. iteration count.

Figure 6.3 depicts the cumulative distribution functions of the recorded ISL, PSL, and execution time metrics for each method (a-c). Inferred from Figure 6.3(a) and (b), the distributions of ISL and PSL metrics for FCGA and the proposed LBSD algorithm are superior to those of PeCAN. In these simulations, the PECAN is inca-

Table 6.5: *Aperiodic Sequence Design Trials* - The average execution time, MF and iteration count values versus N ($N = 2^5 \dots 2^{13}$)

	$N=32$			$N=64$			$N=128$			$N=256$			$N=512$		
Algorithm	t(s)	MF	N_i	t(s)	MF	N_i	t(s)	MF	N_i	t(s)	MF	N_i	t(s)	MF	N_i
CAN [24]	0.0038	5.83	327	0.01	6.90	564	0.02	7.67	913	0.06	8.19	1471	0.16	8.70	2371
ACC-MISL [25]	0.0017	7.00	52	0.004	8.11	84	0.01	9.10	136	0.02	9.99	214	0.07	10.49	342
FCGA [37]	0.0016	6.98	47	0.002	8.12	67	0.006	9.27	101	0.012	10.08	147	0.02	10.69	204
FISL [31]	0.0027	6.86	273	0.006	8.19	494	0.018	9.10	841	0.05	9.89	1426	0.12	10.41	2221
LBSD ($m=2$)	0.0010	6.99	57	0.0015	8.21	80	0.0033	9.26	120	0.0067	9.99	161	0.012	10.65	240
LBSD ($m=3$)	0.0014	6.98	59	0.0019	8.22	81	0.0039	9.28	119	0.008	10.10	166	0.016	10.71	225

	$N=1024$			$N=2048$			$N=4096$			$N=8192$		
Algorithm	t(s)	MF	N_i	t(s)	MF	N_i	t(s)	MF	N_i	t(s)	MF	N_i
CAN [24]	0.38	9.04	3410	0.97	9.25	5041	2.66	9.48	7502	8.37	9.61	10734
ACC-MISL [25]	0.18	10.92	546	0.54	11.25	854	2.18	11.52	1338	7.47	11.72	2140
FCGA [37]	0.05	11.08	285	0.19	11.38	403	0.41	11.64	549	1.29	11.84	814
FISL [31]	0.34	10.90	3647	0.98	11.23	5919	3.21	11.47	9787	11.39	11.69	15747
LBSD ($m=2$)	0.02	11.03	332	0.07	11.37	506	0.26	11.62	718	0.81	11.79	1076
LBSD ($m=3$)	0.038	11.10	325	0.10	11.39	494	0.34	11.66	714	0.99	11.85	1052

pable of generating sequences with an ISL value of less than 10^{-24} and a PSL value of less than $-285.4dB$. As both the proposed LBSD and FCGA algorithms utilize the same objective function, their ISL and PSL metrics are equivalent. In spite of this, LBSD outperforms FCGA in terms of ISL, PSL, and execution time measures. We observe that 41.6% of the ISL distribution for the proposed LBSD is less than 10^{-24}, whereas 24.8% of the ISL distribution for the FCGA falls within this range. In contrast, 27% percent of the PSL distribution for the planned LBSD is less than $-300dB$, compared to 11% percent for the FCGA. In addition, the suggested LBSD approach obtains the lowest ISL and PSL values: 4.02×10^{-26} and $-319.1dB$, respectively. As shown in Figure 6.3(c), the new LBSD algorithm also surpasses the previous contrast methods in terms of convergence speed, demonstrating that the proposed LBSD algorithm is significantly faster and more computationally economical. 92% of LBSD trials have a runtime of less than 0.1 seconds, whereas 50% of FCGA trials have a runtime of less than 0.1 seconds. In Table 6.4, the numerical results of periodic sequence synthesis trials for the PECAN, FCGA, and proposed LBSD are summarized. Table 6.4 demonstrates that the proposed LBSD is superior to the FCGA and PECAN in terms of execution time and ISL, PSL metrics. According to Table 6.4, the proposed LBSD obtains the lowest ISL and PSL values, and a greater proportion of successful runs reach the specified ISL (e.g., 10^{-20} and 10^{-24}) and PSL (e.g., $-200dB$ and $-300dB$) values for the proposed LBSD than for others. For the periodic sequence design case, the suggested LBSD algorithm converges faster than the FCGA and PECAN.

6.3.2 Case II: Aperiodic Sequence Design

We compare the performance of the traditional CAN [24], Accelerated MISL [25], FCGA [37], FISL [31], and the proposed LBSD method in the aperiodic unimodular sequence design experiment (i.e., $\tilde{N} = 2N$ and $\lambda = 0$). In contrast to the previous experiment, we execute the algorithms for different sequence lengths, such as $N = 32, \ldots, 8192$, and set the halting condition to $\epsilon = 10^{-3}$ as in [37] to ensure that all algorithms are compared on an fair basis. In addition to $m = 2$, we also show how well LBSD performs when $m = 3$ is used as a recursion history parameter.

We execute all algorithms 300 times for each sequence length, and then we average the resulting values for the MF, execution time, and iteration count metrics. In Figure 6.4(a-c), the performance values for the contrast algorithms are presented in relation to sequence lengths, and Table 6.5 summarizes the numerical results.

According to Table 6.5 and Figure 6.4(b), all algorithms, with the exception of the CAN algorithm, achieve comparable average MF values for all sequence lengths. Table 6.5 shows the average values for execution time, MF, and iteration count versus sequence length. The FCGA algorithm has the fewest iterations across the contrast algorithms when comparing the average number of iterations in Figure 6.4(c) and Table 6.5. However, the runtime of FCGA is a little bit longer than that of the proposed LBSD algorithm because of the cost of step length calculation. Although the LBSD algorithm needs more iterations than FCGA, the cost of LBDS iteration is lower than FCGA because L-BFGS recursion eliminates the requirement for most additional step length calculations. Comparatively to the CAN method, the FISL algorithm yields acceptable MF results. But its speed of convergence is slower than that of both the FCGA and the proposed LBSD ($m = 2$ and $m = 3$).

The proposed LBSD with parameter choice ($m = 3$) gives slightly better MF values than LBSD with ($m = 2$), according to Table 6.5, however the speed improvement for LBSD ($m = 2$) is significantly bigger. In conclusion, the suggested LBSD algorithm achieves a merit factor that is at least as good as or better than other state-of-the-art algorithms like FCGA and FISL while outperforming other aperiodic sequence synthesis algorithms in terms of speed. Additionally, in these aperiodic sequence design trials, the suggested LBSD is successful in reaching sub-second convergence speed for all provided sequence lengths.

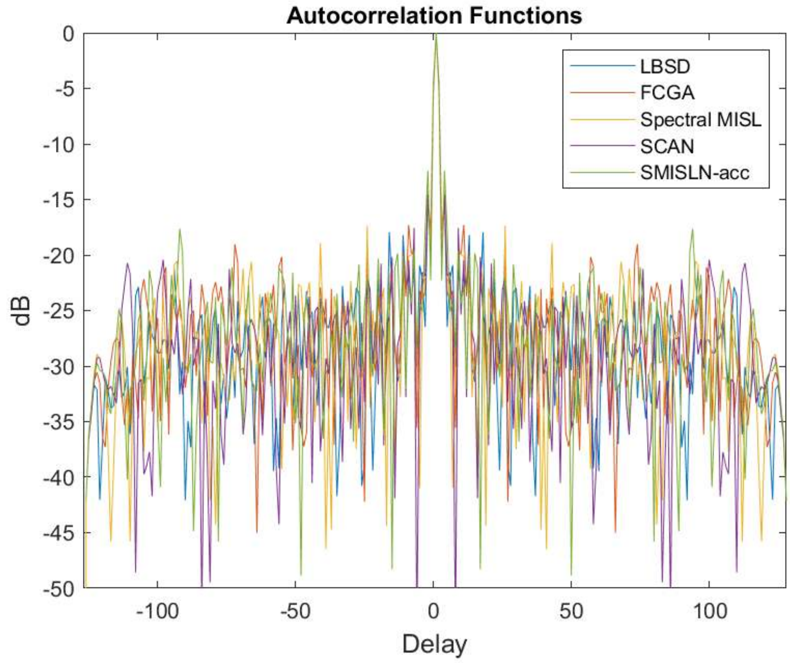

Figure 6.5: *Sparse Frequency Waveform Design Trials* - The normalized ACFs of the sequences ($N = 128$).

6.3.3 Case III: Sparse Frequency Waveform Design

The sparse frequency waveform design problem is the subject of our final experiment, in which we examine and contrast the performance metrics of the conventional SCAN [13], Spectral MISL [25], FCGA [37], SMISLN-acc [38] and the proposed LBSD algorithm. With the normalized spectral stopband $\Omega = [0.04, 0.21] \cup [0.23, 0.25] \cup [0.28, 0.37] \cup [0.39, 0.49] \cup [0.52, 0.56]$ Hz, which combines a variety of non-symmetrical narrow and wide frequency bands, we consider the synthesis of unimodular sequences with lengths $N = 128$ and $N = 8192$. The Pareto weighting parameter for the SCAN, FCGA, SMISLN-ACC, and proposed LBSD algorithms is chosen to be $\lambda = 0.9$, while the Spectral MISL as suggested in [25] is chosen to be $\lambda = 10^4$. The halting criterion for all algorithms is set at $\epsilon = 10^{-3}$.

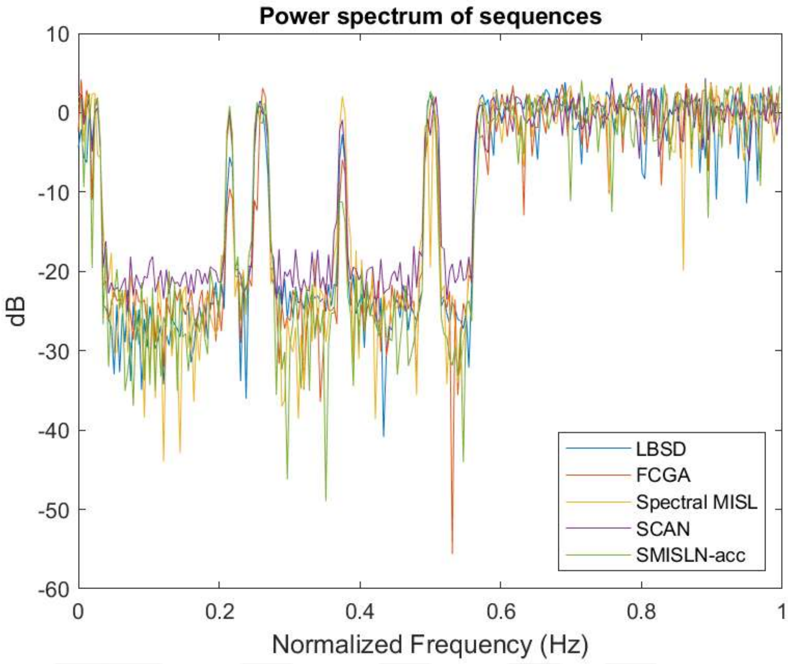

Figure 6.6: *Sparse Frequency Waveform Design Trials* - The normalized PSD of the sequences ($N = 128$).

As previously mentioned, comparing or evaluating the performance of the algorithms based on a single run might be deceptive. As a result, we do 300 Monte Carlo trials for each method to give the results a probabilistic interpretation and eliminate randomness, and we then assess the results by looking at metrics like PSP, NASP, PSL, ISL, iteration count N_I, and execution time t.

Given the aforementioned spectral stopband constraints and parameter settings, we perform 300 Monte Carlo trials with each algorithm for the sequence length $N = 128$ in the first scenario, and we then record the output sequences for the evaluation of metrics in the temporal and spectral domains. Examples of the autocorrelation functions and the power spectrum of the output sequences produced by each contrast method are shown in Figure 6.5 and Figure 6.6, respectively. For such a short sequence length ($N = 128$), it can be shown from Figure 6.5 and Figure 6.6that all techniques are effective at concurrently suppressing the autocorrelation sidelobes and spectral stopbands. The Peak stopband power (PSP) values

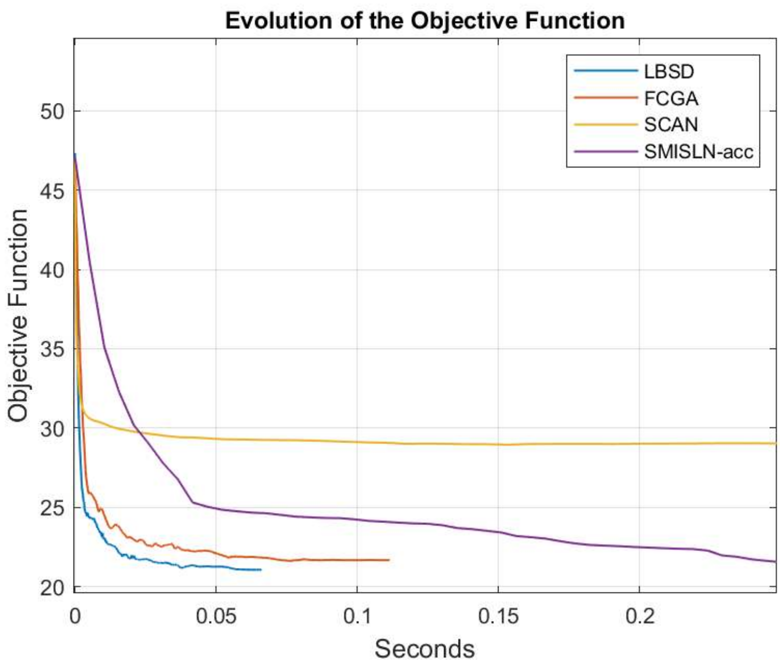

Figure 6.7: *Sparse Frequency Waveform Design Trials* - Cost function evolution versus time ($N = 128$).

for the sequences produced by the SCAN, Spectral-MISL, FCGA, SMISLN-acc, and proposed LBSD for this run are -13.81 dB, -12.44 dB, -19.27 dB, -16.13 dB, and -19.43 dB, respectively, and the corresponding PSL values are -14.56 dB, -14.22 dB for this particular single run. These results suggest that the suggested LBSD can suppress the autocorrelation sidelobes and spectral power in the stopbands as well as or even better than the SCAN, Spectral-MISL, SMISLN-acc, and FCGA.

We examine the cumulative distribution functions of ISL, PSL, PSP, NASP, iteration count, and execution time measurements and their average values over all trials because it is impossible to draw any firm conclusions from a single run. The cumulative distribution functions of each algorithm's performance metrics (PSP, NASP, ISL, PSL, iteration count N_I and time t) are shown in Figure 6.11(a-f), and Table 6.6 shows the average values for each metric. From a spectral domain standpoint, we can see in Figure 6.11(a) that the proposed LBSD and the FCGA, while achieving lower than others, both produce PSP values that are quite similar.

Contrarily, the proposed LBSD grants comparable NASP values to the FCGA and SMISLN-acc on average (See Table 6.6), even though the SMISLN-acc gets the lowest NASP value in Figure 6.11(b). Except for the SCAN method, all algorithms produce comparable ISL and PSL values from a temporal domain perspective. The SCAN algorithm is found to favor higher ISL suppression over spectral stopband suppression. According to Figure 6.11(e), the proposed LBSD algorithm performs similarly to the FCGA in terms of iteration count. However, as can be shown in Figure 6.11(f), the proposed LBSD executes much more faster than the FCGA algorithm and, according to Table 6.6, it has the lowest average execution time. In Figure 6.7, the evolution of the objective functions (in dB) of the algorithms is plotted versus time for this scenario (Spectral MISL's objective function is not included because it cannot be compared to other algorithms' objective functions), and it is evident that the proposed LBSD algorithm converges to the stationary point faster than the other contrast algorithms.

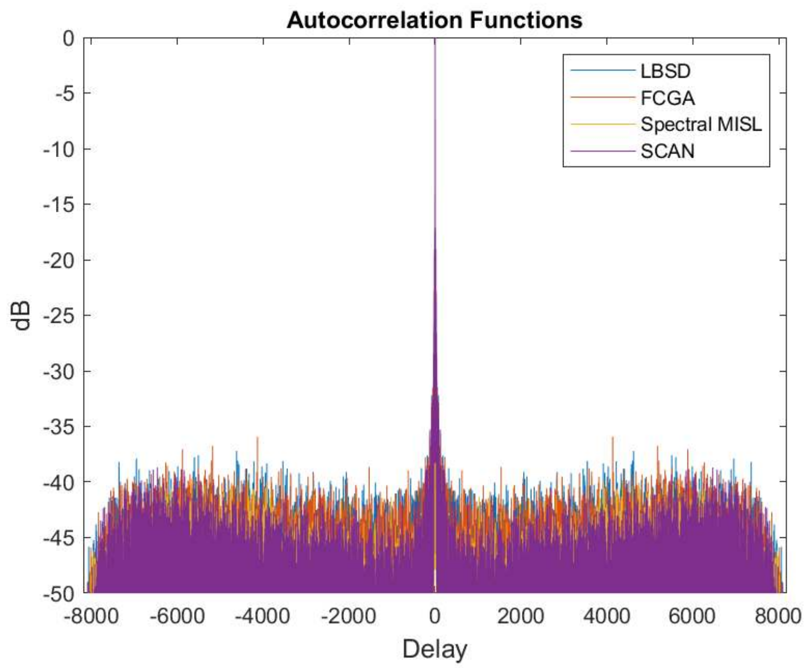

Figure 6.8: *Sparse Frequency Waveform Design Trials* - The normalized ACFs of the sequences ($N = 8192$).

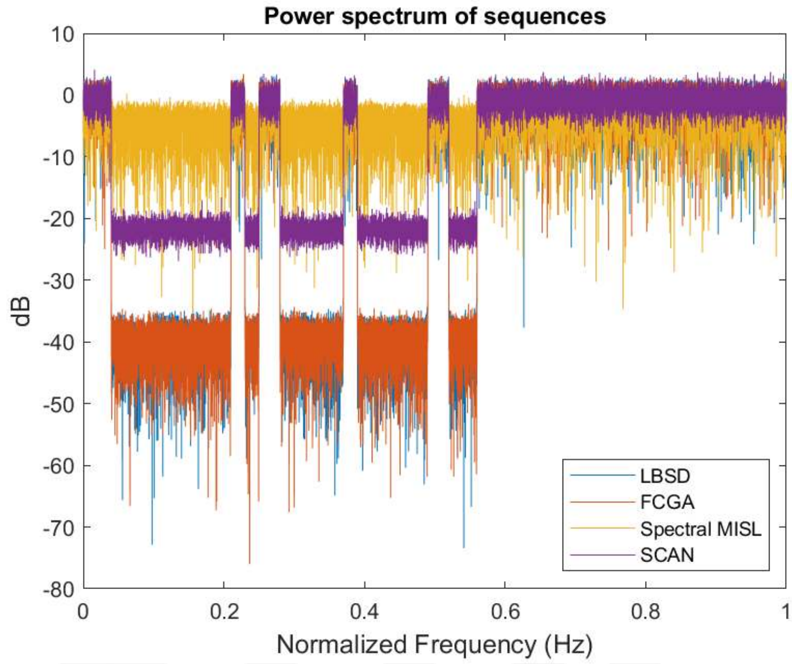

Figure 6.9: *Sparse Frequency Waveform Design Trials* - The normalized PSDs of the sequences ($N = 8192$).

The experiment is repeated in the second scenario with a much longer sequence length ($N = 8192$), and again, all algorithms are performed 300 times (The SMISLN-acc is excluded from these trials because, for such sequence lengths, the size of the stopband matrix used in the algorithm grows fairly big (See Σ_1 in [38]), resulting in exceptionally long execution time.). The autocorrelation functions and power spectrum of the output sequences synthesized by each contrast method for the sequence length $N = 8192$ are depicted in Figure 6.8 and Figure 6.9, respectively for an arbitrary single run. For such long sequence lengths, the proposed LBSD and FCGA algorithms provide deeper spectral stopband suppression than the SCAN and Spectral MISL algorithms, as shown in Figure 6.9. Furthermore, the evolution of the objective function (in dB) in Figure 6.10 reveals that the proposed LBSD algorithm converges significantly faster than existing contrast algorithms. Following that, the cumulative distribution functions of the experiment's metrics for all methods are presented in Figure 6.12(a-f), and the average values of the metrics are reported

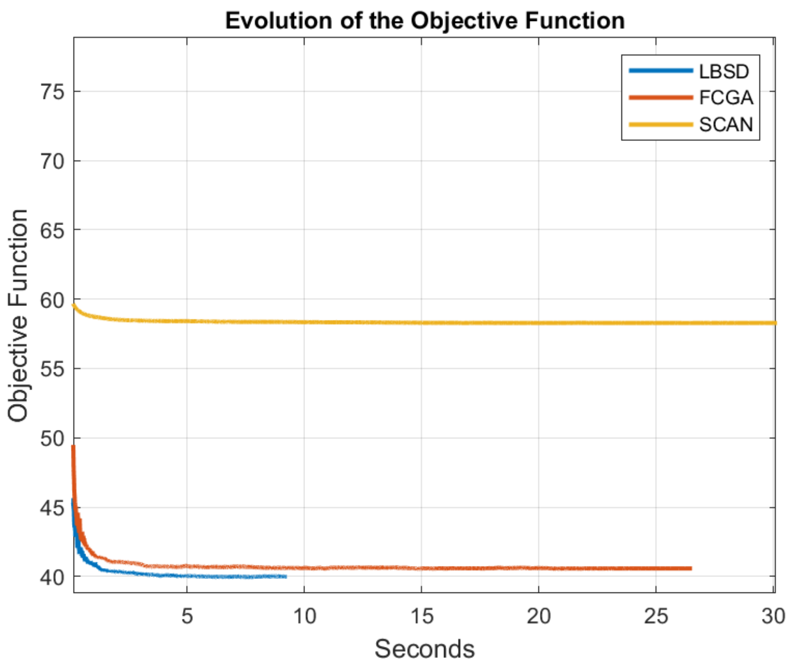

Figure 6.10: *Sparse Frequency Waveform Design Trials* - Cost function evolution versus time ($N = 8192$).

in Table 6.7. In contrast to the CDFs from the previous case with $N = 128$, the disparities in the CDF plots of all metrics for each method are more noticeable in Figure 6.12. By examining the CDFs of the PSP, NASP, ISL, and PSL metrics in Figure 6.12(a-d), it is clear that the SCAN and Spectral MISL provide moderate spectral stopband suppression while overemphasising correlation sidelobe reduction. In general, the proposed LBSD algorithm outperforms the FCGA in terms of PSP, NASP, ISL, and PSL. However, the proposed LBSD achieves the lowest performance metrics (t, Ni) and surpasses all other algorithms as demonstrated in Figure 6.12(e) and (f) in terms of iteration number and execution time. Table 6.7 also shows that the proposed LBSD has the lowest average iteration count and average execution time.

Table 6.6: *Sparse Frequency Waveform Design Trials* - Numerical results($N = 128$)

Algorithm	Average PSP (dB)	Average NASP (dB)	Average ISL	Average PSL (dB)	Average Iter. Count	Average Exec. Time (s)
SCAN [13]	-14.7696	-23.9013	1.2282	-14.2302	1816	0.0868
Spectral MISL [25]	-15.0220	-19.8839	1.3495	-14.0943	3663	0.0881
FCGA [37]	-20.0835	-24.5478	1.3687	-14.0600	260	0.0196
SMISLN-acc [38]	-15.6170	-24.4533	1.3848	-14.0459	905	6.3453
LBSD	-20.0064	-24.4965	1.3786	-14.0712	261	0.0099

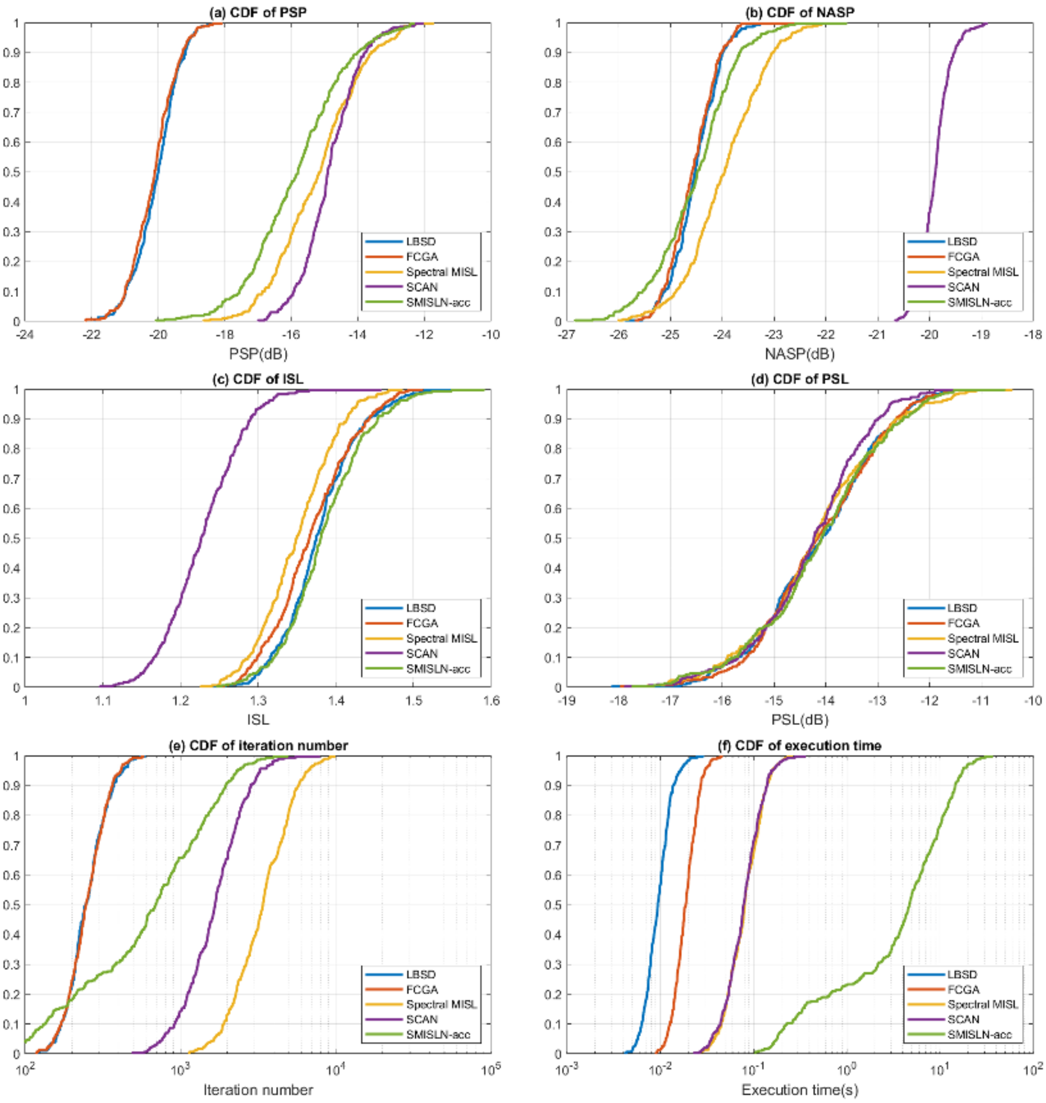

Figure 6.11: *Sparse Frequency Waveform Design Trials* - The CDF of the performance metrics ($N = 128$). (a) ISL CDF. (b) PSP CDF. (c) Iteration Count CDF (d) Exec Time CDF.

Table 6.7: *Sparse Frequency Waveform Design Trials* - Numerical results (N = 8192)

Algorithm	Average PSP (dB)	Average NASP (dB)	Average ISL	Average PSL (dB)	Average Iter. Count	Average Exec. Time (s)
SCAN [13]	-16.0901	-21.1221	0.9273	-14.2572	19819	49.2625
Spectral MISL [25]	1.9435	-2.2102	0.2543	-25.2328	26897	32.0067
FCGA [37]	-31.0045	-38.8892	1.0354	-14.1005	5561	15.7140
LBSD	-30.92611	-38.8475	1.0400	-14.1272	4010	6.0442

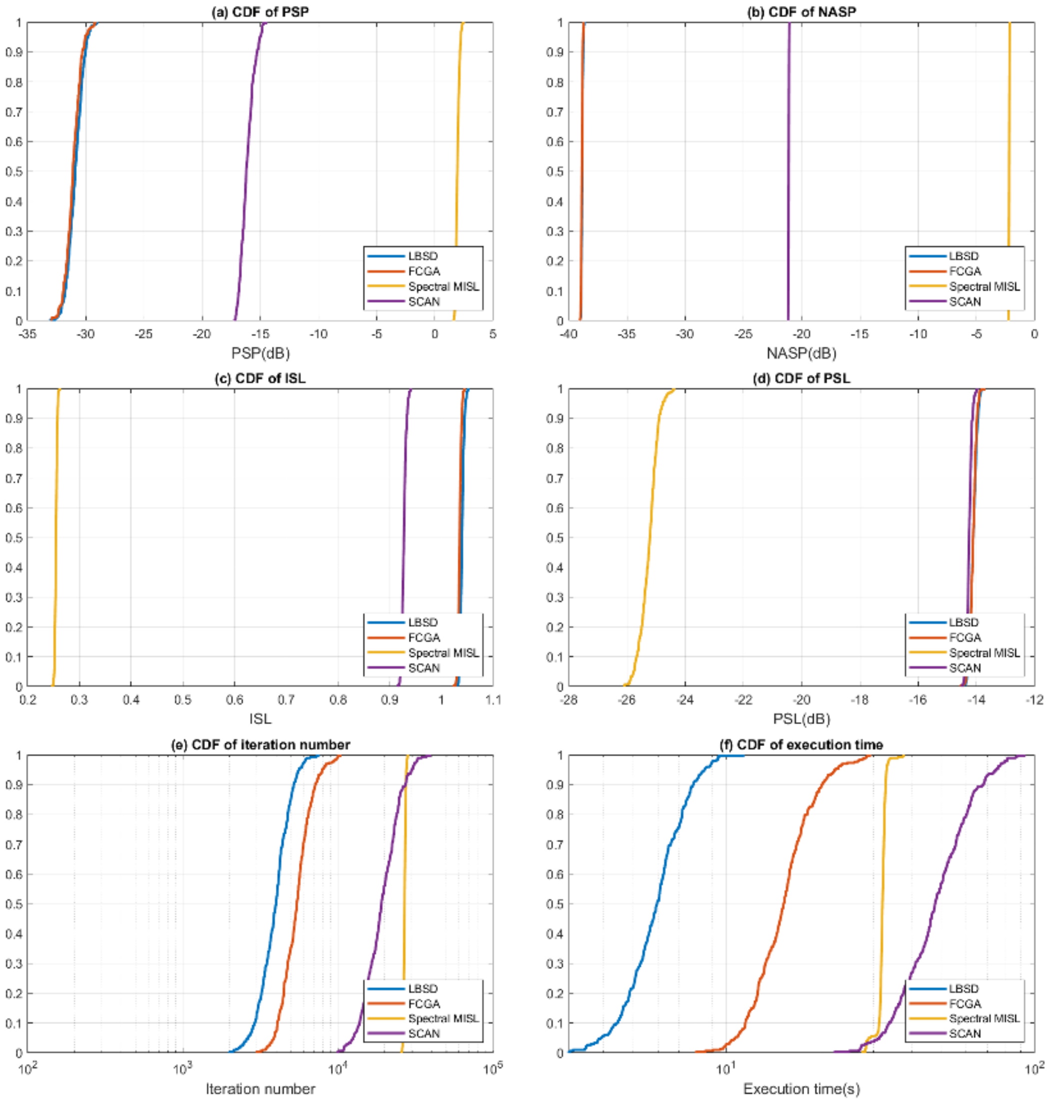

Figure 6.12: *Sparse Frequency Waveform Design Trials* - The CDF of the performance metrics ($N = 8192$). (a) ISL CDF. (b) PSP CDF. (c) Iteration Count CDF (d) CDF of Execution Time CDF.

When performance measures for both sequence lengths ($N = 128$ and $N = 8192$) are considered, the proposed LBSD greatly reduces execution time while maintaining or even improving PSP, NASP, ISL, PSL, and iteration count metrics overall. The results reveal that the proposed LBSD for sparse frequency waveform design is computationally efficient and remarkably fast.

Finally, the unified objective function J in (6.16) is composed of two weighted parts. For this multi-objective function model, the selection of the weight parameter λ has a great impact on optimization results of the algorithm. In the aforementioned periodic, aperiodic and sparse frequency sequence design experiments, we run all the algorithms for the fixed value of λ ($\lambda = 0$ for periodic/aperiodic sequence design and $\lambda = 0.9$ for sparse frequency sequence design). Therefore, to show the effect of the λ parameter choice on the unified objective function J and each separate costs J_{STOP}, J_{ISL}, we average the obtained results over 100 runs (with the given spectral stopbands) for various λ choices. The average values of unified objective function J and the other costs J_{STOP}, J_{ISL} versus λ ($\lambda = 0.1, 0.2, \ldots, 0.9$) is plotted in linear scale for the sequence length $N = 128$ in Figure 6.13. As can bee seen in the figure, for $\lambda > 0.5$ more spectral stopband power suppression is granted whereas for $\lambda < 0.5$ correlation sidelobe suppression is emphasized. Indeed, suppressing the autocorrelation sidelobes enforces a flat power spectrum. On the other hand, having spectral stopbands violates the spectrum flatness. In this regard, the trade between the temporal ISL constraint and spectral stopband constraint can be balanced by the weight parameter λ.

Lastly, in (6.16), the unified objective function J is composed of two weighted components. For this multi-objective function model, the selection of the weight parameter λ has a large impact on optimization results of the algorithm. In the aforementioned experiments on periodic, aperiodic, and sparse frequency sequence design, all algorithms are executed with λ set to a fixed value ($\lambda = 0$ for periodic/aperiodic sequence design and $\lambda = 0.9$ for sparse frequency sequence design). In order to demonstrate the effect of the λ parameter choice on the unified objective function J and each individual cost J_{STOP}, J_{ISL}, we calculate the average of 100 runs (with the specified spectral stopbands above) over a range of λ values. In Figure 6.13, the average values of the unified objective function J and the associated costs J_{STOP}, J_{ISL} are plotted against λ (($\lambda = 0.1, 0.2, \ldots, 0.9$)) in linear scale for the sequence length $N = 128$. As seen in the graph, when $\lambda > 0.5$, spectral stopband power suppression is accentuated, whereas correlation sidelobe suppression is emphasized when $\lambda < 0.5$. In fact, suppressing autocorrelation sidelobes results in a flat power spectrum. However, the flatness of the spectrum is violated if there are spectral stopbands. In this respect, the weight parameter λ can be used to balance the trade-off between the spectral stopband requirement and the temporal ISL constraint.

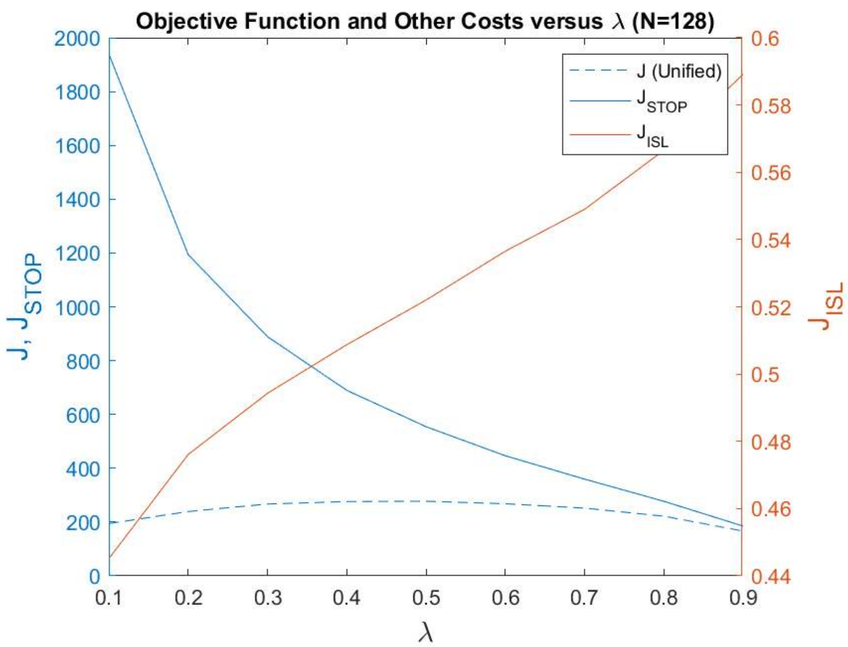

Figure 6.13: *Sparse Frequency Waveform Design Trials* - Objective Function and Other Costs versus λ ($N = 128$).

6.4 Summary

In this dissertation, we have presented a new class of Blind Source Separation algorithms and their applications on some practical problems.

In this study, we develop a novel algorithm for the design of constant modulus sequences that is based on a quasi-Newton optimization technique, namely L-BFGS. The proposed LBSD algorithm is applicable for both periodic and aperiodic sequence design, with the parameter λ controlling the balance between ACF sidelobe suppression and spectral stopband suppression. During the development of the proposed method, the bi-objective (ACF sidelobe and spectral stopband suppression) optimization problem is converted into an unconstrained single-objective optimization problem and then treated as a nonlinear large-scale problem. The problem is addressed using an L-BFGS procedure in which the search direction is derived from a two-loop L-BFGS recursion. This recursion generates a properly scaled search direction vector, thus a unit step is taken and the expense of calculating the step length is avoided. However, we implement a modified version of the step length selection rule in which we use the Taylor series expansion approach to calculate the step length only for the first m-iterations and occasionally for certain iterations when the L-BFGS recursion yields an ascending search direction.

The gradient and step length calculations are primarily based on (I)FFT operations and Hadamard products, whereas the L-BFGS recursion is based on elementary vector calculus operations. Overall, the algorithm proves to be computationally efficient and fast. Due to the L-BFGS technique and straightforward vector algebra involved in the computation of the gradient and step length, the algorithm's space complexity is low. Consequently, the low memory footprint makes it viable for designing very long sequences ($N > 2^{10}$).

The numerical simulations demonstrate that the proposed LBSD method outperforms existing state-of-the-art algorithms in terms of speed. The outcomes demonstrate that the proposed LBSD algorithm is a potential option for creating unimodular sequences that satisfy both temporal and spectral restrictions in less execution time than existing approaches while attaining good or even superior stopband power and correlation sidelobe level. As a result, we think the proposed LBSD algorithm can be beneficial for various spectrum-aware remote sensing applications, such as sonar and radar, and in particular for cognitive radar/radio systems where quick counteraction against jammers and interference in a dynamic radio environment is crucial.

Chapter 7

CONCLUSIONS

In this dissertation, we have presented two new radar waveform design algorithms specifically for noise radar applications and for spectrum-aware radar systems and additionally, we have developed a visual tool to evaluate the Low-Probability-of-Intercept characteristics of waveforms.

The first algorithm we propose is called 'Combined Spectral Shaping and Peak-to-Average Power Reduction (COSPAR)'. In our methodology, it is possible to generate infinitely many noise-like waveforms with desired autocorrelation sidelobe level owing to the configurable spectral shape of COSPAR signals. Moreover a cascaded PAPR reduction procedure is useful in the generation of power efficient noise waveform which could lead to higher transmit power and thus increased detection capability for radars.

The proposed visual tool for evaluating waveforms' LPI characteristics is founded upon the Spectral Kurtosis which acts on 2D time-frequency support of signals. As Kurtosis is an indicator of the deviation from Gaussian distribution, the main idea here is to check whether the signal has a structured time frequency support or not. If the signal has a structured time-frequency support this means that the signal is a deterministic signal (e.g., LFM signal). On the other hand, if the energy of the signal is evenly distributed in time-frequency plane as it is the case for COSPAR signals, then then Spectral Kurtosis tends to indicate a Gaussian distribution which means the signal resembles noise. In military arena, such noise-like signals could allow for covert radar mission while impairing the success of the modern adversary electronic protection systems which are capable of doing time-frequency analysis. In the future, we wish to extend this visual assessment tool into a quantitative analysis method to grade the LPI features of radar waveforms.

The second algorithm we propose is called L-BFGS based Sequence Design(L-BSD) algorithm which involves a Quasi-Newton optimization method i.e., the Limited Memory Broyden Fletcher Goldfarb Shanno method. In today's modern radar systems, the generation of signals shift from analog to digital. As the sampling rates of analog-digital converters increase year by year with the technological advances, more and more number of samples are needed to synthesize high bandwidth signals (for example, RF converters can directly output signals in the carrier band). In this respect, with increasing number of samples, the waveform synthesis algorithms have to converge fast under the related constraints. With this idea in mind, we posed the waveform synthesis problem as large-scale problem, a well-known topic in signal processing and then applied a second order nonlinear optimization method. We have successfully demonstrated the numerical simulation results and showed that the proposed method outperforms other contemporary waveform synthesis techniques in terms of execution time. This algorithm can be utilized in spectrum aware systems such as cognitive radar where agile generation of signals are a necessity.

In chapter 2, we have presented an overview on noise radar and cognitive radar applications we have highlighted and put forward the rationale for having waveforms with certain properties. We have highlighted the waveform diversity requirement for these trending radar applications.

In chapter 3 we have covered the preliminaries of pulse compression processing and related waveform peculiarities to introduce the reader with the base information required to comprehend the computational methods involved in the waveform design methods and then we outlined the construction methods of several important sequence design algorithms in chapter 4.

In chapter 5, we have addressed the dynamic range issue in noise radars, and then, we explained the steps of the proposed COSPAR waveform design algorithm in detail. We also introduced the novel PAPR reduction technique and the visual tool for evaluating waveforms' LPI features. Moreover, we reported several outcomes of field trials conducted in the shoreline with a noise radar demonstrator and showed the effectiveness of COSPAR signals.

In chapter 6, we addressed the spectrally compatible waveform design problem. We introduced a novel algorithm named L-BFGS based Sequence Design (LBSD) algorithm which involves an optimization method for the correlation sidelobes and the spectral stopbands suppression. We outlined the construction of the unified cost function, the derivation of the gradient and step size, and the algorithmic flow of the LBSD. We showed the efficiency of the proposed LBSD algorithm compared to state-of-art algorithms with numerical simulations.

Beyond the practical impact of the outcomes, the major theoretical contributions of this thesis are summarized as follows:

(i) In the development of the COSPAR signals, we have succesfully incorporated a customizable window function (i.e., Taylor Window) and a novel PAPR reduction method inspired by the Phase-Retrieval Algorithm (Gerchberg-Saxton Algortihm) into a waveform synthesis technique.

(ii) We have utilized the Spectral Kurtosis to evaluate time-frequency support of signals to assess the LPI property of signals.

(iii) In the development of the LBSD algorithm, we have succesfully applied a nonlinear optimization method to the waveform synthesis problem and the resulting algorithm proves to be efficient in terms of convergence speed .

Appendix A

AMBIGUITY FUNCTION

A.1 Doppler Frequency

Radars utilize Doppler frequency to calculate target radial velocity (range rate) and to discriminate between moving and stationary targets or objects such as clutter [113]. The Doppler effect is the term used to describe the change in the incident waveform's center frequency brought on by the target motion with respect to the radiation source. This frequency shift might be positive or negative depending on the target's motion direction. A waveform that is incident on a target will have equiphase wavefronts that are spaced apart by the wavelength. The reflected equiphase wavefronts will get close to each other due to a closing target (smaller wavelength). On the other hand, an opening or receding target (moving away from the radar) will result in an expansion (longer wavelength) of the reflected equiphase wavefronts. This phenomenon is illustrated in Figure A.1.

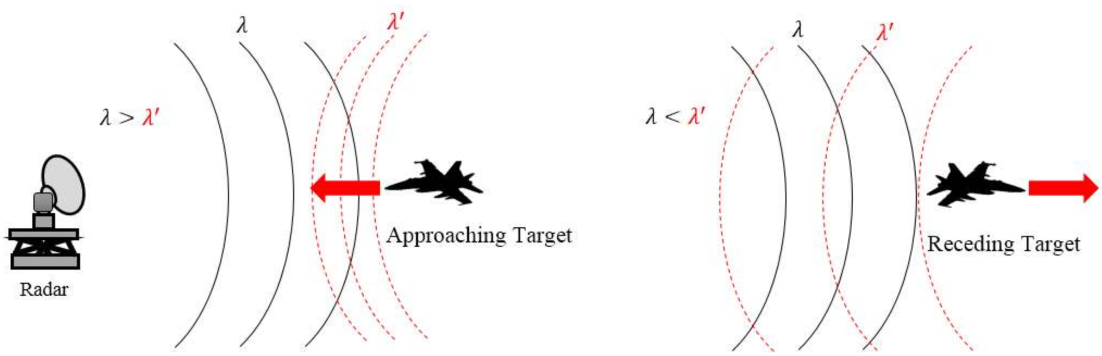

Figure A.1: Wavelength effects of target motion. Black straight line: Incident wave, Red dashed line: Reflected wave

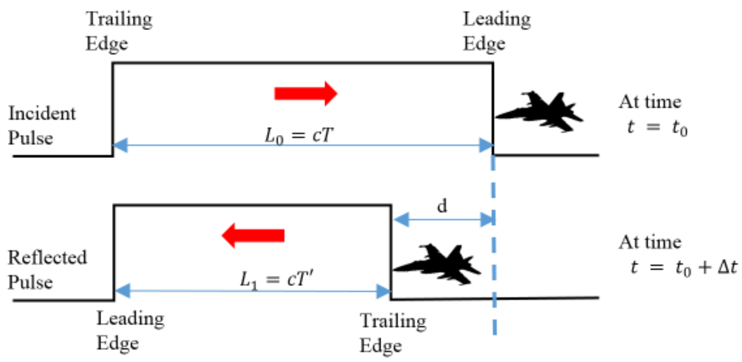

Figure A.2: Illustration of signal compression due to target radial motion.

Consider a pulse with duration T (in seconds) reflecting from an object that is moving towards the radar at radial speed v, as shown in Figure A.2. Assume d as the distance (in meters) that the object moves into the pulse during the interval Δt

$$d = v\Delta t \tag{A.1}$$

where Δt is equal to the time span between the pulse leading edge striking the target and the trailing edge striking the target. Since the pulse is moving at the speed of light c and the trailing edge has moved distance $cT - d$, then

$$\Delta t = \frac{cT - d}{c} \tag{A.2}$$

Combining A.1 and A.2, we obtain

$$d = \frac{cv}{c + v} T \tag{A.3}$$

Now, in Δt seconds the leading edge of pulse has moved in the direction of the radar a distance L_0,

$$L_0 = c\Delta t \tag{A.4}$$

Thus, the reflected pulse width is now T' seconds corresponding to L_1 meters,

$$L_1 = cT' = L_0 - d \tag{A.5}$$

Substituting (A.3) and (A.4) into (A.5) produces,

$$cT' = c\Delta t - \frac{cv}{c+v}T \tag{A.6}$$

$$cT' = \frac{c^2}{c+v}T - \frac{cv}{c+v}T = \frac{c^2 - cv}{c+v}T \tag{A.7}$$

$$T' = \frac{c-v}{c+v}T \tag{A.8}$$

Similarly, one can compute T' for an receding target. In this situation,

$$T' = \frac{c+v}{c-v}T \tag{A.9}$$

We will refer to the term $\eta \triangleq \frac{c+v}{c-v}$ as the time scaling factor(or time dilation factor) [3, 113]. Due to compression or expansion of the pulse, the frequency of the pulse will go up or down by the same scaling factor η. Denoting the modified frequency by f'_c, it follows

$$f'_c = \frac{c+v}{c-v}f_c = \eta f_c \tag{A.10}$$

where f_c is the carrier frequency of the incident signal. The Doppler frequency f_d is defined as the difference between $f'_c - f_c$. More precisely,

$$f_d = f'_c - f_c = \frac{c+v}{c-v}f_c - f_c = \frac{2v}{c-v}f_c \tag{A.11}$$

However, since $v \ll c$ and $c = \lambda f_c$, The Doppler frequency can be approximated by

$$f_d \approx \frac{2v}{c}f_c = \frac{2v}{\lambda} \tag{A.12}$$

A.2 Ambiguity Function

The ambiguity function (AF) represents the time response of a filter matched to a given finite energy signal when the signal is received with a Doppler shift f_d and a delay τ [3]. Let us denote a probing signal $s(t)$ with time support $[0, T]$ (i.e., s(t) is zero outside [0, T]). The continuous-time ambiguity function of $s(t)$ is defined as

$$\chi(\tau, f_d) = \int_{-\infty}^{\infty} s(t)s^*(t-\tau)e^{-j2\pi f_d(t-\tau)}dt \qquad \text{(A.13)}$$

where f_d is the Doppler frequency shift and τ is the time delay [3].

***Remark*:** Note that (A.13) is in fact the ambiguity function for *narrowband* signals (A popular rule of thumb says that if the signal bandwidth is less than one-tenth of the carrier frequency, the signal is regarded as *narrowband* signal [5]). In the following subsections, we will also discuss on the ambiguity function for wideband signals.

A.2.1 General Ambiguity Function

Assume that the transmitted signal is $s(t)$ and the target that reflects $s(t)$ has speed v (a positive v means closing target whereas a negative v means get receding target). The received signal $g(t)$ is a delayed and time-scaled version of $s(t)$:

$$g(t) = \sqrt{\eta}s(\eta(t-\tau)) \qquad \text{(A.14)}$$

where τ is the time delay and η is time scaling factor given by

$$\eta = \frac{c+v}{c-v} \qquad \text{(A.15)}$$

The factor $\sqrt{\eta}$ comes from the energy conservation in the time scaling:

$$E = \int |s(t)|^2 dt = \int |\sqrt{\eta}s(\eta t')|^2 dt' \qquad \text{(A.16)}$$

The general ambiguity function equals the matched filter output, which is given by the cross correlation of $s(t)$ and $g(t)$:

$$\bar{\chi}(\tau, \eta) = \sqrt{\eta} \int_{-\infty}^{\infty} s^*(t) s(\eta(t-\tau)) dt \tag{A.17}$$

Equation (A.17) is valid for general signals [3].

A.2.2 Narrowband Ambiguity Function

It is necessary to make two assumptions in order to specialize (A.17) to the well-known narrowband AF, which may be stated as

$$\chi(\tau, f_d) = \int_{-\infty}^{\infty} s^*(t) s(t-\tau) e^{j2\pi f_d (t-\tau)} dt \tag{A.18}$$

These two assumptions are [3];

(i) $v \ll c$

(ii) $s(t)$ is narrowband hence a time scaling can be considered as solely a frequency shift of the carrier.

We will prove that, (A.17) and (A.18) are equivalent under the above two assumptions, because

$$\sqrt{\eta} s(\eta(t-\tau)) \approx s(t-\tau) e^{2\pi f_d (t-\tau)} \tag{A.19}$$

for a certain f_d (see below).

To prove (A.19) note that $v \ll c$ leads to

$$\eta = \frac{1 + v/c}{1 - v/c} = \left(1 + \frac{v}{c}\right)\left(1 + \frac{v}{c} + \frac{v^2}{c^2} + ...\right) \approx 1 + \frac{2v}{c} \tag{A.20}$$

For this subsection, let $s(t) = A(t) e^{2\pi f_c t}$ where f_c is the carrier frequency and $A(t)$ is the envelop (slowly varying compared with f_c). $A(t)$ is the complex baseband equivalent signal and $s(t)$ is the corresponding passband signal. Then this leads to

$$\begin{aligned}\sqrt{\eta}s(\eta(t-\tau)) &= \sqrt{1+\frac{2v}{c}}A\left(\left(1+\frac{2v}{c}\right)(t-\tau)\right)e^{j2\pi f_c(1+\frac{2v}{c})(t-\tau)} \\ &\approx A(t-\tau)e^{j2\pi f_c(1+\frac{2v}{c})(t-\tau)} \\ &= A(t-\tau)e^{j2\pi(f_c+\frac{2v}{\lambda_c})(t-\tau)} \\ &= \left[A(t-\tau)e^{j2\pi f_c(t-\tau)}\right]e^{j2\pi f_d(t-\tau)} \\ &= s(t-\tau)e^{j2\pi f_d(t-\tau)}\end{aligned} \tag{A.21}$$

where λ_c is the carrier wavelength and f_d is given by the (narrowband) Doppler frequency shift:

$$f_d = \frac{2v}{\lambda_c} \tag{A.22}$$

This concludes the proof of (A.19) and the argument that (A.17) boils down to (A.18) when $v \ll c$ and the signal is narrowband. If we substitute $s(t) = A(t)e^{j2\pi f_c t}$ into the narrowband AF in (A.18), we obtain

$$\begin{aligned}\chi(\tau, f_d) &= e^{-j2\pi f_c \tau}\int_{-\infty}^{\infty} A^*(t)A(t-\tau)e^{j2\pi f_d(t-\tau)}dt \\ &\triangleq e^{-j2\pi f_c \tau}\chi_B(\tau, f_d)\end{aligned} \tag{A.23}$$

where $\chi_B(\tau, f_d)$ is defined as the baseband (narrowband) ambiguity function which is defined only in terms of the complex baseband equivalent signal $A(t)$ [3].

***Remark*:** As a result, we may plot or analyze the modulus of $\chi_B(\tau, f_d)$ (the Baseband AF) when we wish to examine or plot an ambiguity function of an RF passband signal. [3]. Using $\chi_B(\tau, f_d)$ instead of $\chi(\tau, f_d)$ is justified because from (A.23) we see that the equality $|\chi_B(\tau, f_d)| = |\chi(\tau, f_d)|$ holds [3]. Indeed, (A.13) is the same as the AF $\chi_B(\tau, f_d)$ here, i.e., the $s(t)$ in (A.13) corresponds to the baseband signal $A(t)$ here.

A.2.3 Discrete (Narrowband) Ambiguity Function

For this subsection, we limit our focus to baseband waveforms with the following modulations [3]:

$$s(t) = \sum_{n=1}^{N} x(n)u_n(t), \quad 0 \leq t \leq T \tag{A.24}$$

where $\{x(n)\}_{n=1}^{N}$ is the modulating code sequence that is to be designed (which is assumed to be zero when $n \notin [1, N]$) and $u_n(t)$ is an ideal rectangular shaping pulse of time length t_u (thus $T = Nt_u$) described by

$$u_n(t) = \frac{1}{\sqrt{t_u}} \mathrm{rect}\left(\frac{t-(n-1)t_u}{t_u}\right), \quad n = 1, ..., N, \tag{A.25}$$

where

$$\mathrm{rect}(t) = \begin{cases} 1,\ 0 \leq t \leq 1, \\ 0,\ \text{elsewhere}, \end{cases} \tag{A.26}$$

The energy of $\{x(n)\}_{n=1}^{N}$ is restricted to be N, i.e.,

$$\sum_{n=1}^{N} |x(n)|^2 = N. \tag{A.27}$$

Using the waveform defined in (A.24), the ambiguity function (A.13) can be simplified as follows.Replace (A.24) in (A.13) to obtain

$$\begin{aligned} \chi(\tau, f_d) &= \int_0^T \left(\sum_{n=1}^{N} x(n)u_n(t)\right)\left(\sum_{m=1}^{N} x^*(m)u_m(t-\tau)\right) e^{-j2\pi f_d(t-\tau)}dt \\ &= \sum_{m=1}^{N}\sum_{n=1}^{N} x^*(m)\left(\int_0^T u_n(t)u_m(t-\tau)e^{-j2\pi f_d(t-\tau)}dt\right) x(n). \end{aligned} \tag{A.28}$$

Suppose the time grid $\{\tau = kt_u\}$ ($k = -N+1, ..., 0, ..., N-1$) whose points are integer multiples of the subpulse length t_u. Then we can calculate $\chi(\tau, f_d)$ at $\tau = kt_u$ simply as:

$$\begin{aligned}\chi(kt_u, f_d) &= \sum_{m=1}^{N}\sum_{n=1}^{N} x^*(m)\left(\int_{(n-1)t_u}^{nt_u} |u_n(t)|^2 e^{-j2\pi f_d(t-kt_u)}dt\right)\delta_{m+k,n}x(n) \\ &= \frac{e^{j\pi f_d t_u}\sin(\pi f_d t_u)}{\pi f_d t_u}\sum_{n=1}^{N} x(n)x^*(n-k)e^{-j2\pi f_d t_u(n-k)}dt\end{aligned} \tag{A.29}$$

Notice that $\chi(kt_u, f_d)$ equals zero if k lies outside $[-N+1, N-1]$. Similarly to the time grid, we consider the frequecy frid ($fd = p/Nt_u$) for an integer p. Then we obtain

$$\chi(kt_u, \frac{p}{Nt_u}) = e^{j\pi\frac{p}{N}}\text{sinc}\left(\pi\frac{p}{N}\right)\tilde{\chi}(k,p) \tag{A.30}$$

where $\text{sinc}(x) = \sin(x)/x$ and $\tilde{\chi}(k,p)$ is denoted as the discrete ambiguity function [3]:

$$\begin{aligned}\tilde{\chi}(k,p) &= \sum_{n=1}^{N} x(n)x^*(n-k)e^{-j2\pi\frac{(n-k)p}{N}} \\ k &= -N+1, ..., N-1, \quad p = -\frac{N}{2}, ..., \frac{N}{2}-1.\end{aligned} \tag{A.31}$$

The range of p is selected as $-N/2, ..., N/2-1$ since it corresponds to the largest Doppler frequency range which can be unambiguously identified (notice that the bandwidth of $s(t)$ is approximately equal to $1/t_u$). Also take notice that we have implicitly assumed and will continue to assume that N is even associated with our subject without losing generality. An odd N would result in the range $p = -(N-1)/2, ..., (N-1)/2$, which would slightly alter the discussion that follows.

In practical applications related to real life, the Doppler frequency f_d could be much smaller than the bandwidth of the transmit waveform. For instance, considering an X-band radar operating at wavelength $\lambda = 3$ cm, a fighter jet flying at a speed Mach 3 ($v = 1029$ m/s) induces a Doppler frequency of only

$$f = \frac{2v}{\lambda} = \frac{2 \times 1029\text{m/s}}{0.03\text{m}} = 68.6\text{kHz} \tag{A.32}$$

this is much less than the bandwidth which is on the order of many MHz. As another example, for a sonar operating at a frequency $f = 20$ kHz (corresponding to a wavelength of $1500/20 = 75$ mm), a fast-moving submarine at the speed of 25 knots ($v = 12.8$ m/s) induces a Doppler frequency of

$$f = \frac{2v}{\lambda} = \frac{2 \times 12.8\text{m/s}}{0.075\text{m}} = 341.3\text{Hz} \tag{A.33}$$

which can also be considered to be very small compared with the typical several-kHz bandwidth of legacy sonars. In such cases, we can limit our attention to values of $|p| \ll N$, in which case $\text{sinc}(\pi p/N) \approx 1$ and therefore [3]

$$\left|\chi(kt_u, \frac{p}{Nt_u})\right| \approx |\tilde{\chi}(k,p)|, \quad k = -N+1, ..., N-1, \quad |p| \ll N \tag{A.34}$$

***Remark*:** Since, almost always, it is merely the magnitude of ambiguity function that matters in target detection applications, (A.34) tells us that it is sufficient to take into account the discrete ambiguity function expressed in (A.31) [3]. The well known ambiguity function properties of constant volume and symmetry also hold for the discrete version in (A.31).

A.2.4 Wideband Ambiguity Function

While it is sufficient to consider the envelope (the baseband component) when calculating the AF of a narrowband signal (assuming $v \ll c$ is true), this is not the case when calculating the AF of a wideband signal. If we substitute $s(t) = A(t)e^{j2\pi f_c t}$ into the general AF in (A.17), we obtain

$$\begin{aligned}\bar{\chi}(\tau,\eta) &= e^{-j2\pi f_c \eta\tau}\sqrt{\eta}\int_{-\infty}^{\infty} A^*(t)A(\eta(t-\tau))e^{j2\pi f_c(\eta-1)t}dt \\ &\triangleq e^{-j2\pi f_c \eta\tau}\bar{\chi}_B(\tau,\eta).\end{aligned} \tag{A.35}$$

Thus, the proper formula for the AF of a wideband signal (in its baseband form) can be expressed as

$$\bar{\chi}_B(\tau, \eta) = \sqrt{\eta} \int_{-\infty}^{\infty} A^*(t) A(\eta(t - \tau)) e^{j2\pi f_c(\eta - 1)t} dt \tag{A.36}$$

Notice that for a narrowband AF the following well-known symmetry is valid:

$$\chi(\tau, f) = \chi^*(-\tau, -f). \tag{A.37}$$

But, for the general AF in (A.17) or (A.36), there is no such perfect symmetry. Instead, it is simple to demonstrate that [3]

$$\bar{\chi}(\tau, v) = \bar{\chi}^*(-\eta\tau, -v), \tag{A.38}$$

$$\left|\bar{\chi}_B(\tau, v)\right| = \left|\bar{\chi}_B(-\eta\tau, -v)\right|, \tag{A.39}$$

where, for clarity, v is used in lieu of η according to (A.15).

***Remark*:** Therefore, if one wishes to plot the modulus or the magnitude of the general AF in (A.17) or (A.36), all four quadrants must be shown, although the AF looks almost symmetric because the scaling factor η is close to 1 [3].

A.3 Conclusion

In this appendix, we derived the ambiguity function both for the narrowband and wideband continuous-time signals. We showed that under certain assumptions, the narrowband ambiguity function of an RF signal can be analyzed by its underlying baseband signal since the modulus of the AFs are equivalent [3]. A popular rule of thumb states that if the signal bandwidth is less than one-tenth of the carrier frequency, the signal is considered a narrowband signal, and it is reasonable to assume that the target motion causes only a Doppler shift of the carrier frequency according to (A.22) [5]. In most practical radar applications, ($f_c \gg 10 \times BW$) a narrowband AF representation is sufficient. Otherwise, time scaling should be considered, which also affects the envelope of the signal (wideband case). Finally, we derived the discrete ambiguity function which can be used for the discrete baseband waveform sequences.

Appendix B

LIMITED MEMORY BROYDEN-FLETCHER-GOLDFARB-SHANNO (L-BFGS) RECURSION

First, we revisit the Broyden-Fletcher-Goldfarb-Shanno (BFGS) approach, which will serve as the basis for the Limited Memory BFGS method. Let $\mathbf{x}^k \in \mathbb{R}^{N\times 1}$ be a vector, and let ∇f^k be the gradient of the objective function f at k^{th} iteration. The BFGS technique then has the following update rule for each iteration.

$$\mathbf{x}^{k+1} = \mathbf{x}^k - \mu^k \mathbf{H}^k \nabla f^k, \tag{B.1}$$

where $\mathbf{H}^k$ is the inverse Hessian approximation and μ^k denotes the step size. We'll suppose that $\tilde{\mathbf{d}}^k = -\mathbf{H}^k \nabla f^k$ is the search direction. Every iteration of BFGS updates $\mathbf{H}^k$ using the following formula:

$$\mathbf{H}^{k+1} = \mathbf{V}^{k^T} \mathbf{H}^k \mathbf{V}^k + \rho^k \mathbf{s}^k \mathbf{s}^{k^T}, \tag{B.2}$$

where

$$\rho^k = \frac{1}{\mathbf{y}^{k^T}\mathbf{s}^k}, \qquad \mathbf{V}^k = \mathbf{I} - \rho^k \mathbf{s}^k \mathbf{s}^{k^T}, \tag{B.3}$$

and

$$\mathbf{s}^k = \mathbf{x}^{k+1} - \mathbf{x}^k, \qquad \mathbf{y}^k = \nabla f^{k+1} - \nabla f^k. \tag{B.4}$$

When N is a large number, the cost of keeping the inverse Hessian approximation $\mathbf{H}^k$ in the computer memory increases because of the dimensionality of the $N \times N$ Hessian matrix. To address this issue, a prespecified number (i.e., m) of the vector pairs $\{\mathbf{s}, \mathbf{y}\}$, which are employed to implicitly generate $\mathbf{H}^k \nabla f^k$ are saved in memory. A series of vector operations such as inner products and summations involving ∇f^k and the pairs $\{\mathbf{s}, \mathbf{y}\}$ are used to infer the product $\mathbf{H}^k \nabla f^k$. The oldest vector pair in the set of pairings $\{\mathbf{s}, \mathbf{y}\}$ is eliminated after each iteration, and the new pair $\{\mathbf{s}^k, \mathbf{y}^k\}$ is added to the set. As a result, the most recent inverse Hessian approximation always includes the curvature information from the most recent m iterations. According to empirical analysis, suitable values for m range from 3 to 20 for positive outcomes [110].

The following is the procedure for updating the L-BFGS iterations: At the kth iteration, we initialize the inverse Hessian approximation $\mathbf{H}_0^k$ first using the current vector $\mathbf{x}^k$ and the collection of vector pairs specified by $\{\mathbf{s}^p, \mathbf{y}^p\}$ for $p = k - m, \ldots, k - 1$ (Contrary to traditional BFGS, each iteration's initial estimate $\mathbf{H}_0^k$ may be different). Then, the following recursive formulation can be used to compute the L-BFGS approximation of $\mathbf{H}^k$ in (B.2):

$$
\begin{aligned}
\mathbf{H}^k =& (\mathbf{V}^{k-1^T} ... \mathbf{V}^{k-m^T}) \mathbf{H}_0^k (\mathbf{V}^{k-m} \ldots \mathbf{V}^{k-1}) \\
&+ \rho^{k-m} (\mathbf{V}^{k-1^T} ... \mathbf{V}^{k-m+1^T}) \mathbf{s}^{k-m} \mathbf{s}^{k-m^T} (\mathbf{V}^{k-m+1} ... \mathbf{V}^{k-1}) \\
&+ \rho^{k-m+1} (\mathbf{V}^{k-1^T} ... \mathbf{V}^{k-m+2^T}) \mathbf{s}^{k-m+1} \mathbf{s}^{k-m+1^T} (\mathbf{V}^{k-m+2} ... \mathbf{V}^{k-1}) \\
&+ ... \\
&+ \rho^{k-1} \mathbf{s}^{k-1} \mathbf{s}^{k-1^T}.
\end{aligned} \tag{B.5}
$$

To calculate the product $\mathbf{H}^k \nabla f^k$ efficiently, a two-loop recursive approach as described in Algorithm 6 can be developed from (B.5).

In Algorithm 6, the L-BFGS recursion scheme uses $4mn$ multiplications, except for the multiplication $\mathbf{H}_0^k \mathbf{q}$. Furthermore, if $\mathbf{H}_0^k \mathbf{q}$ is diagonal, only n extra multiplications are needed. As a result, the L-BFGS recursion is computationally inexpensive. In addition, $\mathbf{H}_0^k$ can be chosen arbitrarily in each iteration because multiplication by the initial estimate $\mathbf{H}_0^k$ is decoupled from the remaining recursive calculations.

Algorithm 6 L-BFGS two-loop recursion

$\mathbf{q} \leftarrow \nabla f^k$
for $p = k-1, k-2, \ldots, k-m$ **do**
  $\alpha_p = \rho^p \left(\mathbf{s}^p\right)^T \mathbf{q}$
  $\mathbf{q} = \mathbf{q} - \alpha_p \mathbf{y}^p$
end for
$\mathbf{b} \leftarrow \mathbf{H}_0^k \mathbf{q}$
for $p = k-m, k-m+1, \ldots, k-1$ **do**
  $\beta = \rho^p \left(\mathbf{y}^p\right)^T \tilde{\mathbf{d}}$
  $\mathbf{b} = \mathbf{b} + \mathbf{s}^p \left(\alpha_p - \beta\right)$
end for
$\tilde{\mathbf{d}} = -\mathbf{H}^k \nabla f^k \leftarrow -\mathbf{b}$

A preferred method to initialize $\mathbf{H}_0^k$ is to construct $\mathbf{H}_0^k$ as a diagonal Identity matrix scaled by a factor γ^k i.e., $\mathbf{H}_0^k = \gamma^k I$ where γ^k is defined as

$$\gamma^k = \frac{\mathbf{s}_{i-1}^T \mathbf{y}_{i-1}}{\mathbf{y}_{i-1}^T \mathbf{y}_{i-1}}. \tag{B.6}$$

Along the most recent search direction, the scaling factor γ^k approximates the size of the actual Hessian matrix. This process ensures that the final search direction vector $\tilde{\mathbf{d}}$ is of the right size; therefore no additional calculations are needed to determine the step length, and thus unit step ($\mu^k = 1$) is adopted.

BIBLIOGRAPHY

[1] S. Haykin, "Cognitive radar: a way of the future," *IEEE Signal Processing Magazine*, vol. 23, no. 1, pp. 30–40, 2006.

[2] S. Z. Gurbuz, H. D. Griffiths, A. Charlish, M. Rangaswamy, M. S. Greco, and K. Bell, "An overview of cognitive radar: Past, present, and future," *IEEE Aerospace and Electronic Systems Magazine*, vol. 34, no. 12, pp. 6–18, 2019.

[3] J. Li and H. He, *Waveform Design for Active Sensing Systems: A Computational Approach*. New York, USA, Cambridge University Press, 2012.

[4] G. Cui, A. D. Maio, A. Farina, and J. Li, *Radar Waveform Design Based on Optimization Theory*, ser. Radar, Sonar & Navigation. Stevenage, London, SciTech Publishing, 2020. [Online]. Available: https://digital-library.theiet.org/content/books/ra/sbra533e

[5] N. Levanon and E. Mozeson, *Radar Signals*, ser. Wiley - IEEE. Wiley, 2004.

[6] C. Guan, Z. Zhou, and X. Zeng, "A phase-coded sequence design method for active sonar," *Sensors*, vol. 20, no. 17, 2020.

[7] S. W. Golomb and G. Gong, *Signal Design for Good Correlation: For Wireless Communication, Cryptography, and Radar*. New York, USA, Cambridge University Press, 2005.

[8] A. Aubry, A. D. Maio, Y. Huang, M. Piezzo, and A. Farina, "A new radar waveform design algorithm with improved feasibility for spectral coexistence," *IEEE Transactions on Aerospace and Electronic Systems*, vol. 51, no. 2, pp. 1029–1038, 2015.

[9] W. Rowe, P. Stoica, and J. Li, "Spectrally constrained waveform design [sp tips tricks]," *IEEE Signal Processing Magazine*, vol. 31, no. 3, pp. 157–162, 2014.

[10] M. J. Lindenfeld, "Sparse frequency transmit-and-receive waveform design," *IEEE Transactions on Aerospace and Electronic Systems*, vol. 40, no. 3, pp. 851–861, 2004.

[11] W. Liu, Y. Lu, and M. Lesturgie, "Optimal sparse waveform design for hfswr system," in *2007 International Waveform Diversity and Design Conference*, 2007, pp. 127–130.

[12] J. Salzman, D. Akamine, and R. Lefevre, "Optimal waveforms and processing for sparse frequency uwb operation," in *Proceedings of the 2001 IEEE Radar Conference (Cat. No.01CH37200)*, 2001, pp. 105–110.

[13] H. He, P. Stoica, and J. Li, "Waveform design with stopband and correlation constraints for cognitive radar," in *2010 2nd International Workshop on Cognitive Information Processing*, 2010, pp. 344–349.

[14] S. D. Blunt and E. L. Mokole, "Overview of radar waveform diversity," *IEEE Aerospace and Electronic Systems Magazine*, vol. 31, no. 11, pp. 2–42, 2016.

[15] R. H. Barker, "Group sysnchronizing of binary digital systems," in *Communication Theory*, W. Jackson, Ed. London: Butterworths Scientific Publications, 1953, pp. 273–287.

[16] R. Frank, "Polyphase codes with good nonperiodic correlation properties," *IEEE Transactions on Information Theory*, vol. 9, no. 1, pp. 43–45, 1963.

[17] D. Chu, "Polyphase codes with good periodic correlation properties (corresp.)," *IEEE Transactions on Information Theory*, vol. 18, no. 4, pp. 531–532, 1972.

[18] B. Lewis and F. Kretschmer, “A new class of polyphase pulse compression codes and techniques,” *IEEE Transactions on Aerospace and Electronic Systems*, vol. AES-17, no. 3, pp. 364–372, 1981.

[19] F. Kretschmer and B. Lewis, “Polyphase pulse compression waveforms,” *NRL Report 8540, Naval Research Laboratory, Washington D.C.*, 1982.

[20] N. Zhang and S. W. Golomb, “Polyphase sequence with low autocorrelations,” *IEEE Transactions on Information Theory*, vol. 39, no. 3, pp. 1085–1089, 1993.

[21] L.-S. Tsai, W.-H. Chung, and D.-s. Shiu, “Synthesizing low autocorrelation and low papr ofdm sequences under spectral constraints through convex optimization and gs algorithm,” *IEEE Transactions on Signal Processing*, vol. 59, no. 5, pp. 2234–2243, 2011.

[22] S. Mertens, “Exhaustive search for low-autocorrelation binary sequences,” *Journal of Physics A: Mathematical and General*, vol. 29, no. 18, pp. L473–L481, sep 1996.

[23] W. H. Mow, K. Du, and W. H. Wu, “New evolutionary search for long low autocorrelation binary sequences,” *IEEE Transactions on Aerospace and Electronic Systems*, vol. 51, no. 1, pp. 290–303, 2015.

[24] P. Stoica, H. He, and J. Li, “New algorithms for designing unimodular sequences with good correlation properties,” *IEEE Transactions on Signal Processing*, vol. 57, no. 4, pp. 1415–1425, 2009.

[25] J. Song, P. Babu, and D. P. Palomar, “Optimization methods for designing sequences with low autocorrelation sidelobes,” *IEEE Transactions on Signal Processing*, vol. 63, no. 15, pp. 3998–4009, 2015.

[26] D. R. Hunter and K. Lange, “A tutorial on mm algorithms,” *The American Statistician*, vol. 58, no. 1, pp. 30–37, 2004.

[27] J. Song, P. Babu, and D. P. Palomar, "Sequence design to minimize the weighted integrated and peak sidelobe levels," *IEEE Transactions on Signal Processing*, vol. 64, no. 8, pp. 2051–2064, 2016.

[28] P. Stoica, H. He, and J. Li, "On designing sequences with impulse-like periodic correlation," *IEEE Signal Processing Letters*, vol. 16, no. 8, pp. 703–706, 2009.

[29] P. J. Kajenski, "Design of low-sidelobe phase-coded waveforms," *IEEE Transactions on Aerospace and Electronic Systems*, vol. 55, no. 6, pp. 2891–2898, 2019.

[30] S. P. Sankuru and P. Babu, "Designing unimodular sequence with good autocorrelation properties via block majorization-minimization method," *Signal Processing*, vol. 176, p. 107707, 2020.

[31] ——, "A fast iterative algorithm to design phase-only sequences by minimizing the isl metric," *Digital Signal Processing*, vol. 111, p. 102991, 2021.

[32] G. Wang and Y. Lu, "Designing single/multiple sparse frequency waveforms with sidelobe constraint," *IET Radar, Sonar Navigation*, vol. 5, no. 1, pp. 32–38, 2011.

[33] J. Liang, H. C. So, C. S. Leung, J. Li, and A. Farina, "Waveform design with unit modulus and spectral shape constraints via lagrange programming neural network," *IEEE Journal of Selected Topics in Signal Processing*, vol. 9, no. 8, pp. 1377–1386, 2015.

[34] J. Liang, H. C. So, J. Li, and A. Farina, "Unimodular sequence design based on alternating direction method of multipliers," *IEEE Transactions on Signal Processing*, vol. 64, no. 20, pp. 5367–5381, 2016.

[35] B. O'Donnell and J. M. Baden, "Fast gradient descent for multi-objective waveform design," in *2016 IEEE Radar Conference (RadarConf)*, 2016, pp. 1–5.

[36] D. Zhao, Y. Wei, and Y. Liu, “Spectrum optimization via fft-based conjugate gradient method for unimodular sequence design,” *Signal Processing*, vol. 142, pp. 354 – 365, 2018.

[37] L. Tang, Y. Zhu, and Q. Fu, “Fast algorithm for designing periodic/aperiodic sequences with good correlation and stopband properties,” *EURASIP Journal on Advances in Signal Processing*, vol. 2018, no. 1, p. 57, 9 2018.

[38] O. T. Bişkin and O. Akay, “Designing radar transmit sequences satisfying simultaneous temporal integrated sidelobe level and spectral stopband constraints,” *Digital Signal Processing*, vol. 107, p. 102867, 2020.

[39] R. Lin, M. Soltanalian, B. Tang, and J. Li, “Efficient design of binary sequences with low autocorrelation sidelobes,” *IEEE Transactions on Signal Processing*, vol. 67, no. 24, pp. 6397–6410, 2019.

[40] G. Cui, Y. Fu, X. Yu, and J. Li, “Local ambiguity function shaping via unimodular sequence design,” *IEEE Signal Processing Letters*, vol. 24, no. 7, pp. 977–981, 2017.

[41] G. Cui, X. Yu, G. Foglia, Y. Huang, and J. Li, “Quadratic optimization with similarity constraint for unimodular sequence synthesis,” *IEEE Transactions on Signal Processing*, vol. 65, no. 18, pp. 4756–4769, 2017.

[42] A. De Maio, Y. Huang, M. Piezzo, S. Zhang, and A. Farina, “Design of optimized radar codes with a peak to average power ratio constraint,” *IEEE Transactions on Signal Processing*, vol. 59, no. 6, pp. 2683–2697, 2011.

[43] W. Fan, J. Liang, G. Yu, H. C. So, and G. Lu, “Minimum local peak sidelobe level waveform design with correlation and/or spectral constraints,” *Signal Processing*, vol. 171, p. 107450, 2020.

[44] H. Esmaeili-Najafabadi, M. Ataei, and M. F. Sabahi, “Designing sequence with minimum psl using chebyshev distance and its application for chaotic mimo radar waveform design,” *IEEE Transactions on Signal Processing*, vol. 65, no. 3, pp. 690–704, 2017.

[45] J. Zhang, N. Xu, H. Song, and C. Zhang, “Sequence set design for waveform-agile coherent radar systems,” *EURASIP Journal on Advances in Signal Processing*, vol. 2020, no. 1, p. 31, Jul 2020.

[46] H. E. Najafabadi, H. Leung, and P. W. Moo, “Designing sequences with minimized mean sidelobe level for cognitive radars,” *IEEE Access*, vol. 9, pp. 101 643–101 654, 2021.

[47] A. Stove, G. Galati, F. De Palo, C. Wasserzier, A. Y. Erdogan, K. Savci, and K. Lukin, “Design of a noise radar demonstrator,” in *2016 17th International Radar Symposium (IRS)*, 2016, pp. 1–6.

[48] K. Savci, A. Y. Erdogan, and T. O. Gulum, “Software defined l-band noise radar demonstrator,” in *2016 17th International Radar Symposium (IRS)*, 2016, pp. 1–4.

[49] K. Savci, A. G. Stove, A. Y. Erdogan, G. Galati, K. A. Lukin, G. Pavan, and C. Wasserzier, “Trials of a noise-modulated radar demonstrator – first results in a marine environment,” in *2019 20th International Radar Symposium (IRS)*, 2019, pp. 1–9.

[50] K. Savci and A. Y. Erdoğan, “Digital correlator: A scalable and efficient fpga implementation for radar receivers,” in *2019 Signal Processing Symposium (SPSympo)*, 2019, pp. 207–211.

[51] N. Çotuk, A. H. Kayran, A. Aytun, and K. Savci, “Detection of marine noise radars with spectral kurtosis method,” *IEEE Aerospace and Electronic Systems Magazine*, vol. 35, no. 9, pp. 22–31, 2020.

[52] K. Savci, A. G. Stove, F. De Palo, A. Y. Erdogan, G. Galati, K. A. Lukin, S. Lukin, P. Marques, G. Pavan, and C. Wasserzier, "Noise radar—overview and recent developments," *IEEE Aerospace and Electronic Systems Magazine*, vol. 35, no. 9, pp. 8–20, 2020.

[53] F. D. Palo, G. Galati, G. Pavan, C. Wasserzier, and K. Savci, "Introduction to noise radar and its waveforms," *Sensors*, vol. 20, no. 18, p. 5187, Sep 2020.

[54] G. Galati, G. Pavan, K. Savci, and C. Wasserzier, "Noise radar technology: Waveforms design and field trials," *Sensors*, vol. 21, no. 9, p. 3216, May 2021.

[55] K. Savci, G. Galati, and G. Pavan, "Low-papr waveforms with shaped spectrum for enhanced low probability of intercept noise radars," *Remote Sensing*, vol. 13, no. 12, p. 2372, Jun 2021.

[56] G. Galati, G. Pavan, K. Savci, and C. Wasserzier, "Counter-interception and counter-exploitation features of noise radar technology," *Remote Sensing*, vol. 13, no. 22, p. 4509, Nov 2021.

[57] K. Savci, "A limited memory bfgs based unimodular sequence design algorithm for spectrum-aware sensing systems," *IEEE Access*, 2022.

[58] C. Hulsmeyer, "The telemobiloscope," *Electrical Magazine*, vol. 2, 1904.

[59] C. Hülsmeyer, "Verfahren, um entfernte metallische gegenstände mittels elektrischer wellen einem beobachter zu melden," Patent, German Patent 165,546, 30 April 1904.

[60] P. E. Pace, *Detecting and Classifying Low Probability of Intercept Radar, 2nd Ed.* Artech House: Norwood, MA, USA, 2009.

[61] G. Galati, G. Pavan, and F. De Palo, "Generation of pseudo-random sequences for noise radar applications," in *2014 15th International Radar Symposium (IRS)*, June 2014, pp. 1–4.

[62] G. Galati, G. Pavan, F. De Palo, and A. Stove, "Potential applications of noise radar technology and related waveform diversity," in *2016 17th International Radar Symposium (IRS)*, 2016, pp. 1–5.

[63] R. Bourret, "A proposed technique for the improvement of range determination with noise radar," *IRE Proceedings*, vol. 45, 1957.

[64] B. Hourton, "Noise-modulated distance measuring system," *IRE Proceedings*, vol. 49, 1959.

[65] M. Wicks, "Spectrum crowding and cognitive radar," in *2010 2nd International Workshop on Cognitive Information Processing*, 2010, pp. 452–457.

[66] J. R. Guerci, "Cognitive radar: A knowledge-aided fully adaptive approach," in *2010 IEEE Radar Conference*, 2010, pp. 1365–1370.

[67] S. Haykin, "Cognitive dynamic systems: Radar, control, and radio [point of view]," *Proceedings of the IEEE*, vol. 100, no. 7, pp. 2095–2103, 2012.

[68] C. E. Cook and M. Bernfeld, *Radar Signals: An Introduction to Theory and Application.* Academic Press, USA, 1967.

[69] A. De Martino, *Introduction to Modern EW Systems, 2nd Ed.* Artech House, 2018.

[70] G. Galati and G. Pavan, "Compatibility problems related with pulse-compression, solid-state marine radars," *IET Radar, Sonar & Navigation*, vol. 10, pp. 791–797(6), April 2016.

[71] V. S. Chernyak, "On the concept of mimo radar," in *2010 IEEE Radar Conference*, 2010, pp. 327–332.

[72] P. Woodward, *Probability and Information Theory with Applications to Radar.* McGraw-Hill: New York, NY, USA, 1953.

[73] M. Skolnik, *Radar Handbook, Third Edition*, ser. Electronics electrical engineering. McGraw-Hill Education, 2008.

[74] Z. Shi, S. Qiao, S. Chen, T. Jiang, and X. Ran, "Ambiguity function of direct chaotic radar employing microwave chaotic colpitts oscillator," vol. 77, pp. 1–14, 2007.

[75] J. E. Gentle, *Random Number Generators and Monte Carlo Methods, 2nd Ed.* Springer, NY, USA, 2003.

[76] "Mersenne twister, a very fast random number generator of period $2^{19937} - 1$." [Online]. Available: http://www.math.sci.hiroshima-u.ac.jp/m-mat/MT/emt.html

[77] F. De Palo and G. Galati, "Range sidelobes attenuation of pseudorandom waveforms for civil radars," in *2017 European Radar Conference (EURAD)*, Oct 2017, pp. 114–117.

[78] S. Haykin, Y. Xue, and P. Setoodeh, "Cognitive radar: Step toward bridging the gap between neuroscience and engineering," *Proceedings of the IEEE*, vol. 100, no. 11, pp. 3102–3130, 2012.

[79] M. S. Greco, F. Gini, P. Stinco, and K. Bell, "Cognitive radars: On the road to reality: Progress thus far and possibilities for the future," *IEEE Signal Processing Magazine*, vol. 35, no. 4, pp. 112–125, 2018.

[80] J. M. Blackledge, *Digital Signal Processing : Mathematical and Computational Methods, Software Development and Applications, 2nd Ed.* Horwood Publishing, UK, 2006.

[81] N. Wiener, *Extrapolation, Interpolation, and Smoothing of Stationary Time Series.* Wiley, NY, USA, 1949.

[82] G. Turin, "An introduction to matched filters," *IRE Transactions on Information Theory*, vol. 6, no. 3, pp. 311–329, 1960.

[83] A. Rihaczek, "Doppler-tolerant signal waveforms," *Proceedings of the IEEE*, vol. 54, no. 6, pp. 849–857, 1966.

[84] M. Friese, "Polyphase barker sequences up to length 36," *IEEE Transactions on Information Theory*, vol. 42, no. 4, pp. 1248–1250, July 1996.

[85] A. R. Brenner, "Polyphase barker sequences up to length 45 with small alphabets," *Electronics Letters*, vol. 34, no. 16, pp. 1576–1577, Aug 1998.

[86] P. Borwein and R. Ferguson, "Polyphase sequences with low autocorrelation," *IEEE Transactions on Information Theory*, vol. 51, no. 4, pp. 1564–1567, 2005.

[87] R. Gold, "Optimal binary sequences for spread spectrum multiplexing (corresp.)," *IEEE Transactions on Information Theory*, vol. 13, no. 4, pp. 619–621, October 1967.

[88] Y. Sun, P. Babu, and D. P. Palomar, "Majorization-minimization algorithms in signal processing, communications, and machine learning," *IEEE Transactions on Signal Processing*, vol. 65, no. 3, pp. 794–816, 2017.

[89] L. Zhao, J. Song, P. Babu, and D. P. Palomar, "A unified framework for low autocorrelation sequence design via majorization–minimization," *IEEE Transactions on Signal Processing*, vol. 65, no. 2, pp. 438–453, 2017.

[90] K. Krzysztof, *Signal Processing in Noise Waveform Radar*, ser. Radar Library. Artech House, Boston, Massachusetts, 2020.

[91] A. Popov, P. Rybkin, and V. Vasil'ev, "The report of experiments on electrical wireless signalization performed by a mine detachment during the campaign of 1897 *inrussian*," *In Collection of Documents and Materials 50 Years of*

Radio; Invention of Radio by A.S. Popov; Berg, A.I., Ed.; The Academy of Sciences of the U.S.S.R.: Moscow, 1945.

[92] L. Pralon, G. Beltrao, A. Barreto, and B. Cosenza, "On the analysis of pm/fm noise radar waveforms considering modulating signals with varied stochastic properties," *Sensors*, vol. 21, no. 5, p. 1727, Mar 2021.

[93] K. M. M. Prabhu, *Window Functions and Their Applications in Signal Processing.* CRC Press, 2014.

[94] A. W. Doerry, "Catalog of window taper functions for sidelobe control," Albuquerque, MN, USA, Tech. Rep., 2017.

[95] T. Taylor, "Design of line-source antennas for narrow beamwidth and low side lobes," *Transactions of the IRE Professional Group on Antennas and Propagation*, vol. 3, no. 1, pp. 16–28, 1955.

[96] W. Carrara, R. Goodman, and R. Majewsli, *Spotlight Synthetic Aperture Radar Signal Processing Algorithms*, ser. Springer Series in Operations Research and Financial Engineering. Artech House: Norwood, MA, USA, 1995.

[97] P. P. Ann and R. Jose, "Comparison of papr reduction techniques in ofdm systems," in *2016 International Conference on Communication and Electronics Systems (ICCES)*, 2016, pp. 1–5.

[98] S. H. Han and J. H. Lee, "An overview of peak-to-average power ratio reduction techniques for multicarrier transmission," *IEEE Wireless Communications*, vol. 12, no. 2, pp. 56–65, 2005.

[99] J. Tropp, I. Dhillon, R. Heath, and T. Strohmer, "Designing structured tight frames via an alternating projection method," *IEEE Transactions on Information Theory*, vol. 51, no. 1, pp. 188–209, 2005.

[100] L. Taylor, "The phase retrieval problem," *IEEE Transactions on Antennas and Propagation*, vol. 29, no. 2, pp. 386–391, 1981.

[101] R. W. Gerchberg, "A practical algorithm for the determination of phase from image and diffraction plane pictures," vol. 35, 1972, p. 237.

[102] S. H. Han and J. H. Lee, "Papr reduction of ofdm signals using a reduced complexity pts technique," *IEEE Signal Processing Letters*, vol. 11, no. 11, pp. 887–890, 2004.

[103] A. Rihaczek, *Principles of High Resolution Radar*. Artech House: Norwood, MA, USA, 1996.

[104] C. Wasserzier and G. Galati, "On the efficient computation of range and doppler data in noise radar," *International Journal of Microwave and Wireless Technologies*, vol. 11, pp. 584 – 592, 2019.

[105] L. Cohen, *Time-Frequency Analysis*. Prentice Hall: Hoboken, NJ, USA, 1995.

[106] J. Ville, "Theorie et applications de la notion de signal analytique," *Cables Transm.*, vol. 2, pp. 61–74.

[107] H. I. Choi and W. Williams, "Improved time-frequency representation of multicomponent signals using exponential kernels," *IEEE Transactions on Acoustics, Speech, and Signal Processing*, vol. 37, no. 6, pp. 862–871, 1989.

[108] J. Antoni, "The spectral kurtosis: a useful tool for characterising non-stationary signals," *Mechanical Systems and Signal Processing*, vol. 20, no. 2, pp. 282–307, 2006.

[109] J. Antoni and R. Randall, "The spectral kurtosis: application to the vibratory surveillance and diagnostics of rotating machines," *Mechanical Systems and Signal Processing*, vol. 20, no. 2, pp. 308–331, 2006.

[110] J. Nocedal and S. J. Wright, *Numerical Optimization*, ser. Springer Series in Operations Research and Financial Engineering. Springer, New York, NY, 2006.

[111] Y.-C. Wang, L. Dong, X. Xue, and K.-C. Yi, "On the design of constant modulus sequences with low correlation sidelobes levels," *IEEE Communications Letters*, vol. 16, no. 4, pp. 462–465, 2012.

[112] E. Polak and G. Ribiere, "Note sur la convergence de méthodes de directions conjuguées," *ESAIM: Mathematical Modelling and Numerical Analysis - Modélisation Mathématique et Analyse Numérique*, vol. 3, no. R1, pp. 35–43, 1969.

[113] B. R. Mahafza, *Radar system analysis and design using Matlab.* Boca Raton, USA, Chapman & Hall/CRC, 2000.